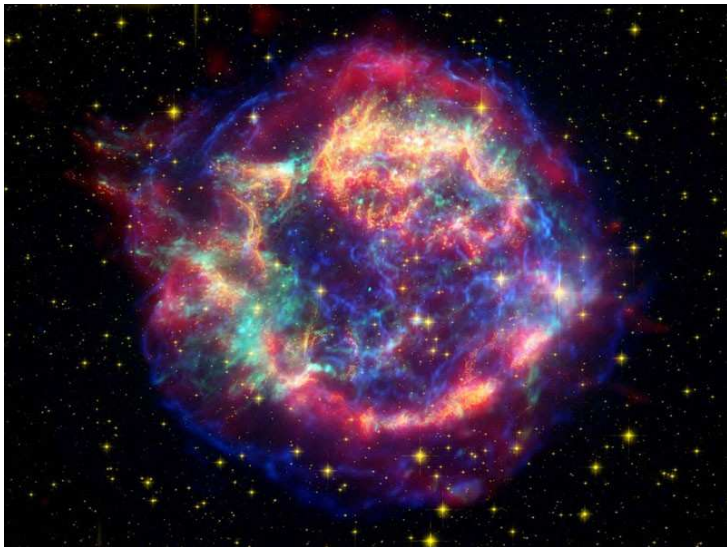


PAMELA measurements of high energy cosmic ray positrons

LAURA ROSSETTO



KTH Engineering Sciences

Doctoral Thesis
Stockholm, Sweden 2012



KTH Engineering Sciences

Doctoral Thesis
PAMELA measurements of high energy
cosmic ray positrons

Laura Rossetto

Particle and Astroparticle Physics, Department of Physics,
Royal Institute of Technology, SE-106 91 Stockholm, Sweden

Stockholm, Sweden 2012

Cover illustration: Cassiopeia A supernova remnant located approximately 3.4 kpc away in the Milky Way, in the constellation Cassiopeia. It is a false colour composite image synthesized from observations gathered in different spectral regions by three space-based observatories. Red areas represent infrared data from the Spitzer Space Telescope. Yellow areas represent visible light data collected by the Hubble Space Telescope. Green and blue areas are X-ray data from the Chandra X-ray Observatory.

Akademisk avhandling som med tillstånd av Kungliga Tekniska Högskolan i Stockholm framlägges till offentlig granskning för avläggande av teknologie doktorsexamen måndagen den 11 juni 2012 kl 13:15 i sal FB42, AlbaNova Universitetscentrum, Roslagstullsbacken 21, Stockholm.

Avhandlingen försvaras på engelska.

ISBN 978-91-7501-362-6

TRITA-FYS 2012:27

ISSN 0280-316X

ISRN KTH/FYS/--12:27--SE

© Laura Rossetto, May 2012

Printed by Universitetsservice US AB 2012

Abstract

PAMELA is a satellite-borne experiment mounted on board of the Russian Resurs DK1 satellite which was launched from the Baikonur cosmodrome in Kazakhstan on June 15th 2006. The satellite orbits around the Earth on a semi-polar and elliptical trajectory and PAMELA has been acquiring data for almost six years. The detector was designed and optimised for the study of the antimatter component in the cosmic radiation. The PAMELA apparatus consists of a time-of-flight system, a permanent magnetic spectrometer, an electromagnetic calorimeter, a neutron detector and an anticoincidence system. Combining information from different detectors and in particular from the calorimeter, positrons can be identified from the significant background due to cosmic ray protons.

The interest in cosmic ray positron measurements considerably increased in the last years because of new experimental results. The positron fraction measured by the PAMELA detector clearly increases with energy above 10 GeV. This is not in agreement with a pure secondary positron production, thus indicating a probable primary origin of positrons. In this context, a measurement of the positron fraction and of the positron flux up to the maximum energy permitted by the PAMELA design becomes extremely important.

In view of extending positron measurements, a method for positron identification has been studied. The method uses longitudinal and transverse shower profile variables in the calorimeter for separating electromagnetic and hadronic showers. This method has been first tested on simulated positron and background proton events produced in two different energy ranges (20 – 100 GeV and 100 – 300 GeV). Proton contamination can arise in identified positron events due to the production of neutral pions which decay electromagnetically. Positron and electron events have been identified from positively and negatively charged particles in flight data, allowing the positron fraction and the positron flux to be reconstructed up to an energy of ~ 300 GeV. As a cross-check, a multivariate approach has also been applied to flight data in order to estimate the number of positron and electron events at energies greater than 100 GeV. The positron fraction obtained with these two different methods are in good agreement within statistical uncertainties. The resulting positron flux measurement shows a rise at energies greater than 100 GeV.

Contents

Abstract	iii
Contents	v
Introduction	1
1 Cosmic rays	5
1.1 The energy spectrum	5
1.2 Acceleration mechanisms	8
1.3 Propagation mechanisms	12
1.3.1 Diffusion processes	12
1.3.2 Convection processes	12
1.3.3 Reacceleration processes	13
1.4 Solar modulation	13
1.5 Cosmic ray positrons and electrons	17
1.5.1 PAMELA positron fraction	19
1.5.2 PAMELA electron flux	20
1.5.3 Theoretical interpretations	23
2 The PAMELA experiment	27
2.1 The PAMELA apparatus	27
2.1.1 The time-of-flight system	30
2.1.2 The magnetic spectrometer	31
2.1.3 The electromagnetic calorimeter	32
2.1.4 The neutron detector	34
2.1.5 The anticoincidence system	34
2.2 The PAMELA data acquisition system	37
2.2.1 The trigger configuration	38
2.3 PAMELA scientific goals	38

3 Shower development in the PAMELA calorimeter	41
3.1 Electromagnetic showers	41
3.1.1 The shower profiles	44
3.2 Hadronic showers	46
3.2.1 The shower profiles	48
3.3 The π^0 contamination of hadronic showers	50
3.4 The PAMELA electromagnetic calorimeter	51
3.4.1 Shower profile variables	51
4 Simulation studies of π^0 contamination	63
4.1 GEANT3 simulations	63
4.2 “Only- π^0 case” simulations	67
4.3 Simulation analysis	67
4.4 Positron selection criteria	70
4.4.1 Tracker selections	70
4.4.2 Time-of-flight selections	71
4.4.3 Anticoincidence selections	71
4.4.4 Calorimeter selections	72
4.5 The “Nature analysis” approach	73
4.6 A new approach for positron identification	81
4.7 Analysis in the energy range 20 – 100 GeV	85
4.7.1 Positron selection efficiencies	85
4.7.2 Proton contamination	88
4.8 Analysis in the energy range 100 – 300 GeV	90
4.9 Positron fraction	99
4.10 Conclusions	106
5 Multivariate analysis approach	109
5.1 The Toolkit for Multivariate Analysis	109
5.2 The MultiLayers Perceptron neural network	110
5.3 Analysis in the energy range 100 – 300 GeV	111
5.4 Positron fraction	118
5.5 Conclusions	121
6 Positron flux	123
6.1 Flux evaluation	123
6.2 The live time	124
6.3 The geometrical factor	125
6.4 Selection efficiencies	128
6.4.1 Trigger efficiency	128
6.4.2 Efficiency of selections above the calorimeter	128
6.4.3 Calorimeter efficiency	129
6.5 Positron flux	131
7 Conclusions	135

<i>Contents</i>	vii
Acknowledgments	137
List of figures	139
List of tables	143
Bibliography	145

Introduction

Outline of the thesis

The work presented in this thesis concerns positron selection studies which have been tested on simulations and then applied to flight data collected by the PAMELA satellite experiment between July 2006 and January 2010. The positron fraction and the positron flux have been evaluated up to ~ 300 GeV. A potential proton contamination in positron identification due to neutral pion production was also studied in a detailed way and is also presented in this thesis.

In chapter 1 basic concepts and features of cosmic rays are presented together with a description of acceleration and propagation mechanisms throughout the galaxy. Particular attention is focused on cosmic ray positrons and on the positron fraction first published by the PAMELA Collaboration in 2009. Chapter 2 is dedicated to a detailed description of the components which constitute the PAMELA experiment. The main scientific goals are briefly summarized together with performance for the detection of cosmic ray particles and antiparticles. In chapter 3 electromagnetic and hadronic shower development inside the calorimeter are described; neutral pion contamination in hadronic showers is also presented. Furthermore, a detailed description of the transverse shower profile variables used in the analysis work is presented. Chapter 4 is dedicated to GEANT3 simulation studies of hadronic and electromagnetic showers induced by protons and positrons inside the calorimeter. A new approach for positron identification using shower profile variables in the calorimeter is also described: this method has been tested on simulations in two different energy ranges and up to a maximum energy of 300 GeV. This method was then applied to flight data in order to select positron and electron events. The resulting positron fraction is shown at the end of this chapter. As a cross-check to the results presented in chapter 4, a multivariate approach has also been applied to flight data in order to estimate the number of electron and positron events. This method and the resulting positron fraction are presented in chapter 5. In chapter 6 the procedure followed to evaluate the positron flux up to ~ 300 GeV is described. The obtained result is shown and compared to the positron flux evaluated by other experiments.

The author's contribution

I joined the PAMELA Collaboration in October 2007 when I started working as a PhD student in the Particle and Astroparticle Physics group at KTH. The first year was mainly focused on learning about the PAMELA experiment. Some months were spent studying the momentum-velocity ($p\beta$) method applied to the PAMELA calorimeter in order to separate antiprotons from negatively charged pions. I produced simulated data sets for this work. This analysis was documented as a PAMELA Collaboration note but is not described further in this thesis. In the second year of my PhD I started working on simulations which focused on the study of neutral pion production in hadronic showers inside the calorimeter. I used the PAMELA Collaboration's official simulation code and I modified it in order to artificially increase the number of neutral pions produced in hadronic showers and study the consequences for positron identification. I studied and applied to my simulations standard positron selection criteria used by the Collaboration in the positron analysis. I also developed new selection criteria in the calorimeter with the goal of obtaining a new measurement of the positron fraction and of the positron flux up to a maximum energy of 300 GeV.

The work presented in this thesis was presented at several PAMELA Collaboration meetings. Part of the simulation analysis has been previously reported in a Licentiate thesis. Furthermore, this work has been presented in a poster at the 32nd International Cosmic Ray Conference in 2011:

- Laura Rossetto, *Studies of positron identification with the PAMELA calorimeter*. Licentiate Thesis, Physics Department, Royal Institute of Technology, Stockholm, Sweden, 2010. TRITA-FYS 2010:61.
- Laura Rossetto, on behalf of the PAMELA Collaboration, *Positron identification study with the PAMELA calorimeter*. Proceedings of the 32nd International Cosmic Ray Conference, Beijing 2011.

This work will also be part of a future publication concerning the high energy behaviour of the positron fraction and the absolute positron flux.

I am also co-author of the following articles published by the PAMELA Collaboration:

- O. Adriani et al. *Measurements of quasi-trapped electron and positron fluxes with PAMELA*. Journal of Geophysical Research, **114**: A12218, 2009.
- O. Adriani et al. *A statistical procedure for the identification of positrons in the PAMELA experiment*. Astroparticle Physics, **34**: 1 – 11, 2010.
- O. Adriani et al. *PAMELA Results on the Cosmic-Ray Antiproton Flux from 60 MeV to 180 GeV in Kinetic Energy*. Physical Review Letters, **105**: 121101–1 – 5, 2010.

- O. Adriani et al. *PAMELA Measurements of Cosmic-Ray Proton and Helium Spectra*. *Science*, **332** (6025): 69 – 72, 2011.
- O. Adriani et al. *Observations of the 2006 December 13 and 14 Solar Particle Events in the 80 MeV/n - 3 GeV/n range from space with PAMELA detector*. *The Astrophysical Journal*, **742**: 102, 2011.
- O. Adriani et al. *Cosmic-Ray Electron Flux Measured by the PAMELA Experiment between 1 and 625 GeV*. *Physical Review Letters*, **106**: 201101–1 – 5, 2011.
- O. Adriani et al. *The discovery of geomagnetically trapped cosmic-ray antiprotons*. *The Astrophysical Journal Letters*, **737**: L29, 2011.

Chapter 1

Cosmic rays

Cosmic rays are high energy particles travelling through outer space and arriving at the Earth. About 98 % of these particles are *protons* and *nuclei* while about 2 % are *electrons*. The hadronic component comprises protons (~ 87 %), helium nuclei (~ 12 %) and heavier nuclei (~ 1 %) [1]. These particles come from galactic or extragalactic astrophysical sources and are so called *primary* cosmic rays. They are deflected by the galactic magnetic field and thus travel a random path before arriving to the Earth. Along this path they can interact with the interstellar medium and create *secondary* particles. Also, when these high energy particles enter the Earth's atmosphere, they collide with the molecules of atmospheric gases and produce a large number of lower energy particles called *Extensive Air Showers*. Only particles with energy greater than 10^{14} eV generate particle showers which can pass through all the atmosphere and can be detected by surface array detectors. Particles with energy below 10^{14} eV can only be detected outside the atmosphere using balloon-borne or satellite experiments.

In this first chapter basic concepts and features of cosmic rays are presented together with some recent experimental results. Particular attention is focused on the results published by the PAMELA Collaboration.

1.1 The energy spectrum

The cosmic ray energy spectrum extends from $E \sim 10^8$ eV up to $E \sim 10^{20}$ eV. Figure 1.1 shows the all particle energy spectrum of cosmic rays [2]. The energy spectrum is well represented by a power-law distribution $I(E) \propto E^{-\alpha}$ but two changes in the spectral index are visible. For $E > 10^9$ eV the spectrum has a spectral index $\alpha = 2.7$; the spectrum becomes then steeper at $E \sim 3 \cdot 10^{15}$ eV with a spectral index $\alpha = 3.1$: this is the so called *knee* of the spectrum. The spectral index changes again around 10^{18} eV, the so called *ankle* of the spectrum [3]. Recent measurements obtained from the Pierre Auger Observatory show that the

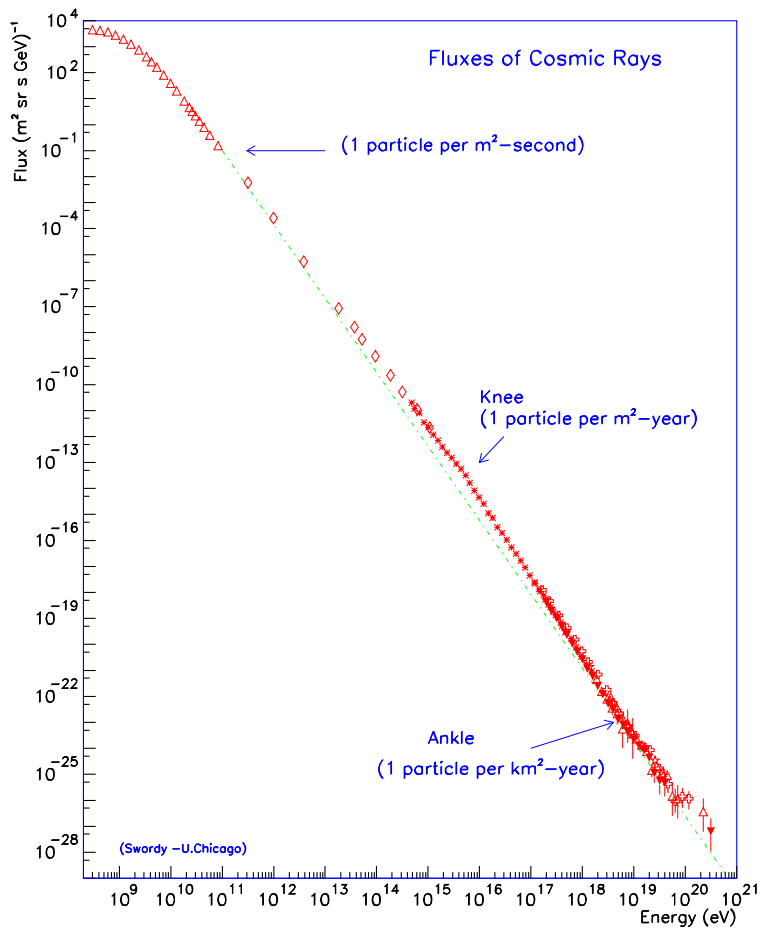


Figure 1.1. The all particle energy spectrum of cosmic rays at the top of the atmosphere [2].

ankle is located at $E = 10^{18.6}$ eV and that the spectral index is $\alpha \sim 3.3$ below the ankle and $\alpha \sim 2.6$ above the ankle [4].

The origin of the knee and the ankle in the cosmic ray energy spectrum is still unknown but there are theories which provide several explanations. For instance, the knee energy could represent the boundary between particles accelerated inside our galaxy and those of extragalactic origin. In our galaxy cosmic rays can be accelerated up to a maximum energy $E_{max} \propto Z \cdot (L \cdot B)$ which depends on the size L and the magnetic field strength B of the acceleration region and on the charge Z of the primary particle. Another theory is that particles are constrained within the galaxy by the galactic magnetic field up to the knee energy, i.e. $E_{max} \approx Z \cdot 3 \cdot 10^{15}$ eV. The knee energy depends on the charge Z of the primary particle and thus the knee is expected at higher energies for particles with higher Z values. Data from Extensive Air Showers detected by the EAS-TOP array show a dominance of helium primaries around the knee at $3.5 \cdot 10^{15}$ eV; they indicate also the knee energy for elements like carbon, nitrogen and oxygen to be around $(6 - 7) \cdot 10^{15}$ eV [5]. Furthermore, measurements from the KASCADE array show the knee at $(3 - 5) \cdot 10^{15}$ eV to be caused by a steepening in the light-element spectra (mostly hydrogen and helium) [6], [7]. A knee-like structure in the spectrum of the heavy component ($Z > 13$ up to iron nuclei) is instead expected in the energy range from $\sim 4 \cdot 10^{16}$ eV to $\sim 1.2 \cdot 10^{17}$ eV [8]. Recent measurements performed by the KASCADE-Grande array show the first evidence of a knee-like feature in the heavy component spectrum at about $8 \cdot 10^{16}$ eV, with the spectral slope changing from $\alpha = 2.76$ before the knee to $\alpha = 3.24$ after the knee [8].

Particles beyond the ankle are thought to be of extragalactic origin because their gyroradius is larger than the size of the galaxy. Furthermore, a sharp cut-off is expected around $\sim 5 \cdot 10^{19}$ eV (the so called GZK cut-off) due to interactions of particles with the cosmic microwave background photons [3]. This effect was predicted by Greisen [9], Zatsepin and Kuz'min [10] in 1966. Measurements performed by the Pierre Auger Observatory indicate a strong flux suppression above $4 \cdot 10^{19}$ eV [11].

For energies less than $\sim 10^9$ eV the cosmic ray flux undergoes the effect of *solar modulation*. Thus, the attenuation of the power-law spectrum observed at low energies varies with the phase of the solar cycle (see section 1.4).

Another important feature is that the slopes of energy spectra are different for different elements. This is due to the fact that there are *primary* and *secondary* cosmic rays elements. The primary elements, such as carbon and oxygen, are accelerated in large abundances in sources of high energy particles while secondary particles, like lithium, beryllium and boron, are created by nuclear interactions of primary cosmic rays with the nuclei of the interstellar gas. This last process is known as *spallation*. Secondary particles show significantly steeper spectra than those of primary ones [1]. Figure 1.2 shows relative abundances of galactic cosmic rays at the top of the Earth's atmosphere compared with the relative abundances of these elements in the solar system. The relative abundances of elements like carbon and oxygen are similar in both cases, thus demonstrating that these are primary

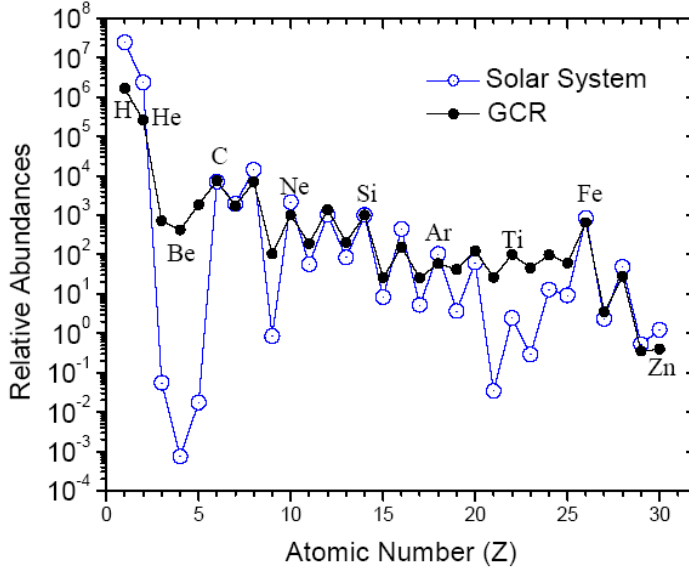


Figure 1.2. Relative abundances of galactic cosmic rays (GCR) at the top of the Earth's atmosphere (black full circles) compared with the relative abundances of these elements in the solar system (blue open circles). Abundances of both GCR and solar system elements are normalized to Si = 10^3 . Data of cosmic-ray abundances for elements heavier than helium are taken from the ACE/CRIS experiment [12], [13].

elements. On the other hand, some elements that are rare in the solar system such as lithium, beryllium and boron are more abundant in galactic cosmic rays. This indicates that these elements are secondary ones produced by spallation process.

1.2 Acceleration mechanisms

The mechanism by which charged particles are accelerated to high energies was first introduced by Fermi in 1949 and is based on the acceleration in strong shock waves, such as those produced in *supernovae explosions*. This mechanism is based on the assumption that particles have an isotropic velocity distribution behind the shock and that they diffuse from behind the shock to the upstream region in front of the shock itself. The important thing is that particles receive an increase of energy every time they cross the shock front and this increment in energy is the same going in both directions (head-on collisions). The average energy gained on crossing the shock is:

$$\left\langle \frac{\Delta E}{E} \right\rangle = \frac{2}{3} \cdot \frac{V}{c} \quad (1.1)$$

where V is the velocity of the gas behind the shock and c is the velocity of light [14]. This mechanism is also called *first order Fermi acceleration* due to the fact that it is first order in V/c . In the *second order acceleration* mechanism the average energy gained is:

$$\left\langle \frac{\Delta E}{E} \right\rangle = \frac{2}{3} \cdot \left(\frac{V}{c} \right)^2 \quad (1.2)$$

In this case charged particles are reflected by irregularities in the galactic magnetic field assumed to move randomly with velocity V : since V is very small compared to the velocity of light ($V/c \leq 10^{-4}$) the rate of energy gain by particles is very slow and the *second order acceleration* is not so efficient. Equation 1.1 is a very important result because using this acceleration mechanism a power-law differential energy spectrum of the high energy particles can be obtained [14]:

$$N(E)dE \propto E^{-2}dE. \quad (1.3)$$

There is an upper limit to the energy to which particles can be accelerated by this mechanism. The first order Fermi acceleration is in fact a slow process and particles have to diffuse back and forth across the shock wave in order to gain a lot of energy. Considering for instance the shock wave of a *supernova remnant*, its acceleration phase lasts typically about 10^5 years and the upper limit to the energy of particles which can be accelerated in typical supernova explosions is about 10^{14} eV/nucleon. As already mentioned, the cosmic ray spectrum extends well beyond this upper limit and so shock acceleration in supernovae cannot account for the complete range of energies observed [14].

One of the possible candidates for a source of the highest energy cosmic rays is the *pulsar magnetosphere* (figure 1.3). Pulsars with strong magnetic fields and short periods, such as the Crab pulsar, have such strong electric potentials within the magnetospheres that particles can be accelerated to high energies. Using Maxwell's first equation one can evaluate the maximum amount of energy which a particle can attain in a magnetic field of strength B and dimension L :

$$E_{max} = \gamma mc^2 \sim zeBcL \quad (1.4)$$

and considering for instance the magnetic field of a young pulsar, $B = 10^6$ T and a region of dimension $L \sim 100$ km, the total energy given to the particle is:

$$E_{max} = 5 \text{ J} = 3 \cdot 10^{19} \text{ eV} \quad (1.5)$$

Thus, this result shows that particles could be accelerated to the highest energies in the vicinity of pulsars [14]. In the same way charged particles can be confined in other large astrophysical objects, like active galactic nuclei (AGN) or gamma ray bursts (GRB), and can be accelerated through repeated crossing of the plasma shock fronts. The so called Hillas plot is displayed in figure 1.4. The diagram shows the maximum kinetic energy to which particles can be accelerated (black lines) in relation to the size and the magnetic field strength of some celestial objects [15].

In GRBs for instance, neutrinos are expected to be produced in the decay of charged pions produced in interactions between high energy protons and the intense γ ray background. Very recent measurements of the IceCube neutrino observatory [16] seem disfavour GRBs as cosmic ray accelerator at energies above 10^{18} eV. This result shows an upper limit on the flux of energetic neutrinos associated with GRBs that is at least a factor of 3.7 below the theoretical predictions.

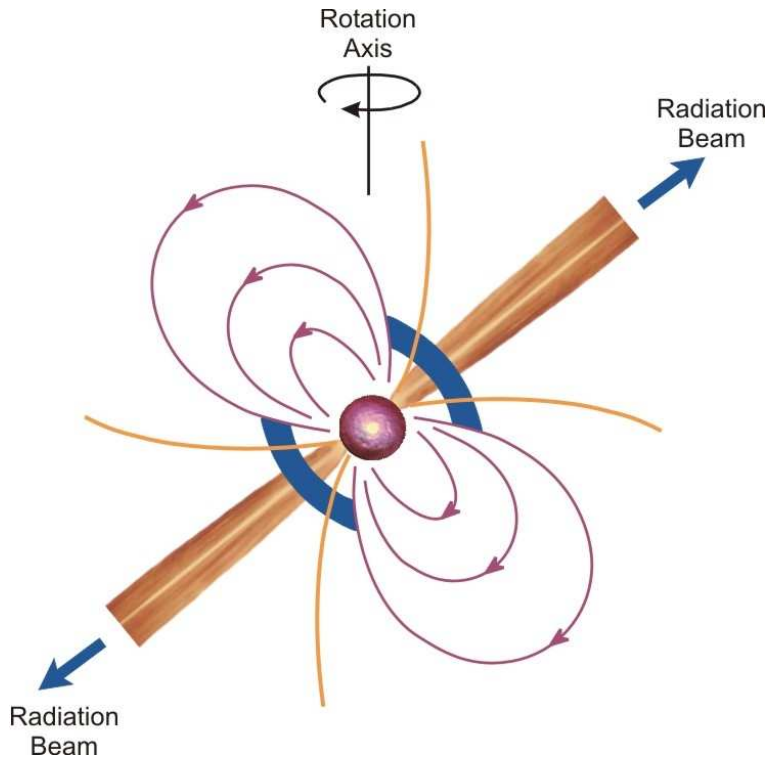


Figure 1.3. A schematic model of a pulsar: the sphere in the middle represents the rotating neutron star in which the magnetic and rotation axes are misaligned, the curves indicate the magnetic field lines and the two cones represent the emission beams. The radio pulses are caused by radio emission from the poles of the magnetic field distribution. Typical parameters for a neutron star are: $M = 1.4 M_{\odot}$, $R = 10$ km, $\vec{B} = 10^4 - 10^9$ T.

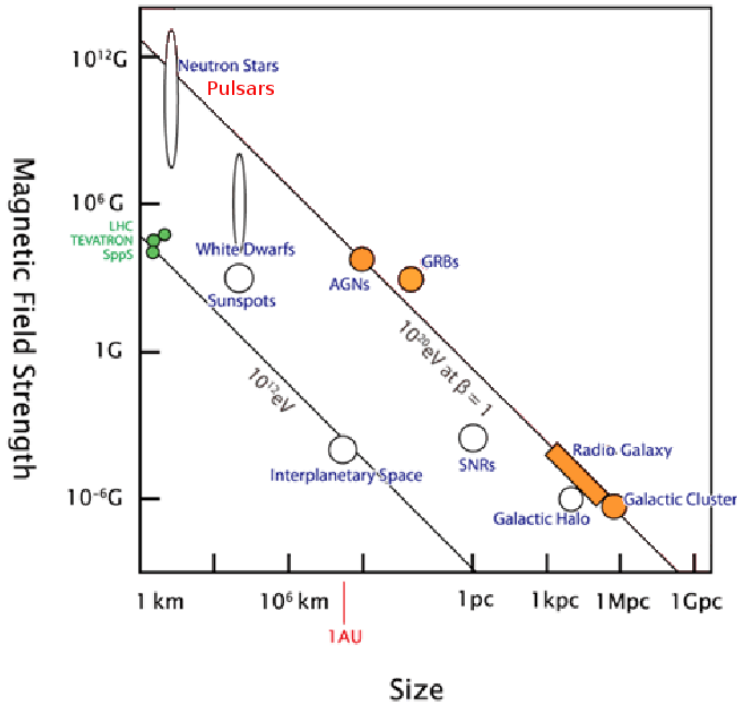


Figure 1.4. Hillas plot: size L and magnetic field strength B diagram for some celestial objects. The minimum product $B \cdot L$ for containing particles with energy 10^{12} eV and 10^{20} eV is also shown (black lines) [15].

1.3 Propagation mechanisms

Once particles are accelerated to very high energies, as described in the section 1.2, they propagate through the interstellar medium before reaching the Earth. During the propagation phase the particles lose energy by interacting with matter, magnetic fields and radiation. The processes which participate in the particle transportation are diffusion, convection and re-acceleration.

1.3.1 Diffusion processes

A way to describe cosmic ray propagation is the *diffusion-loss equation*:

$$\frac{dN(E)}{dt} = \frac{d}{dE} [b(E)N(E)] + Q(E, t) + D \nabla^2 N(E) \quad (1.6)$$

for high energy electrons and

$$\frac{dN_i(E)}{dt} = \frac{d}{dE} [b(E)N_i(E)] + Q_i(E, t) + D \nabla^2 N_i(E) - \frac{N_i(E)}{\tau_i} + \sum_{j>i} \frac{P_{ij}}{\tau_j} N_j \quad (1.7)$$

for light nuclei [14].

In both cases, the term $d[b(E)N(E)]/dE$ describes the temporal evolution of the particle energy spectrum in an elementary volume dV subject only to energy gains and losses while the term $Q(E, t)$ is the rate of injection of particles per unit volume. The *diffusion process* which permits particles to enter and leave the volume dV is described by the term $D \nabla^2 N(E)$: this process depends upon the gradient of particle density $N(E)$ and the scalar diffusion coefficient D . Typical values of the diffusion coefficient are $D \sim (3 - 5) \cdot 10^{28} \text{ cm}^2 \text{ s}^{-1}$ at energy $\sim 1 \text{ GeV/n}$. This value increases with magnetic rigidity as $R^{0.3} - R^{0.6}$ in different diffusion models of cosmic ray propagation [17]. In the light nuclei case all these quantities refer to a particular species i . Furthermore, the last two terms describe the effects of spallation gains and losses: τ_i and τ_j are the spallation lifetimes of particles of species i and j and P_{ij} is the probability that the species i is created during an inelastic collision involving the destruction of the nucleus j . As indicated by the sum in the last term, it is the spallation of all species with $j > i$ which gives contributions to the number density of nuclei of species i , N_i [14].

1.3.2 Convection processes

Although the most important propagation process is diffusion, experimental data show that diffusion alone cannot account for the entire propagation process. Cosmic rays can be transported also through the galactic winds existing in many galaxies. Galactic winds are streams of charged particles, equivalent to the solar wind but on

galactic scale. They result from different contributions: solar winds of very massive and bright stars, accretion processes of massive stars, supernovae explosions and accretion processes of supermassive black holes at the centre of galaxies.

Nowadays, two models describing this process have been studied: the one-zone and the two-zone model. In the so called one-zone model convection and diffusion processes are both present through-out the galaxy. In the two-zone model diffusion plays a role alone up to 1 kpc distance from the plane of the galaxy and both diffusion and convection are present beyond [17].

1.3.3 Reacceleration processes

Cosmic ray particles can be accelerated also by magnetohydrodynamic (MHD) waves due to inhomogeneities in the galactic magnetic field. This process is called *reacceleration* to distinguish it from the primary acceleration process. Reacceleration depends on the velocity of disturbances propagating in a magnetic field (Alfvén velocity). Data on secondary nuclei abundances can be well explained considering reacceleration processes in the energy range 1-100 GeV/nucleon: the increase of the relative abundance of secondary nuclei, in this part of the spectrum, as the energy increases could be explained by the fact that particles spend longer time in the region due to reacceleration [17]. Furthermore, for energies greater than ~ 100 GeV/nucleon diffusion and/or convection processes starts being predominant thus explaining the decreasing of secondary nuclei abundances as function of energy. For instance, diffusive-reacceleration models described in [18] adapt well to the measured boron-to-carbon ratio (B/C), showing also that models predicting reacceleration of cosmic rays produce the characteristic peak observed in the B/C ratio spectra at approximately 1 GeV/nucleon. Theoretical B/C ratio energy spectra are shown in figure 1.5 together with experimental data.

Simulation studies of different propagation models of cosmic rays in the galaxy have been performed by Wu [20] considering experimental data of the B/C ratio and the antiproton-to-proton flux ratio as measured by PAMELA [21].

1.4 Solar modulation

When cosmic ray particles enter the solar system they travel across the heliosphere before reaching the Earth. The heliosphere extends ~ 120 AU from the Sun [22] and it is that part of space dominated by the solar wind and the heliospheric magnetic field. The solar wind is a plasma consisting mainly of hydrogen, helium and some heavier nuclei, all highly ionized, and electrons. It flows away from the Sun with a velocity of about 300 km/s to 800 km/s [22]. The solar wind is modulated by the solar activity which is periodic with a 11 year cycle and, as a consequence, also the cosmic ray flux undergoes a modulation. The 11 year cycle includes variations due to changing magnetic conditions in the heliosphere. Stronger magnetic fields and turbulences reduce the intensity of low energy galactic cosmic rays in the heliosphere because of deflection. Consequently, during periods of maximum solar activity, the

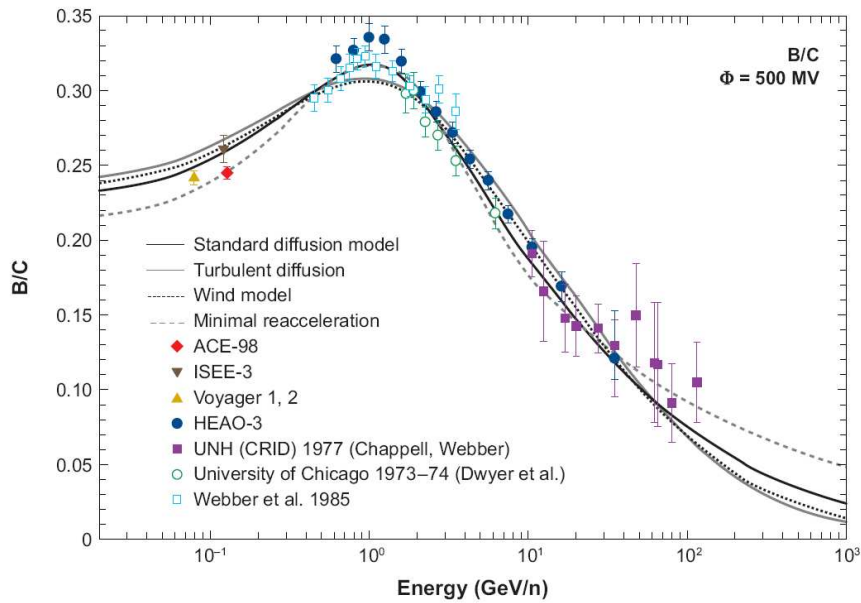


Figure 1.5. B/C ratio energy spectrum as measured by different experiments [19] compared to different propagation models of cosmic rays: standard diffusion model (solid line), turbulent diffusion model (dashed lines), convection model (dotted lines) and reacceleration model (dash-dotted lines); models are evaluated considering a solar modulation parameter $\Phi = 500$ MV [17].

intensity of cosmic radiation which reaches the Earth is reduced. Also disturbances due to local solar activity, such as solar flares or coronal mass ejections, cause irregularities in the flow of the solar wind and the associated magnetic field and can interfere with the propagation of low energy cosmic rays to Earth. Thus, the flux of low energy particles decreases during periods of high solar activity and reaches a minimum at the solar maximum and vice-versa. This effect is called *solar modulation* and can have a significant effect on cosmic rays with energies less than ~ 10 GeV/nucleon [22].

The sinusoidal time dependence of the solar activity and of the cosmic ray flux is clearly visible on figure 1.6. Cosmic ray data are derived from neutron monitors located at different points on the globe (Neutron Monitor Network [23]). As introduced at the beginning of this chapter, when cosmic rays enter the atmosphere they collide with the molecules of atmospheric gases and produce a cascade of lower energy secondary particles. The neutrons produced by interactions of cosmic rays in the atmosphere are called *atmospheric neutrons*. They are generated in hadronic and electromagnetic air showers by spallation and evaporation processes on nitrogen and oxygen nuclei, which are the predominant elements in the Earth's atmosphere [24]. In spallation processes neutrons are produced by the fragmentation of a nucleus inelastically scattered by a cosmic ray particle, while in evaporation processes neutrons are produced by the electromagnetic interaction of a cosmic ray particle with atmospheric nuclei. Since the neutron mean lifetime is long (~ 15 minutes [25]) they do not decay before reaching the ground and thus the neutron flux detected on the ground is directly proportional to the flux of galactic cosmic rays arriving at the top of the atmosphere. Figure 1.6 shows clearly the anticorrelation between cosmic ray flux and solar activity. During periods of maximum solar activity the flux of cosmic ray particles on the Earth is attenuated. This effect is also visible in the galactic proton flux measured by the PAMELA detector during the years 2006–2009 as shown in figure 1.7.

Furthermore, at each solar maximum the polarity of the solar magnetic field reverses leading to alternating magnetic polarity in successive solar cycles. Thus, a complete solar cycle is 22 years long. The heliospheric current sheet is the surface in the solar wind that separates magnetic polarities. It is tilted with respect to the solar equator by an angle that varies from about 10° at minimum solar activity to more than 70° during high solar activity [28]. The magnetic dipole projection on the solar rotational axis and the rotational axis itself can be either parallel ($A > 0$ phase) or antiparallel ($A < 0$ phase). The combination of Sun's rotation and solar wind radial expansion distorts the current sheet into a wavy shape that is responsible for greater modulation during high solar activity (see figure 1.8-left). The most recent reversal of the solar magnetic field from an $A > 0$ to an $A < 0$ configuration took place during year 2000. Cosmic ray propagation to Earth is also affected by this magnetic polarity change. Particles with opposite charge drift in opposite directions in the heliospheric magnetic field causing a charge sign dependence. According to drift theory, positively charged particles enter the inner heliosphere primarily via the polar regions during an $A > 0$ phase and mainly via

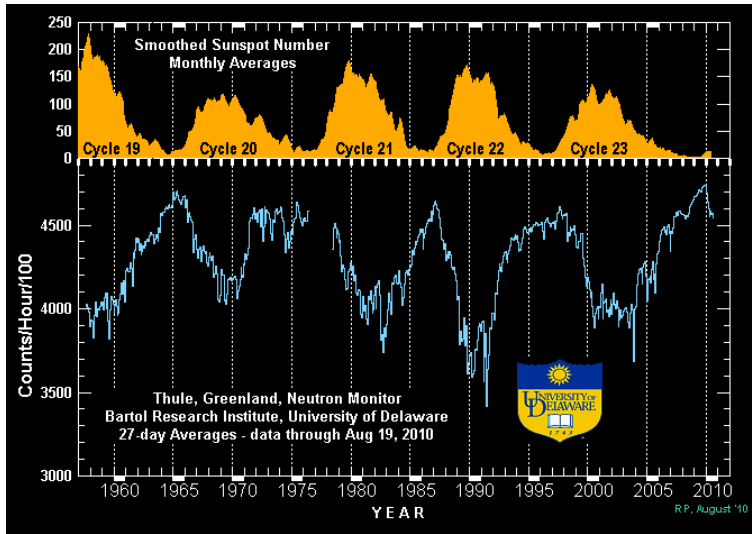


Figure 1.6. The sinusoidal time dependence of the solar activity (yellow line) compared to the count rate recorded by a neutron monitor detector in Thule, Greenland (blue line) [26].

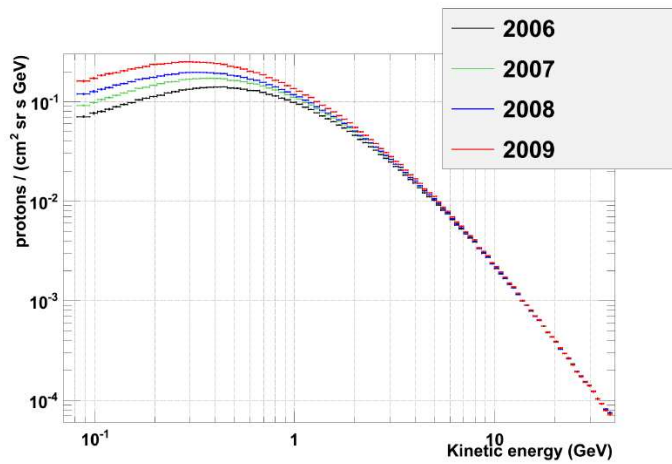


Figure 1.7. Proton absolute flux measured by the PAMELA experiment in 2006, 2007, 2008 and 2009. The effect of solar modulation is clearly visible [27].

the equatorial regions along the heliospheric current sheet during an $A < 0$ phase. The phenomenon acts in an opposite way for negatively charged particles [29]. This configuration is shown in figure 1.8-*right*. Thus, due to this effect positive particles are favoured during an $A > 0$ solar magnetic field phase and are instead suppressed during an $A < 0$ phase [30].

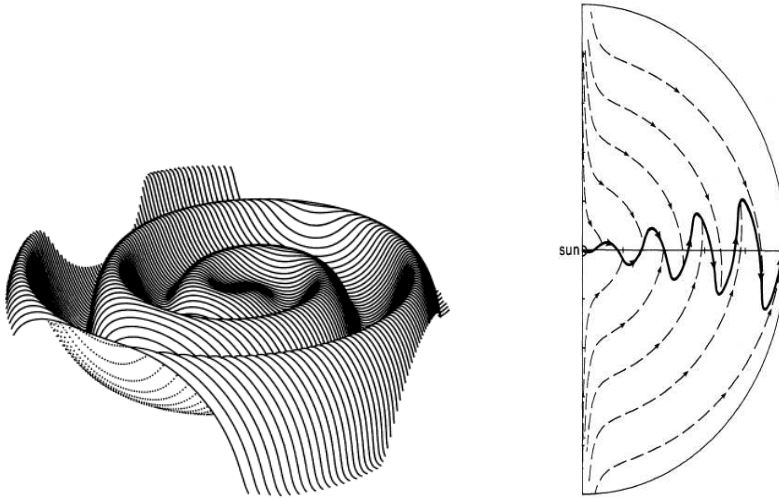


Figure 1.8. *Left:* a representation of the heliosphere current sheet as seen by an observer 30° above the equatorial plane and 75 AU from the Sun [30]; the Sun is shown at the centre and the figure is 25 AU across. *Right:* drift trajectories for 2 GeV protons in an $A > 0$ solar magnetic field configuration. The tick marks are at 5 AU intervals. The direction of the arrows changes for an $A < 0$ phase or for negative charged particles [30].

1.5 Cosmic ray positrons and electrons

As already mentioned at the beginning of this chapter, electrons account for $\sim 2\%$ of the cosmic ray particles. The proton-to-positron flux ratio is $\sim 10^3$ at 1 GV and increases to $\sim 10^4$ at 100 GV [31]. Even if electrons and positrons are very few compared to protons, they are of great interest nowadays because of the astrophysical questions they could answer. Since they lose energy very efficiently as they propagate they could give useful information about acceleration mechanisms and propagation processes of cosmic rays in the local part of our galaxy.

Positrons are believed to be mainly secondary particles, produced during interactions of primary cosmic ray nuclei with the interstellar medium. When primary cosmic ray protons interact with protons of the interstellar gas, charged pions and kaons are produced; thus secondary positrons are decay products of π^+ and K^+ .

The so called *positron fraction*, defined as the ratio between the positron flux and the sum of positron and electron flux,

$$\frac{\Phi(e^+)}{\Phi(e^+) + \Phi(e^-)} \quad (1.8)$$

and obtained from models considering a pure secondary positron production and with or without reacceleration processes has been studied for instance by Moskalenko and Strong [32] (see figure 1.9). According to these models the positron fraction

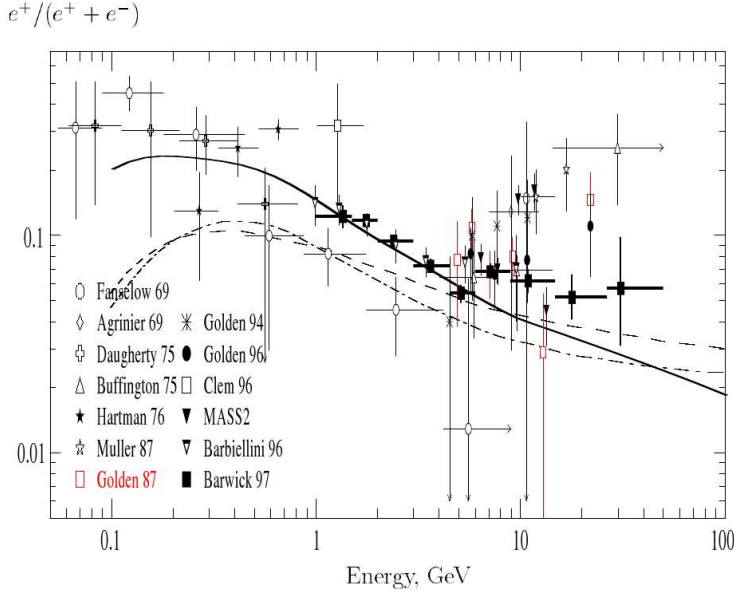


Figure 1.9. Positron fraction as measured by several experiments before PAMELA data [33]. Experimental data are compared to a pure secondary positron production model without reacceleration processes evaluated by Moskalenko and Strong [32] (black solid line); predictions for the positron fraction considering a leaky-box model (dashed-dot line) and a diffusion model (dashed line) [34] are also shown.

is expected to decrease as the energy increases and this trend is consistent with experimental data up to 10 GeV. For energies greater than 10 GeV data collected during the 90's possibly show an excess with weak statistical significance above the predicted ratio, although the observational errors are large and there are not so many measurements at higher energies [32].

Positrons could be also created as primary particles in high energy astrophysical sources, such as in the magnetosphere of near-by pulsars and supernova remnants, or be produced by dark matter particle annihilations. Electrons can be accelerated in the magnetosphere of pulsars, magnetized neutron stars with high spin rate.

In pulsar magnetic fields, about $10^6 - 10^9$ T [14], electrons lose energy via synchrotron radiation and consequently photons are produced; these photons can then produce pairs of electrons and positrons with lower energies. These particle pairs are then accelerated and confined in the pulsar nebula for $\sim 10^5$ years before escaping into the interstellar medium. The energy spectrum of these primary positrons is expected to be harder than that of the secondary ones with a spectral index of about 1.5 - 1.6 according to Zhang and Cheng [35]. Thus, positrons originating from pulsars may dominate the high energy end of the cosmic ray positron spectrum. Only pulsars at a distance of 1 kpc or closer can contribute significantly to the positron energy spectrum due to the energy losses during the propagation into the interstellar medium [36]. For instance, it has been estimated by Hooper et al. [37] that at 10 GeV only ~ 20 % of the cosmic rays positrons originate from pulsars within 500 pc from the Solar System; furthermore, above ~ 50 GeV the positron spectrum seems to be dominated by a single or small number of nearby pulsars.

Beside astrophysical sources, primary positrons could be produced also via annihilation of dark matter particles. Nowadays it is known that baryonic matter accounts only for 4 % of the total energy density of the Universe; the remaining is shared among dark matter (~ 23 %) and dark energy (~ 73 %). WIMPs are one of the favourite candidates for the dark matter component of the Universe. They are expected to form a halo around the disk and the bulge of our galaxy. Two examples of WIMP particles are the *neutralino*, a Majorana fermion in the supersymmetric scenario of the particle standard model, and the lightest *Kaluza-Klein* particle in the Universal Extra Dimension model. In this last scenario, primary positrons could be produced via annihilation of some Kaluza-Klein dark matter particles, for instance through the process $\chi\chi \rightarrow e^+ e^-$.

1.5.1 PAMELA positron fraction

The PAMELA detector has been collecting data since July 2006. One of the first results obtained by the Collaboration concerned the positron fraction measured between 1.5 and 100 GeV. This result is based on the data collected between July 2006 and February 2008, and more than 10^9 triggers have been acquired during a total acquisition time of ~ 500 days [31]. Another important result regards the measurement of the cosmic ray electron flux in the energy interval 1 - 625 GeV. This result is based on the data set collected up to January 2010 during a total acquisition time of ~ 1200 days [38] (see section 1.5.2).

In figure 1.10-*top* the PAMELA positron fraction is shown together with a theoretical trend for pure secondary positron production during the propagation of cosmic rays in the galaxy [31]. Comparing PAMELA data with those obtained from other experiments (figure 1.10-*bottom*) two disagreements are evident at lower and higher energies.

The difference at low energy is interpreted as a consequence of solar modulation effects. As explained in section 1.4 the solar wind affects the energy spectra of cosmic rays within the solar system. The most recent reversal of the solar magnetic field took place during year 2000 and it is clearly visible in the antiproton-to-proton

flux ratio as measured by several flights of the BESS balloon-borne experiment between 1997 and 2000 [39]. CAPRICE94, HEAT95 and AMS-01 data (figure 1.10-*bottom*) have been collected during the previous solar cycle which favoured positively charged particles, explaining in this way the higher positron fraction at lower energies comparing to the PAMELA one. Furthermore, data collected during June 2006 by the AESOP balloon-borne experiment [40] show also a lower positron fraction at low energies compared to data collected before year 2000 (figure 1.10-*bottom*) in agreement with PAMELA data. Thus, the low energy PAMELA data show the most statistically significant charge-sign dependence for solar modulation to date [31].

At high energies, above 10 GeV, the PAMELA positron fraction increases clearly with energy. The theoretical calculations performed considering a pure secondary production of positrons during the propagation of cosmic rays in the galaxy [32] is not able to fully describe PAMELA data. A study about uncertainties on this model have been carried on by Delahaye et. al. [41]. This study concerns uncertainties on nuclear cross-section, effects induced by primary electron injection spectra and models of propagation throughout the galaxy. Considering these uncertainties and a soft electron spectrum with spectral index -3.53 [41], it seems that PAMELA data could be explained by the standard secondary production. However, PAMELA measurements of the electron spectrum indicate a hard spectral index of -3.18 ± 0.05 [38]. On the other hand, changing the injection spectral index of primary electrons, i.e. for a harder electron spectrum with spectral index -3.35 , PAMELA data show an excess above ~ 10 GeV [41]. This means that either a significant modification in the acceleration and propagation models for cosmic rays is needed or a primary component is present. Even if the reason for this rise is still unclear, many models have been proposed in order to explain PAMELA data. These models concern astrophysical sources, mostly pulsars, or the annihilation of dark matter particles (see section 1.5.3).

1.5.2 PAMELA electron flux

The electron flux measured by the PAMELA experiment in the energy interval $1 - 625$ GeV is shown in figure 1.11-*top* (red points) [38]. The PAMELA electron energy spectrum is also compared with the following measurements: CAPRICE94 [42], HEAT [43], AMS-01 [44], MASS91 [45], Kobayashi [46], BETS [47], ATIC [48], HESS [49] and Fermi [50]. It is important to remark that measurements from [46]–[50] (blue symbols) corresponds to the electron and positron sum. In figure 1.11-*bottom* the PAMELA electron flux is compared with a secondary production model including diffusion and reacceleration processes [32] (solid line). PAMELA data are well represented by a single power law fit with spectral index -3.18 ± 0.05 (long dashed line). This is compatible with a soft electron spectrum, as required to explain the measured PAMELA positron fraction considering a standard diffusion reacceleration model of cosmic ray propagation [38]. Measurements have been also fitted with a model considering standard secondary electron production and additional cosmic ray electron sources (short dashed line).

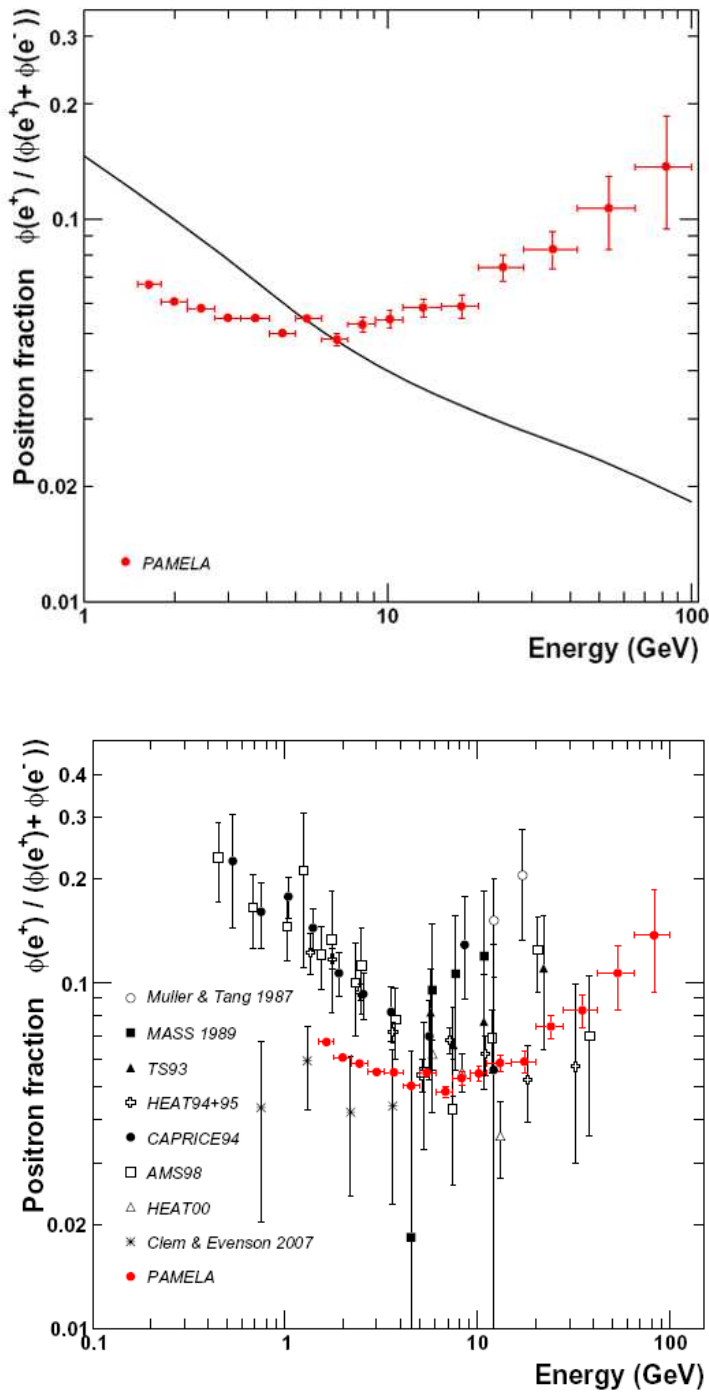


Figure 1.10. *Top:* the positron fraction as measured by the PAMELA experiment; the error bars corresponds to one standard deviation. The solid line represents the theoretical fraction for pure secondary positron production considering diffusion and convection as propagation mechanisms without reacceleration processes [31], [32]. *Bottom:* comparison between the PAMELA positron fraction (red points) and other recent experimental data [31].

Differences in the spectrum above 10 GeV are visible and this may indicate that changes in the propagation model or additional sources of cosmic ray electrons are needed.

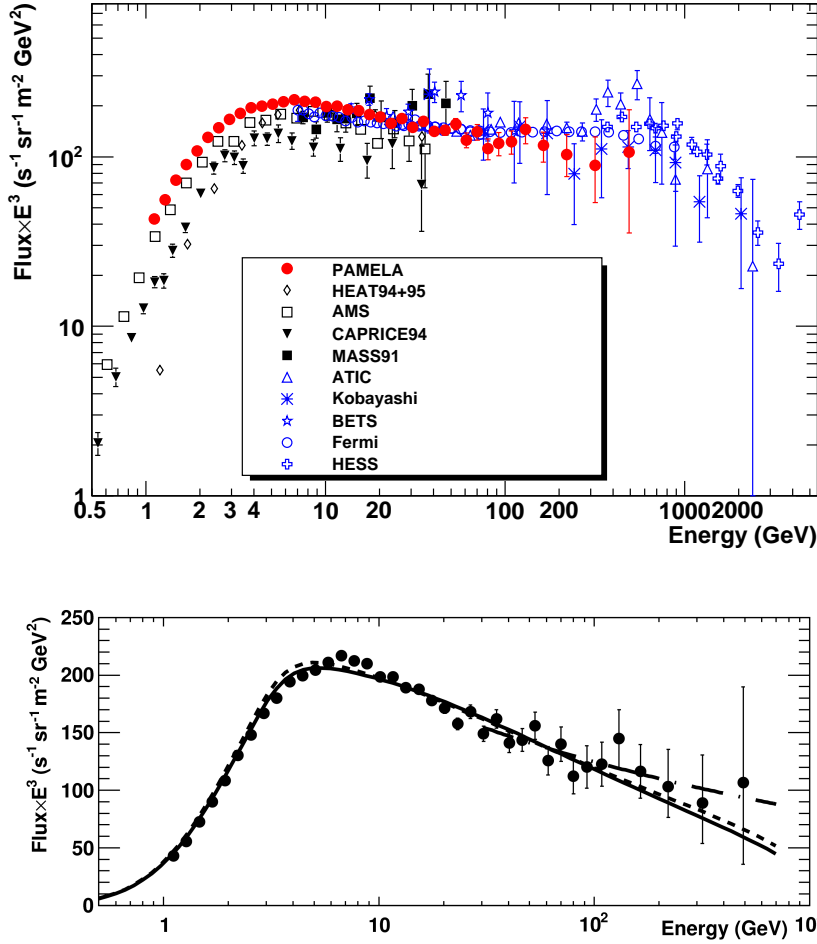


Figure 1.11. *Top:* the electron flux as measured by the PAMELA experiment (red points) [38] compared with other experimental data: CAPRICE94 [42], HEAT [43], AMS-01 [44], MASS91 [45], Kobayashi [46], BETS [47], ATIC [48], HESS [49] and Fermi [50]. The measurements indicated by blue points refer to electron and positron sum [38]. *Bottom:* the PAMELA electron flux (black points) compared with a standard diffusion reacceleration model [32] (solid line); data above 30 GeV are fitted with a single power law (long dashed line) with spectral index -3.18 ± 0.05 ; data are also compared with a model including additional cosmic ray electron sources (short dashed line) [38].

1.5.3 Theoretical interpretations

Direct measurements of the positron and electron energy spectra are very important for constraining parameters of different theoretical models which describe cosmic ray production and propagation in the galaxy. While at energies less than ~ 10 GeV cosmic ray spectra are deformed by solar modulation (see section 1.4), at higher energies spectra are mainly modulated by three effects: source spectral index, synchrotron and Inverse Compton energy losses and diffusion in the galactic magnetic field [51]. Thus, measurements of the high energy part of positron and electron spectra are of most interest in distinguishing between different theoretical models. Considering only a conventional model accounting for diffusion and for reacceleration processes, it is not possible to fully reproduce both the electron-plus-positron energy spectrum as measured by the Fermi-LAT experiment [50] and the positron fraction as measured by the PAMELA experiment [31] (see figure 1.12 [52]).

As already mentioned, pulsar magnetospheres could be sources of primary cosmic ray positrons. Some studies performed by Hooper et al. [37] show that PAMELA positron fraction can be well reproduced considering positrons produced by the sum of all pulsars in our galaxy (figure 1.13); in particular, the best fit is obtained for about one pulsar birth each ~ 25 years. An interesting model has been studied by Grasso et al. [51] and theoretical predictions are shown in figure 1.12. In this model a diffusion reacceleration standard model of cosmic ray electrons have been considered together with a contribution of nearby pulsars. In particular pulsars within a distance smaller than 1 kpc and an age larger than $5 \cdot 10^4$ years have been included in the calculations. This study shows also that only the Monogem and Geminga pulsars give a significant contribution to the high energy positron and electron flux [51]. Figure 1.12 shows that this model well fits both the electron-plus-positron energy spectrum as measured by the Fermi-LAT experiment [50] (figure 1.12-*top*) and the positron fraction as measured by the PAMELA experiment [31] (figure 1.12-*bottom*).

Many different interpretations of PAMELA data regard also production of positrons by annihilation of dark matter particles. Already in 1991 Kamionkowski and Turner postulated a rise in the positron fraction due to the annihilation of WIMP particles in the galactic halo [53]. Nowadays, PAMELA results pose a theoretical challenge in finding a model which describes both the rise in the positron fraction at energies greater than ~ 10 GeV and the antiproton-to-proton flux ratio [21] which is instead well described by a pure secondary positron production. Dark matter annihilation processes produce antiprotons and protons in addition to positrons and electrons. Thus, the antiproton-to-proton ratio as measured by PAMELA [21] sets stringent constraints on the annihilation dark matter modes. For instance, a study conducted by Cirelli et al. [54], requires a very high neutralino mass ($M > 10$ TeV), which is not allowed by most supersymmetric models. Furthermore, neutralinos suffer helicity suppression in the annihilation process resulting in a softer positron spectrum than the one observed by PAMELA. To overcome this problem, many theories have been proposed. One of them requires neutralino annihilation into leptons (mainly $\chi\chi \rightarrow e^+ e^- \gamma$) and radiative corrections for propagation effects.

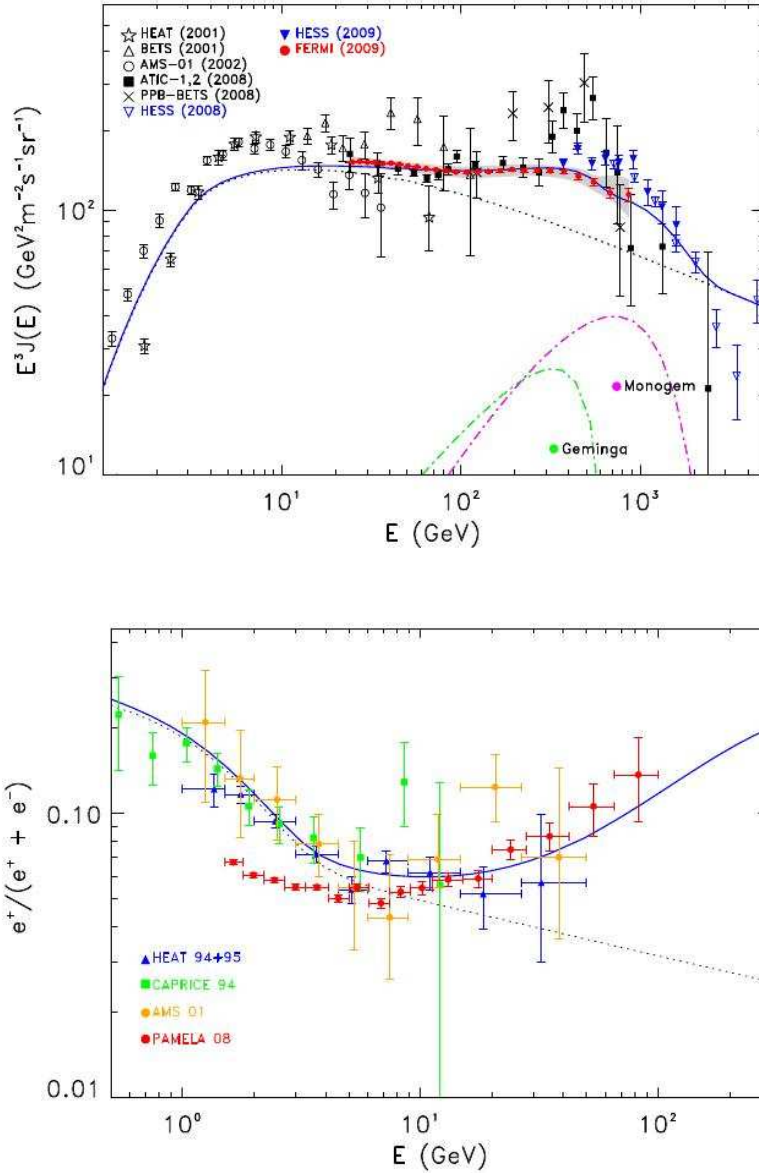


Figure 1.12. *Top:* electron-plus-positron energy spectrum as measured by the Fermi-LAT experiment (red points) [50] compared with other measurements; systematic errors are also shown (grey band). Fermi-LAT data are compared with a theoretical computation (blue line) which considers pulsars within a distance smaller than 1 kpc and an age larger than $5 \cdot 10^4$ years and a diffusion reacceleration standard model (dotted black line). The significant contribution from Monogem (purple line) and Geminga (green line) pulsars is also shown [52].

Bottom: positron fraction as measured by PAMELA (red points) [31], CAPRICE94 [42], HEAT [43] and AMS [44] experiments; the positron fraction is also compared with a theoretical predictions (blue line) which considers pulsars within a distance smaller than 1 kpc and an age larger than $5 \cdot 10^4$ years and a diffusion reacceleration standard model (dotted black line) [52].

This results in a harder positron spectrum (figure 1.14) with a negligible impact on the antiproton spectrum [55]. Other models consider *Kaluza-Klein* particles: for instance, a lightest Kaluza-Klein particle is a boson that can annihilate directly into positron-electron pairs without helicity suppression [56].

New experimental data from the AMS-02 experiment [57] are expected soon. The AMS-02 experiment will provide measurements with a higher maximum energy cut-off compared to PAMELA. Moreover, in order to further extend positron measurements in the TeV scale, the PEBS long-duration electron positron balloon-borne mission has been proposed [58]. New results about positron and electron flux will be interesting in this scenario. The future data, together with the present ones, will probably provide a better understanding of all these open questions.

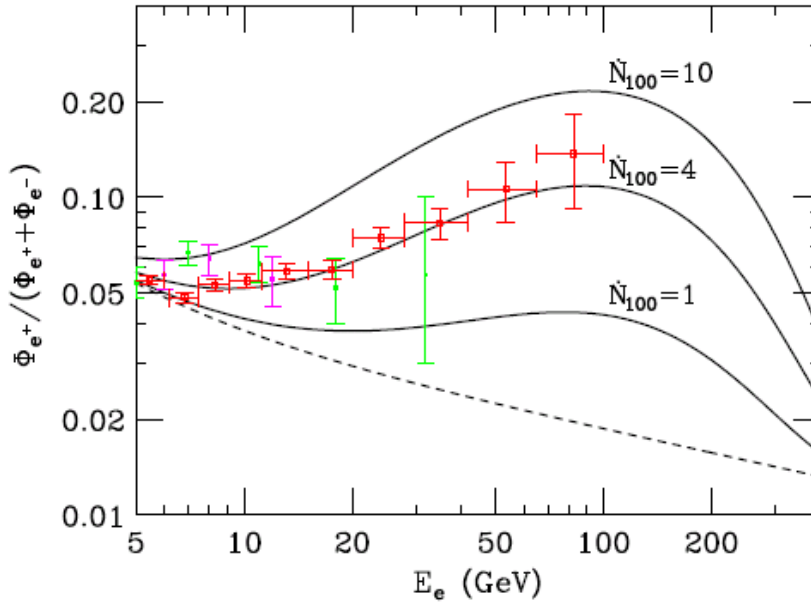


Figure 1.13. Positron fraction measured by the PAMELA experiment (red points) compared to theoretical positron fraction (black lines) resulting from the sum of all pulsars in our galaxy within 500 pc of the Solar System. Calculations have been done considering different rates of pulsar birth: one per 10 years ($\dot{N}_{100} = 10$), one per 25 years ($\dot{N}_{100} = 4$) and one per 100 years ($\dot{N}_{100} = 1$). \dot{N}_{100} is the rate of pulsar formation in units of pulsars per century [37]. The theoretical prediction considering a pure positron secondary production is also shown (dashed line) [32]. Pamela results are compared to data obtained by the HEAT experiment (green points) [33].

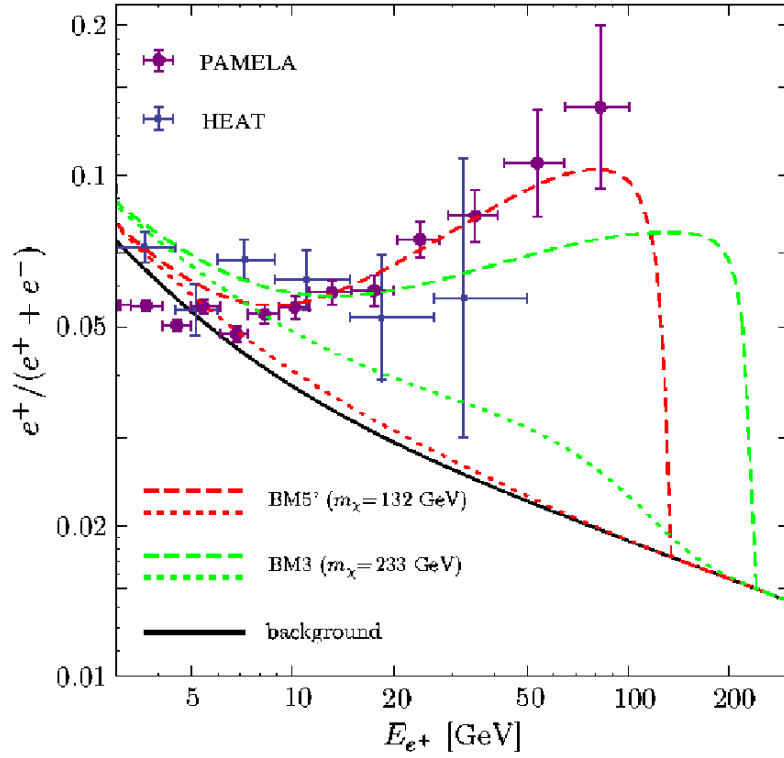


Figure 1.14. Positron fraction measured by the PAMELA experiment (violet points) compared to theoretical positron fraction considering dark matter particle annihilation models (green and red lines). The models taking into account different neutralino masses with radiative corrections (dashed lines) or without radiative corrections (dotted lines) [55]. The theoretical prediction considering a pure positron secondary production is also shown (black solid line) [32]. Pamela results are compared to data obtained by the HEAT experiment (blue points) [33].

Chapter 2

The PAMELA experiment

PAMELA (**P**ayload for **A**ntimatter **M**atter **E**xploration and **L**ight-nuclei **A**stro-**physics**) is a satellite-borne experiment mounted on board of the Russian Resurs DK1 satellite. It was launched from the Baikonur cosmodrome in Kazakhstan on June 15th 2006. The satellite acquires high-quality images of the Earth's surface. Its mass is ~ 6.7 tonnes and its height is 7.4 m. The satellite orbit is elliptical and semi-polar and its altitude varies between 350 km and 600 km with an inclination of 70° . An overview of the Resurs DK1 satellite is shown in figure 2.1.

The PAMELA experiment is mounted in a pressurized container attached to the Resurs DK1 satellite (figure 2.1). It has been designed to study charged cosmic rays particles and mainly antiparticles, *antiprotons* and *positrons*.

In this chapter a detailed description of the PAMELA experiment is presented together with a summary of the main scientific goals.

2.1 The PAMELA apparatus

The PAMELA apparatus has an height of ~ 1.3 m, a mass of 470 kg and an average power consumption of 355 W. It is formed by the following subdetectors:

- a time-of-flight system (ToF)
- a magnetic spectrometer (Tracker)
- an electromagnetic calorimeter
- a neutron detector
- an anticoincidence system (AC)

The geometrical acceptance of the experiment is $21.5 \text{ cm}^2 \text{ sr}$ and is determined by the geometry of the magnetic spectrometer cavity [59].

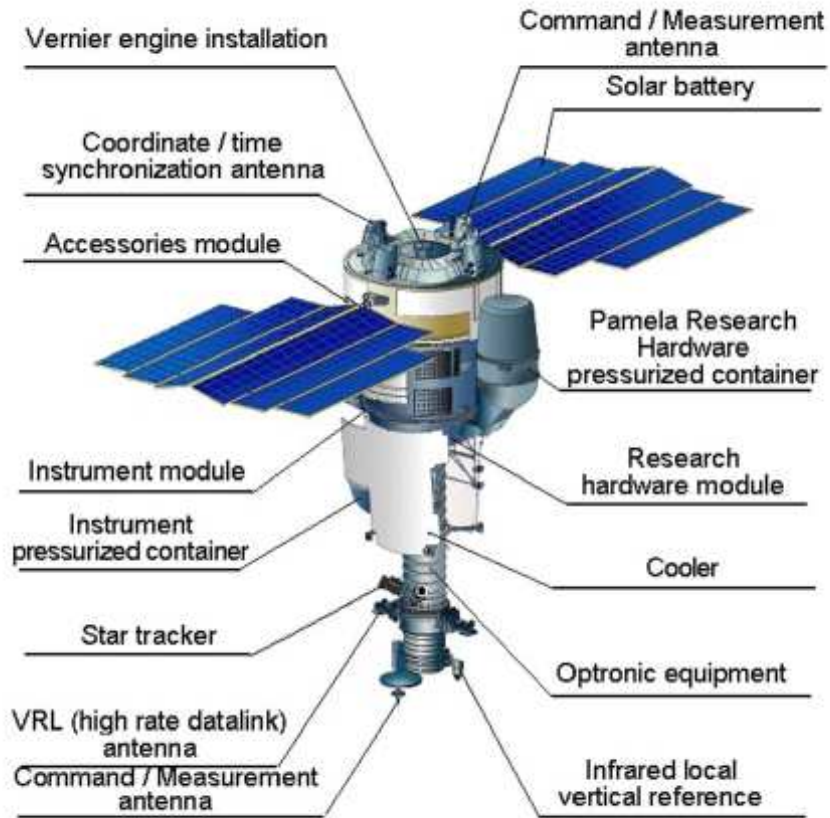


Figure 2.1. A schematic overview of the Resurs DK1 satellite which hosts the PAMELA experiment. The satellite has a mass of ~ 6.7 tonnes and a height of 7.4 m; the solar array span is ~ 14 m [59].

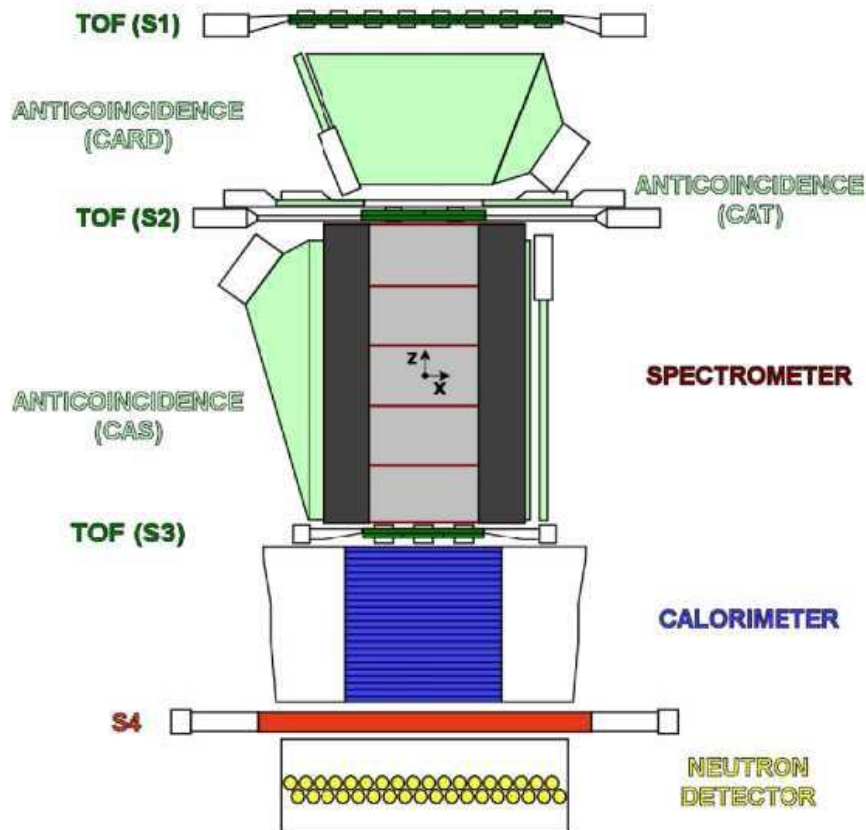


Figure 2.2. Schematic overview of the PAMELA detector. The instrument has an height of ~ 1.3 m, a mass of 470 kg and an average power consumption of 355 W [59].

2.1.1 The time-of-flight system

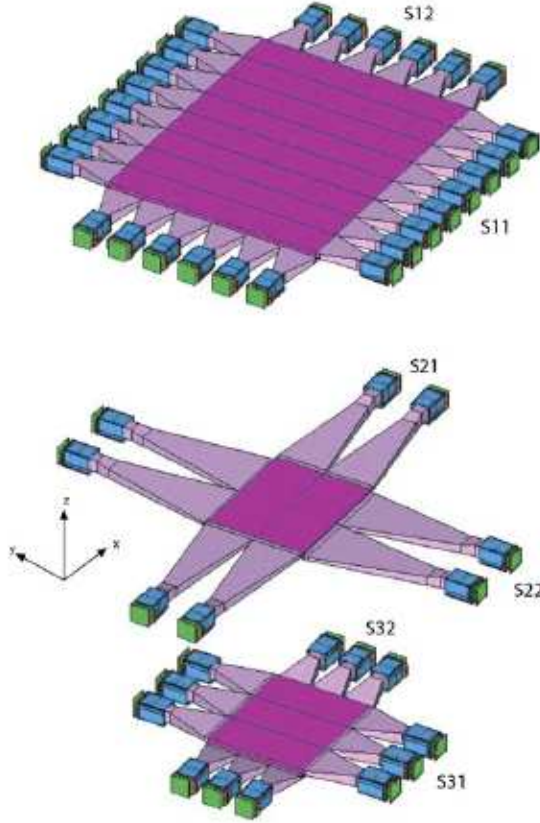


Figure 2.3. Schematic overview of the time-of-flight system. The distance between the scintillator planes S1 and S3 is 77.3 cm. S1 has a sensitive area of $(33 \times 40.8) \text{ cm}^2$. Both S2 and S3 have a sensitive area of $(15 \times 18) \text{ cm}^2$ [59].

The *time-of-flight system* (ToF) consists of three planes labeled as S1, S2 and S3 and arranged as shown in figure 2.2. The plane S1 is situated on the top of the apparatus, S2 lies above the magnetic spectrometer while S3 lies between the spectrometer and the calorimeter; the distance between S1 and S3 is 77.3 cm. Each plane is formed by two fast plastic scintillators layers (Bicron BC-404) placed orthogonal to each other (figure 2.3). The two S1 layers, so-called S11 and S12, are divided into 8 and 6 bars respectively with a thickness of 7 mm and a total sensitive area of $(33 \times 40.8) \text{ cm}^2$. The S2 layers, S21 and S22, are segmented into 2×2 orthogonal bars with a thickness of 5 mm while S3 layers, S31 and S32, are segmented into 3×3 orthogonal bars. Both the planes S2 and S3 have a sensitive

area of $(15 \times 18) \text{ cm}^2$. Each of the ToF scintillator bars are glued at the ends to a plastic light guide which is read out by a photomultiplier (Hamamatsu R5900U).

The ToF system acts as the main PAMELA trigger by measuring the coincidental energy deposits in the scintillators. The measurement of the ionisation energy loss (dE/dx) in the scintillator planes determines the absolute value of charge, z , of the incident particles. Furthermore, the ToF measures the flight time of the particles passing through its planes: this information is combined with the track length derived from the spectrometer in order to derive the velocity β of incident particles. This also permits up-going particles, so-called albedo particles, to be rejected, excluding in this way misidentification between a particle and an antiparticle due to the bending of the spectrometer magnetic field. The flight time for a 1 GeV/c electron is 2.7 ns and for 1 GeV/c proton is 3.7 ns. Thus, since the time resolution is about 250 ps, the ToF allows to discriminate between electrons and antiprotons, or protons and positrons, up to $\sim 1 \text{ GeV}/c$ [59], [60].

An extra scintillator plane, S4, is situated just under the calorimeter. It consists of a single scintillator plane of 1 cm thickness and an area of $(48 \times 48) \text{ cm}^2$ and it is read out by six photomultipliers. The main task of this scintillator plane is to detect showers which are not fully contained in the calorimeter improving in this way the electron-hadron separation performance of the all instrument.

2.1.2 The magnetic spectrometer

The magnetic spectrometer, or tracker, consists of a permanent magnet and six silicon detector planes (figure 2.4). The magnet has a tower which is 44.5 cm high and composed of five identical modules. Each module comprises twelve magnetic blocks made of a Nd-Fe-B alloy with a residual magnetisation of 1.3 T. These five modules form a rectangular cavity $(13.1 \times 16.1) \text{ cm}^2$ which defines the geometrical factor of the PAMELA experiment to be $21.5 \text{ cm}^2 \text{ sr}$. The modules are also configured to provide an almost uniform magnetic field oriented along the y-direction with a mean value of 0.43 T inside the cavity and a value of 0.48 T at the centre. Furthermore, the magnet is enclosed by ferromagnetic shielding in order to attenuate the stray field outside of the cavity which could interfere with the satellite instruments.

Six 300 μm thick silicon detector planes are inserted inside the magnetic cavity separated by 8.9 cm. Each plane is formed by three ladders inserted into an aluminium frame which connects to the magnetic cavity. One ladder comprises two double sided sensors, $(5.33 \times 7.00) \text{ cm}^2$, with implanted strips orthogonal to each other on the two sides. This provides two independent impact coordinates on each plane. Also, no additional supporting structure is present above or below the planes in order to limit multiple scattering in dead layers [61].

The magnetic spectrometer allows charged particle deflection η to be measured as well as the rigidity R which is defined as $\eta = 1/R$. The momentum of a particle and the sign of its electric charge are then evaluated via the relation $R = c \cdot p / Z \cdot e$,

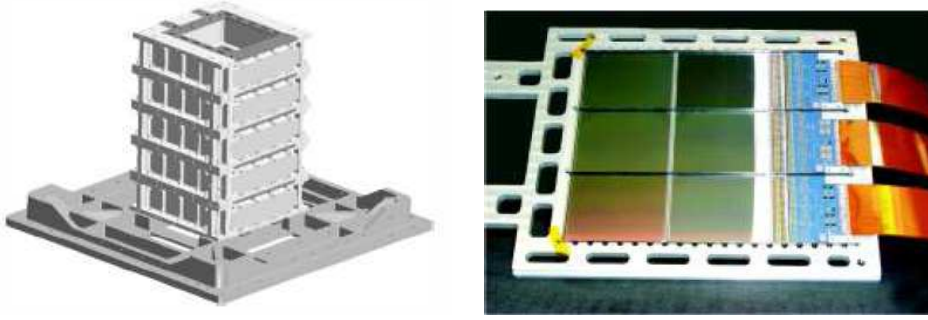


Figure 2.4. *Left:* design of the five modules which constituted the PAMELA magnet. The tower is 44.5 cm high and the rectangular cavity is (13.1×16.1) cm² [61]. *Right:* picture of a silicon plane (300 μ m thick) inserted in the magnetic spectrometer cavity: the three silicon strip detectors and the front-end electronics are visible; each silicon detector has a surface of (5.33×7.00) cm² [62].

where e is the electron charge, p is the momentum, c is the speed of light and Z is the absolute charge.

The resolution of the deflection measurement depends on several factors: the geometry of the spectrometer, the intensity of the magnetic field and the spatial resolution of the detector silicon sensors. Tests performed with particle beams show a spatial resolution of (3.0 ± 0.1) μ m in the bending x -view (figure 2.5-*top*), and (11.5 ± 0.6) μ m in the non-bending y -view obtained for normally incident tracks. The resulting deflection measurement error as a function of the rigidity obtained with proton beams is shown in figure 2.5-*bottom*: this determines the *maximum detectable rigidity*, MDR, to be ~ 1 TV. The MDR is defined as 100 % uncertainty in the particle rigidity measurement [63].

While the MDR sets an upper rigidity limit for detecting cosmic ray particles such as protons, helium nuclei and heavier nuclei, the upper rigidity limit for the detection of their antiparticles is complicated by their low abundance in cosmic radiation. As the rigidity increases, the tracks approach a straight line in the tracker. Thus, a high rigidity particle can be assigned an opposite charge. This phenomenon is called *spillover* and causes a non-negligible background when measuring antiparticles at high energy. Spillover effects limit the upper detectable momentum to about 190 GeV/c for antiprotons and to about 270 GeV/c to positrons (see table 2.1) [59].

2.1.3 The electromagnetic calorimeter

The electromagnetic calorimeter (see section 3.4 for a further description) is formed by 44 single-sided silicon sensor planes interleaved with 22 plates of tungsten absorber. Each silicon plane is 380 μ m thick while each tungsten layer has a thickness of 0.26 cm which corresponds to 0.74 X_0 (*radiation lengths*). Thus, the total depth

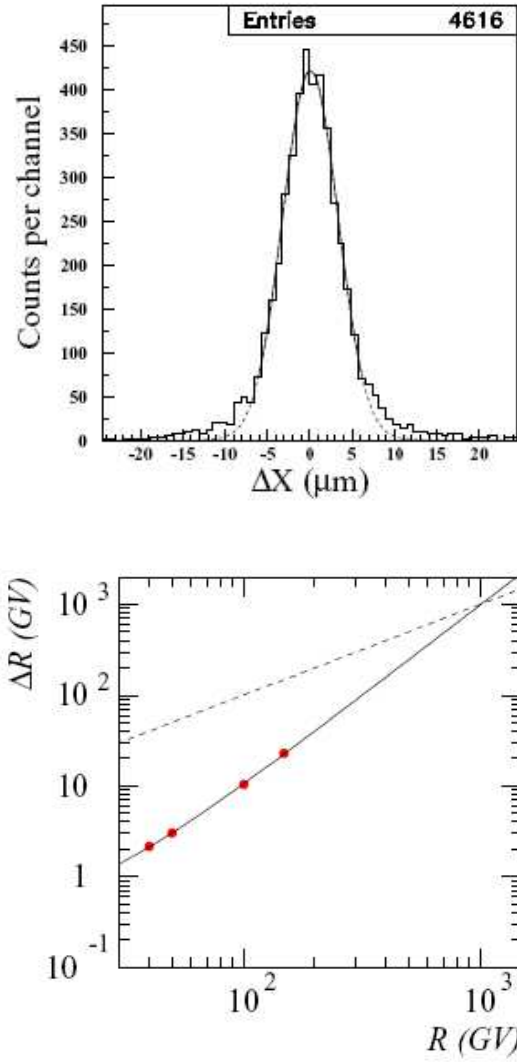


Figure 2.5. *Top:* the tracker spatial resolution in the bending x -view fitted by a Gaussian distribution. *Bottom:* the deflection error ΔR measured by the magnetic spectrometer as a function of R obtained with proton beams. The dashed line is the bisector $\Delta R = R$; the fitted function (solid line) depends on the multiple scattering and on the spatial resolution which both contribute to the deflection uncertainty. The intersection of the two curves gives the maximum detectable rigidity of the spectrometer, $\text{MDR} \sim 1 \text{ TV}$ [59].

of the calorimeter is $16.3 X_0$, corresponding to ~ 0.6 nuclear interaction lengths. Each silicon detector has a sensitive area of (8×8) cm² and is segmented into 32 read-out strips with a pitch of 2.4 mm. The silicon detectors are then arranged in a 3×3 matrix thus forming a total sensitive area of about (24×24) cm². Also, all the silicon strips are connected creating 24 cm long strips. The strips of two consecutive layers are orthogonal (x -view and y -view) and therefore provide two-dimensional spatial information. The signals are read out using six CR1.4P chips per plane with the outputs multiplexed into a single 16-bit ADC; also, the read-out is divided into four independent sections, corresponding to the x -even, y -even, x -odd and y -odd planes [64]. Figure 2.6 shows a picture of one single detection module and the whole detector.

The main aim of the calorimeter is to identify positron and antiproton events over large backgrounds of protons and electrons respectively. Since electromagnetic and hadronic showers differ in their longitudinal and transversal profile and energy distributions, a powerful way to distinguish these two events is to analyse the shower development inside the calorimeter. The PAMELA electromagnetic calorimeter was designed in order to reach this goal: its longitudinal (Z) and transverse segmentation (X and Y) described above (coordinate system related to figure 2.2), combined with the measurement of the particle energy loss in each silicon strip, allows reliable identification of electromagnetic and hadronic showers. The electron-hadron separation performance has been studied and it has been found that it provides a proton rejection factor of $\sim 10^5$ keeping 90 % efficiency in selecting electrons and positrons; an electron rejection factor of $\sim 10^5$ in antiprotons selections has been found too [59].

2.1.4 The neutron detector

The neutron detector is situated below the S4 scintillator plane. It consists of 36 counters filled with ³He and organized into two planes of 18 counters each. It is also enveloped by a polyethylene moderator in order to prevent thermal neutrons entering from the sides and from the bottom of the detector. The total size of the neutron detector is $(60 \times 55 \times 15)$ cm³.

2.1.5 The anticoincidence system

The anticoincidence system consists of

- four plastic scintillators surrounding the sides of the magnetic spectrometer (CAS);
- one plastic scintillator covering the top of the spectrometer (CAT);
- four plastic scintillators surrounding the volume between the first two time-of-flight planes, S1 and S2 (CARD).

The CARD detectors geometry is the same of the CAS ones but with a reduced surface area. The CAT detector has a hole in the center corresponding to the



Figure 2.6. *Top:* picture of one *detection module* described in the text (see also section 3.4); the 3×3 matrix of silicon strips with a size of (24×24) cm² is clearly visible. *Bottom:* picture of the entire electromagnetic calorimeter [62].

spectrometer acceptance (figure 2.7). The anticoincidence plastic scintillators (Bicron BC-448M) are 8 mm thick and are read out by photomultipliers (Hamamatsu R5900U). Two photomultipliers are used for the CAS and CARD detectors in order to decrease the possibility of single point failure; for the same reason and due to its irregular shape the CAT detector is read out by eight photomultipliers.

The anticoincidence system is used to identify *false trigger events*. Simulations have shown that about 75 % of the triggers in orbit are generated by secondary particles produced via interactions of the primary ones with the PAMELA structures: for instance, events interacting into the calorimeter and backscattered or particles entering the apparatus from the side. These events are called false trigger events and they have to be removed during the offline data analysis.

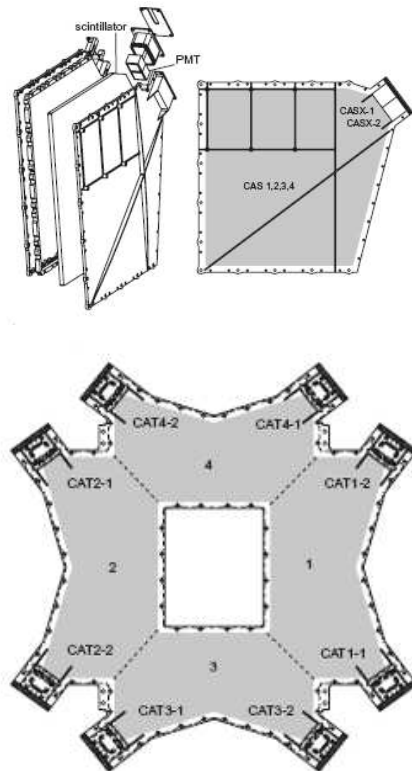


Figure 2.7. The anticoincidence system. *Top:* scheme of the CAS detector which surrounds the sides of the tracker. *Bottom:* scheme of the CAT detector which covers the top of the tracker; the hole in the centre corresponds to the tracker acceptance and measures (18×22) cm². The geometry of the CARD detector is the same of the CAS one but with a reduced surface area [59].

2.2 The PAMELA data acquisition system

A schematic view of the on-board Data Acquisition System (DAQ) is shown in figure 2.8. The Intermediate Data Acquisition System (IDAQ) reads out information from the subdetectors at a rate of 2 Mbytes/s, every time a trigger event is detected. Data are then stored in the PAMELA mass memory before being transferred to the satellite on-board memory several times per day. The downlinking to the Russian ground station in Moscow (NTsOMZ) takes place 2-3 times per day with a total transmission rate of ~ 16 Gbytes/day. The data are pre-processed in Moscow and then transferred via the GRID network from Moscow to the INFN facility at CNAF, Bologna (Italy).

The data acquisition and storage and all the communications with the satellite are control by the Pamela Storage and Control Unit (PSCU). The PSCU is constituted by four parts: two mass memory modules of 2 Gbytes, a CPU, the Pamela Interface Board (PIF) and the Telemetry and Control system (TMTC). The PIF performs communications with the IDAQ system and provides an interface to the mass memories and with the Very high-speed Radio Link (VRL) module of the satellite. The TMTC provides the housekeeping operations, like alarm, temperature and voltage monitoring. The PSCU organizes the data acquisition period in different runs, where each run corresponds to a continuous data taking in which the trigger and the detectors configurations are constant.

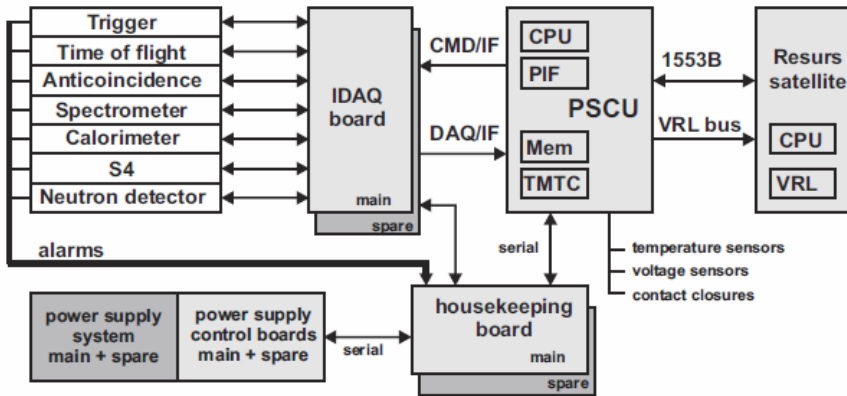


Figure 2.8. Scheme of the PAMELA Data Acquisition System (DAQ) [59].

2.2.1 The trigger configuration

The main PAMELA trigger is defined by the time-of-flight system when coincidental energy deposits are detected in its scintillator layers. There are two default configurations:

- (S11 or S12) and (S21 or S22) and (S31 or S32) \Rightarrow *outside* the radiation belts and the South Atlantic Anomaly (SAA) regions;
- (S21 or S22) and (S31 or S32) \Rightarrow *inside* the radiation belts and the SAA regions.

Inside the radiation environments the first ToF layer S1 is not considered because of the high counting rate that can saturate it. S2 and S3 can still be used as main trigger in these regions because they are more shielded. Other trigger configurations can be implemented and changed from ground. In figure 2.9 trigger rates observed during two consecutive orbits are shown: the maximum number of events per minute is detected in the polar regions (~ 35 Hz) while the minimum is detected around the Equator (~ 15 Hz). When the satellite passes through the SAA region the trigger rate increases up to ~ 70 Hz. The missing acquisition time after the SAA peak corresponds to the calibration time of the detectors. The calibrations of the anticounter, the tracker, the calorimeter and the S4 scintillator are performed by the PSCU when the satellite crosses the equator and it lasts about 1 minute [59]. Furthermore, the calorimeter is equipped with a self-trigger system which allows high energy electrons, between 300 GeV and ~ 1 TeV, to be detected. In order to collect sufficient statistics for these rare events it is necessary to have a large geometrical factor. Thus, the PAMELA geometrical factor is increased to ~ 600 cm² sr by requiring that particles enter only from one of the first four planes and cross at least 10 radiation lengths in the calorimeter [64].

2.3 PAMELA scientific goals

The PAMELA detector has been designed and optimised for the study of the antimatter component in the cosmic radiation. Compared to previous satellites or balloon-borne experiments, the PAMELA apparatus has increased significantly the statistics over a wider energy range in detecting cosmic rays particles and, mainly, antiparticles. The importance of antiparticle studies is linked to the production and propagation mechanisms of cosmic rays in the galaxy. Positrons and antiprotons are believed to be mainly created as secondary products in the interactions between cosmic ray nuclei and atoms in the interstellar medium [32]. High energy antiparticles could also be produced during annihilation or decay processes of dark matter particles, or be produced by nearby sources such as pulsars, for the positrons case. In table 2.1 the PAMELA design performances in detecting cosmic ray particles and antiparticles are shown (second column). The design performances are also compared to the energy ranges of the corresponding published

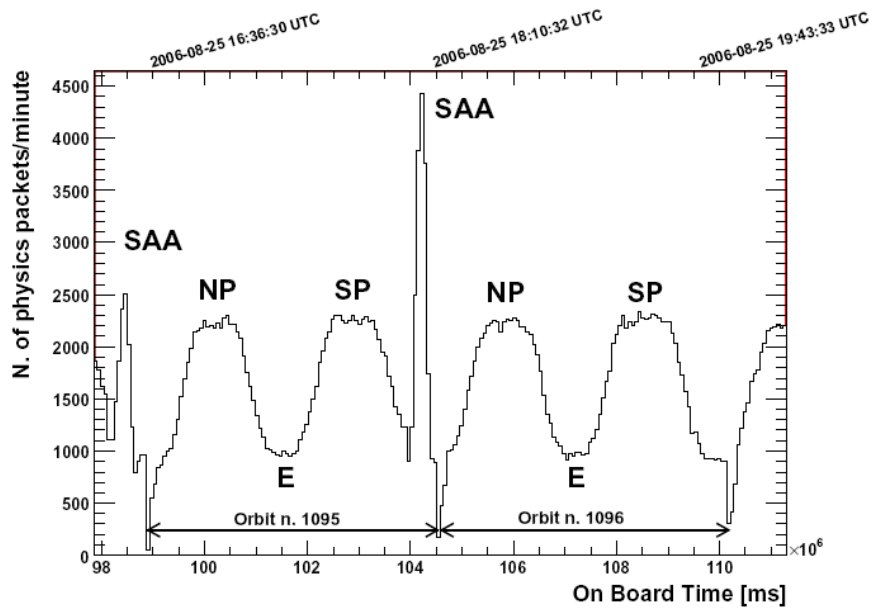


Figure 2.9. The PAMELA trigger rate during two consecutive orbits. The trigger rate is strongly dependent on the position of the satellite: the minimum is reached at the Equator (E) while the maximum at the North Pole (NP) or South Pole (SP); the highest peak corresponds to the South Atlantic Anomaly region (SAA). The missing acquisition time after the peaks of the SAA is due to the detector calibrations passing through the equator [59].

analysis (third column). The identification between particles and antiparticles is performed by combining information coming from the magnetic spectrometer and the electromagnetic calorimeter. Another important task is to measure the anti-helium/helium ratio with a sensitivity of the order of 10^{-7} . The detection of anti-helium nuclei would be a significant discovery and it could indicate the presence of antimatter domains in a baryon symmetric Universe. Furthermore, the reconstruction of electron spectra up to 2 TeV allows to investigate a possible contribution of local sources to the cosmic radiation. Solar physics and solar modulation of cosmic ray particles can be studied by analysing low energy particles, i.e. $\lesssim 10$ GeV.

Cosmic ray particle	Energy range
Antiprotons	80 MeV – 190 GeV
Positrons	50 MeV – 270 GeV
Electrons	50 MeV – 400 GeV
Protons	80 MeV – 700 GeV
Electrons + positrons	up to 2 TeV
Light nuclei ($Z \leq 6$)	100 MeV/n – 250 GeV/n
$\overline{\text{He}}/\text{He}$	$O(10^{-7})$

Table 2.1. PAMELA performances for the detection of cosmic ray particles and antiparticles [59]. Published PAMELA measurements are: the antiproton flux [65], the electron flux [38], the positron fraction [31], [66], and the proton and helium fluxes [67].

Chapter 3

Shower development in the PAMELA calorimeter

The PAMELA calorimeter is used to identify positron and antiproton events over a large background of protons and electrons respectively. Since leptons and hadrons interact in different ways, a powerful way to distinguish between these two types of events is to analyse the longitudinal and transverse shower profiles inside the calorimeter. An important characteristic of the hadronic showers is that neutral pions are produced during hadronic interactions and those π^0 rapidly decay into two photons thus initiating a component which propagates electromagnetically. This electromagnetic component becomes more prominent at high energies and could affect the discrimination between electromagnetic and hadronic showers in the calorimeter. In view of extending the positron fraction and the positron flux measurements up to ~ 300 GeV, the neutral pion contamination of hadronic showers and its consequence for positron identification needs to be studied.

In this chapter the development of electromagnetic and hadronic showers in the calorimeter are described together with a description of the π^0 contamination. Furthermore, a detailed description of the transverse shower profile variables used in this work is presented.

3.1 Electromagnetic showers

An electromagnetic shower begins when an high-energy electron, positron or photon interacts with a material. A sketch of an electromagnetic shower is shown in figure 3.1.

The energy loss of electrons or positrons is dominated by the *bremstrahlung* process above few tens of MeV in most materials, while *ionization* processes are predominant at low energies ($\lesssim 10$ MeV) [25]. During the *bremstrahlung* process, electrons and positrons lose their energy via Coulomb interactions with the electric

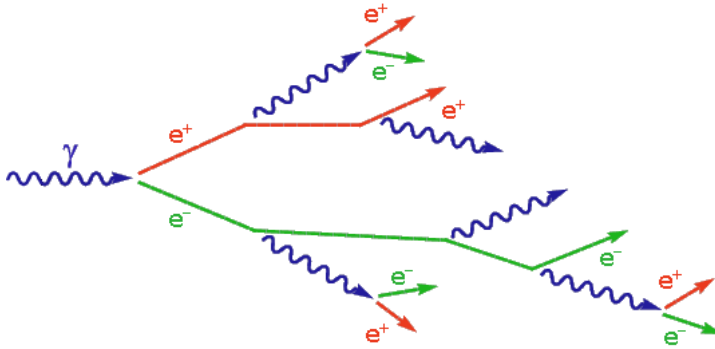


Figure 3.1. An electromagnetic shower initiated by a photon.

field generated by the atomic nuclei. The energy spectrum of the photons emitted during this interaction falls off as E^{-1} [68].

Photons instead interact with matter mainly via the *photoelectric effect*, *Compton scattering* and *electron-positron pair production*. Figure 3.2 shows the contributions of different processes to the photon total cross section as a function of energy in the case of lead [25].

The *photoelectric effect* occurs when an atom absorbs a photon and emits an electron. The photoelectric cross section varies with the photon energy as E^{-3} , so this process dominates at low energies and it loses its importance very rapidly as the energy increases.

At higher energies, between approximately a few hundred keV and around 5 MeV, *Compton scattering* is the most likely process to occur [68]. In the Compton scattering process high energy photons lose energy colliding with stationary electrons and transferring to them some of their energy and momentum. The cross section for Compton scattering is almost proportional to the atomic number Z and decreases with increasing photon energy as E^{-1} . Therefore, above a certain threshold energy, Compton scattering becomes more likely than the photoelectric effect. This threshold ranges from 20 keV for carbon ($Z = 6$) to 700 keV for uranium ($Z = 92$) [68].

When the photons have energies larger than twice the electron rest mass, i.e. 1.022 MeV, they may create, in the electric field of nuclei, *electron-positron pairs*. The cross section for pair production increases with energy and it reaches an asymptotic value for energies greater than 1 GeV; furthermore, since it is the only process where the cross section increases directly with energy, it is the most likely process to occur at high energies. Usually, the electron-positron pairs are caused by nuclear

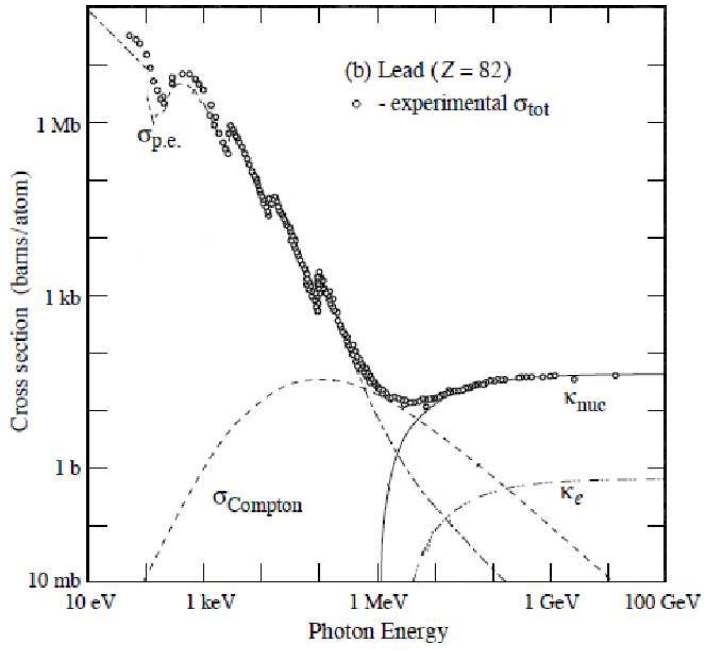


Figure 3.2. Contributions of different processes to the photon total cross section as a function of energy in lead: $\sigma_{p.e.}$ = photoelectric effect, σ_{Compton} = Compton scattering, κ_{nuc} = pair production-nuclear field, κ_e = pair production-electron field [25].

electromagnetic field; sometimes, for low- Z elements and at high energies they can also be created in the fields of the atomic electrons [68].

Since the development of electromagnetic showers is primarily determined by the electron density in the absorber medium, it is often convenient to describe the shower characteristics in a material-independent way, mainly using the *radiation length* X_0 for the longitudinal development and the *Molière radius* ρ_M for the transverse one.

The *radiation length* is defined as the distance over which an electron or positron loses 63.2 % on average of its energy due to the bremsstrahlung process [68]. The radiation length for a single material (with atomic number Z and mass number A) can be evaluated by the following expression [25]:

$$X_0 = \frac{716.4 A}{Z (Z + 1) \ln(287/\sqrt{Z})} \text{ g} \cdot \text{cm}^{-2} \quad (3.1)$$

The radiation length for a mixture of different material can be calculated as follows [68]:

$$\frac{1}{X_0} = \sum_i \frac{V_i}{X_i} \quad (3.2)$$

where V_i and X_i are respectively the fraction by volume and the radiation length (in mm) of the i^{th} component of the mixture. This formula is needed in order to evaluate for instance the effective radiation length of the PAMELA calorimeter, consisting mainly of tungsten absorbers and silicon detectors.

The *Molière radius* is defined as follows [68]:

$$\rho_M = E_s \cdot \frac{X_0}{E_c} \text{ g} \cdot \text{cm}^{-2} \quad (3.3)$$

where X_0 is the radiation length, E_c is the critical energy (see section 3.1.1) and the scale energy $E_s = m_e c^2 \sqrt{4\pi/\alpha} = 21.2$ MeV. About 90 % of the energy of an electromagnetic shower is deposited in a cylinder with radius ρ_M around the shower axis. Furthermore, the Molière radius is much less dependent on Z than the radiation length and to first approximation the Z dependence cancels. In fact, the radiation length is proportional to A/Z^2 and assuming $A \sim Z$ one obtains $X_0 \propto Z^{-1}$; considering that the critical energy is also proportional to Z^{-1} it is easy to see that ρ_M is independent of Z in first approximation [68].

3.1.1 The shower profiles

Via all the mechanisms described above, electromagnetic showers develop in the calorimeter. The average energy of the shower particles decreases until no further multiplications take place. The depth at which this occurs is called *shower maximum* and beyond this point the number of shower particles decreases. The

shower maximum is reached at a so-called *critical energy*, E_c . The critical energy is defined as the energy at which the average energy losses from radiation processes equal those from ionization. Among alternate definitions is that of Rossi [69], who defines the critical energy as the energy at which the ionization loss per radiation length X_0 is equal to the electron energy [25]:

$$\left[\frac{dE}{dX} \right]_{ion} X_0 = E \quad (3.4)$$

The critical energy is parameterised by the Particle Data Group as [25]:

$$E_c = \frac{610 \text{ MeV}}{Z + 1.24} \quad (3.5)$$

This formula is valid for solids and liquids and shows the Z^{-1} dependence.

It is important to note that the development of an electromagnetic shower, described in units of X_0 and ρ_M , becomes approximately material-independent.

The longitudinal profile

The longitudinal development is governed by the high-energy part of the cascade and therefore scales as the radiation length X_0 in the material. Figure 3.3 shows the longitudinal development of 10 GeV electron showers in different absorber materials. All the three profiles look very similar which means that they roughly scale with X_0 . However, a couple of small differences are present: as Z increases, the shower maximum shifts to greater depth and beyond it the shower profile decreases more slowly. The result of these effects is that, for instance, a larger number of radiation lengths is needed in order to contain an electromagnetic shower in lead than in aluminium [68].

Another characteristic of the longitudinal shower profile is that it has a logarithmic energy dependence. Consider, for instance, an electron that emits a photon via the bremsstrahlung process. After having traversed one radiation length, the energy of the photon produced is half of the initial electron energy E_0 . Thus, after n radiation lengths the electron has produced $N = 2^n$ secondaries (i.e. photons, electrons and positrons) each with an average energy $E = E_0/N$. As already mentioned, the cascade particles multiplication goes on until the average energy per particle drops below the critical energy E_c . The maximum development is reached after $n_{max} = \ln(E_0/E_c) / \ln 2$ radiation lengths and the maximum number of particles produced is $N_{max} = E_0/E_c$ [1].

The transverse profile

The transverse shower profile provides information about the energy deposit in a direction perpendicular to the shower axis. In the early stages of the shower development the transverse spread is caused by multiple scattering of electrons

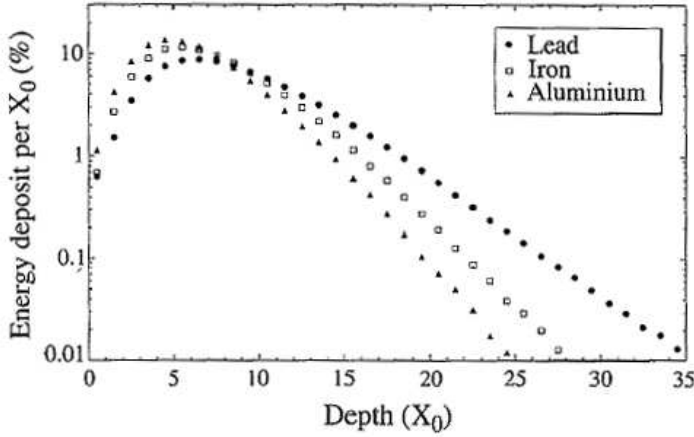


Figure 3.3. Longitudinal development of 10 GeV simulated electron showers in aluminium (black triangles), iron (open squares) and lead (black circles) [68].

and positrons, while beyond the shower maximum it is mainly due to the photons and electrons produced via Compton scattering and the photoelectric effect. Thus, radial shower profiles are characterised by a pronounced central core (the first component) surrounded by a halo (the second component). These features allow electromagnetic showers to be separated from hadronic ones. Usually transverse profiles are described in units of Molière radius ρ_M .

Electromagnetic shower development in the PAMELA calorimeter is shown in figure 3.4: the shower is initiated by a 100 GeV positron and is obtained by a GEANT3 simulation. The narrow core around the shower axis, where most of the energy is released, is clearly visible.

3.2 Hadronic showers

A hadronic interaction takes place when a hadron, e.g. a proton, enters a thick material. Strong interactions can arise between the shower particles and the nuclei of the absorbing medium resulting in a more complicated shower development compared to the electromagnetic one. Charged hadrons can ionize the atoms of the traversed medium and usually they interact strongly with the atomic nuclei. Neutral hadrons instead cannot ionize the medium: they lose energy only by nuclear interactions. An important feature which characterises hadronic shower development is that *neutrons* are abundantly produced in nuclear interactions. On the contrary, the production of neutrons is lower in electromagnetic showers: thus,

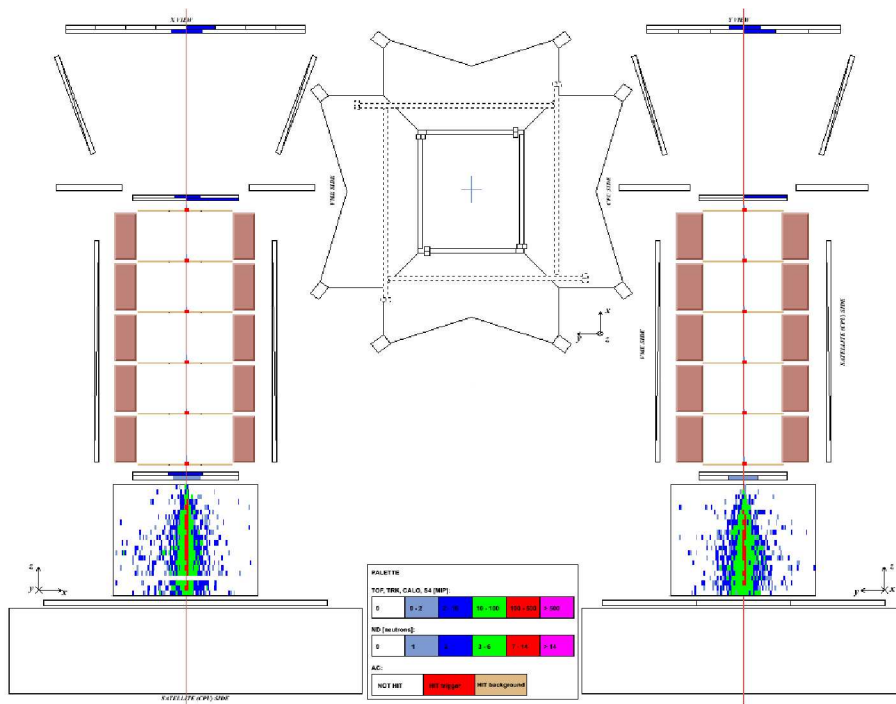


Figure 3.4. Electromagnetic shower development in the PAMELA calorimeter: the shower is initiated by a 100 GeV positron and is obtained by a GEANT3 simulation. On the left and on the right the x-view (bending) and y-view (non-bending) of the apparatus are shown respectively; a view of the event from above is depicted too. The vertical red line corresponds to the z-axis. The colour scale indicates the detected energy in each calorimeter strip.

neutron detection could be a very powerful way to distinguish between electromagnetic and hadronic showers. Another important difference is the scale of the shower development which, in the hadronic case, is governed by the cross section for nuclear interactions.

In the first nuclear reaction, mainly mesons, nucleons and photons are produced. These particles may lose their energy by ionization or interact in the calorimeter material causing shower development. This is the case of neutral pions which rapidly decay into two photons, thus initiating electromagnetic shower development inside the hadronic one (see section 3.3).

3.2.1 The shower profiles

Hadronic shower development is governed by the *nuclear interaction length* λ_{int} . The nuclear interaction length of an absorber medium is defined as the average distance a hadron has to travel inside that medium before a nuclear interaction occurs. The relationship between λ_{int} and the total cross section σ_{tot} for nuclear interactions is [68]:

$$\sigma_{tot} = \frac{A}{N_A \cdot \lambda_{int}} \quad (3.6)$$

The total cross section is determined by the interactions between incident particles and target nuclei. The total cross section scales with $A^{2/3}$. The target cross section is related to the nuclei radius as r^2 and the volume is proportional to the atomic weight A , i.e. $r^3 \propto A$. Thus, using the previous formula, one can obtain that the radiation length λ_{int} is proportional to $A^{1/3}$ when λ_{int} is expressed in units of $\text{g} \cdot \text{cm}^{-2}$ [68].

Secondary particles, mainly pions, produced in the hadronic interactions, are emitted in the forward direction of the primary hadron. The spallation fragments are emitted instead more or less isotropically in the laboratory frame. For this reason the longitudinal and the transverse profiles are very different from those of the electromagnetic showers.

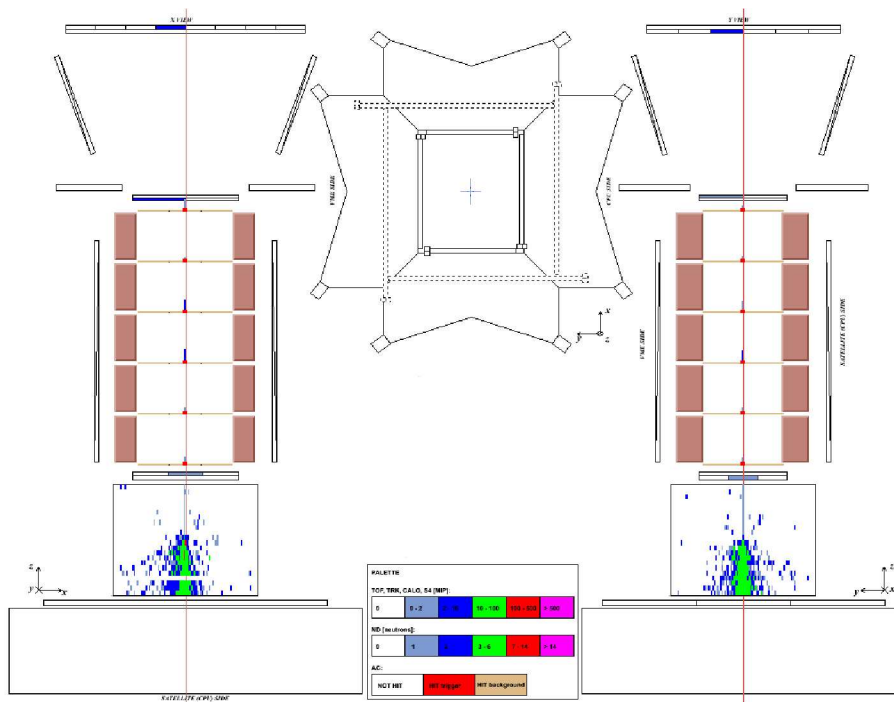
The longitudinal profile

Longitudinal profiles of hadronic showers have some similarities with those of electromagnetic showers. The number of particles produced during hadronic interactions rises roughly linearly and reaches a maximum which depends on the particle energy. Beyond the maximum, particle multiplication is balanced by the absorption of shower particles; thus, the number of secondaries decreases and this decay is much less steep than the initial rise. In this case, any maximum lies deeper in the calorimeter for a given incident energy than in the electromagnetic showers. This is due to the fact that the mean free path for hadronic interactions is much longer than for electromagnetic processes. Thus, the absorption of hadronic showers requires more material compared to the absorption of electromagnetic showers of the same energy.

The transverse profile

Hadronic showers develop deeper in the calorimeter and are also much broader than electromagnetic ones. The lateral profile is usually composed by a narrow core, generated by the electromagnetic component, and a halo produced by the non-electromagnetic shower component. The narrow core is generated by neutral pions which induce electromagnetic shower development inside the hadronic one (see section 3.3).

Hadronic shower development in the PAMELA calorimeter is shown in figure 3.5: the shower is initiated by a 100 GeV proton and is obtained by a GEANT3 simulation. Comparing this figure with an electromagnetic shower induced by a positron of the same energy (figure 3.4) it is clearly visible that a proton interacts deeper in the calorimeter and that the lateral profile of the initiated shower is broader.



3.3 The π^0 contamination of hadronic showers

As already mentioned, hadronic showers generally contain a component that propagates electromagnetically. For instance, when protons interact with nuclei in the first interaction charged and neutral pions are produced, e.g.:

$$p + N \rightarrow \pi^+, \pi^-, \pi^0 \quad (3.7)$$

While charged pions can interact with nuclei and produced other pions, neutral pions immediately decay into two photons

$$\pi^0 \rightarrow \gamma + \gamma \quad (3.8)$$

The π^0 mean lifetime is $\tau = 8.4 \cdot 10^{-17}$ s [14] with a probability of about 0.99 [25]. Thus, these photons induce an electromagnetic shower producing electrons, positrons and other photons via Compton scattering, photoelectric effect and electron-positron pair production. It is important to stress that process 3.8 is not the only way in which photons are produced in hadronic interactions. During the first proton interaction with nuclei η mesons are also produced and they can decay into two photons

$$\eta \rightarrow \gamma + \gamma \quad (3.9)$$

with a probability that is about 0.28 [25]. For low transverse momenta, the production ratio η / π^0 is of the order of 10 % [70]. In the work described in this thesis only the process 3.8 has been taken into account.

Considering process 3.7, the average fraction f_{elm} of the initial hadron energy converted into π^0 increases according to a power law:

$$f_{elm} = 1 - (1 - f_{\pi^0})^n \quad (3.10)$$

where f_{π^0} is the fraction of neutral pions produced in the first interaction, $(1 - f_{\pi^0})$ is the non-electromagnetic component of the shower and n is the number of generations of reactions. On average, approximately 1/3 of the mesons produced in the first interaction are neutral pions. It is necessary to stress that other particles are produced than just charged and neutral pions and therefore $f_{\pi^0} = 1/3$ should be considered as an upper limit [68]. Furthermore, the number of generations n is directly proportional to the energy of the particle that initiated the shower.

The transverse profiles of hadronic showers are thus characterized by an electromagnetic core caused by neutral pions. Since the electromagnetic showers develop in a smaller amount of material compared to the hadronic ones, on average the energy density is larger close to the shower axis and in the first stages of the shower development where most of the π^0 s are generated.

In the PAMELA experiment hadrons and leptons with $E > 2$ GeV cannot be discriminated by using the dE/dx and β velocity measurements provided by the time-of-flight system [60] (see section 2.1.1). Thus, the different longitudinal and

transverse shower profiles inside the electromagnetic calorimeter allow a high identification power between electromagnetic and hadronic showers. Since the identification of positrons over a large background of protons is one of the main goal of the PAMELA experiment, the electromagnetic contamination of hadronic showers due to neutral pions could affect the discrimination between positron and proton events and it becomes extremely important within the context of the positron analysis. A study of π^0 contamination of hadronic showers has been performed using simulations and it is described in chapter 4.

3.4 The PAMELA electromagnetic calorimeter

As already described in chapter 2 (section 2.1.3), the PAMELA electromagnetic calorimeter is formed by 44 single-sided silicon sensor planes interleaved with 22 plates of tungsten absorber. Each detector plane is formed by a silicon detector x-view plane, a tungsten absorber and a silicon detector y-view plane. Two detector planes formed one detector module (see figure 3.6). The silicon detectors form a total sensitive area of about $24\text{ cm} \times 24\text{ cm}$ and are arranged in a 3×3 matrix. Each silicon detector is segmented into 32 read-out strips thus forming 96 total strips for each plane. Furthermore, all the strips are connected creating 24 cm long strips [59].

The calorimeter was designed in order to contain electromagnetic showers: its total depth is $16.3 X_0$ and up to energies of the order of 1 TeV the maximum of the electromagnetic cascade is well contained inside the calorimeter [64]. On the contrary, the total depth corresponds to ~ 0.6 nuclear interaction lengths only, thus $\sim 40\%$ of protons pass through the calorimeter without interacting. The longitudinal and transverse segmentation of the calorimeter combined with the energy released in each silicon strip gives a powerful way to identify electromagnetic showers [59].

The calorimeter reconstructs the energy of incident electrons independently from the tracking system. Figure 3.7 shows the energy dependence of the energy resolution of the calorimeter: the energy resolution for electrons shows a square root dependence on the energy reaching a constant value above 20 GeV of $\sim 5.5\%$. Up to 200 GeV it follows a quasi-linear behaviour as a function of the electron energy with deviations accounting for the partial containment at the highest energy. For energies greater than ~ 800 GeV the resolution decreases because of increasing longitudinal leakage and saturation of the signal from the strips (~ 1100 MIP) [64]. One MIP is the energy deposited by a minimum ionising particle. The mean rate of energy loss by relativistic particles traversing a material is governed by the Bethe-Bloch equation: the trend of this equation as a function of the particle momentum has a minimum due to ionisation processes which lies around $1 - 2\text{ MeV cm}^2\text{ g}^{-1}$ [25].

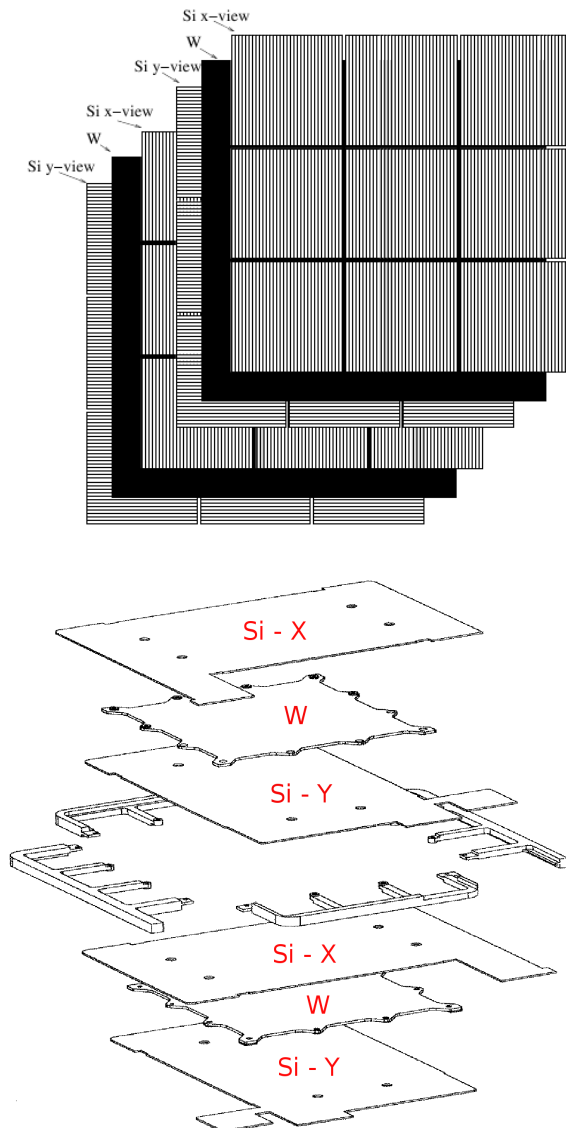


Figure 3.6. Schematic overview of one calorimeter module. One module consists of two detector planes, where each plane is formed by a silicon detector x-view plane, a tungsten absorber and a silicon detector y-view plane; the segmentation of each silicon detector plane in 96 total strips is also visible (*top*). The calorimeter consists of 11 of such modules [71].

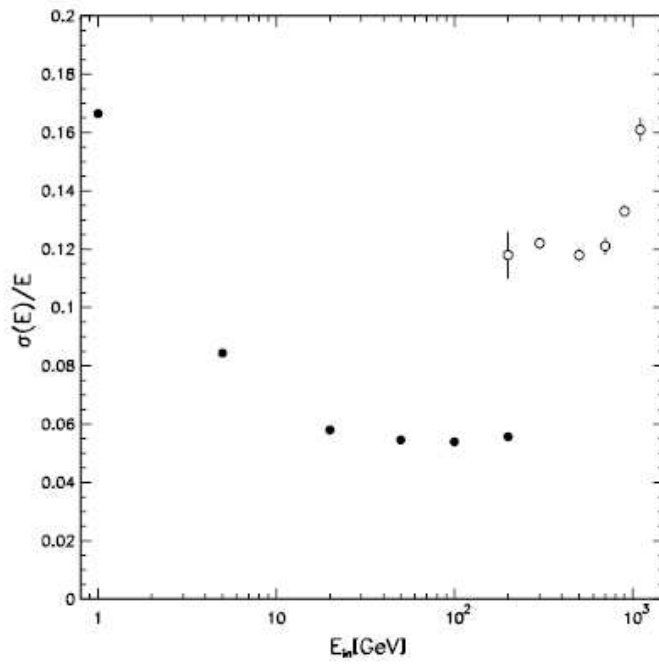


Figure 3.7. The energy dependence of the energy resolution of the electromagnetic calorimeter. The black filled points are for normal operation (test beam data) and the open circle points are for the self-trigger mode (simulations) described in section 2.2.1 [59].

3.4.1 Shower profile variables

In order to study the π^0 contamination of hadronic showers in the PAMELA calorimeter, shower profiles have been studied in a detailed way using GEANT3 simulations (see chapter 4). The variables used to distinguish between electromagnetic and hadronic interactions are described below, where the term *strips* refers to the silicon strips which constitute each detector plane (see figure 3.6), and the terms *track* and *rigidity* refer respectively to the track and the rigidity as reconstructed by the tracker. In the PAMELA calorimeter a radius of $2\rho_M$ around the shower axis corresponds to 8.5 silicon strips [64]. Furthermore, the shower axis is defined by extrapolating the particle track reconstructed by the spectrometer. The variables are divided into variables related to the energy released in the calorimeter and variables related to the number of hit strips. Figures 3.8 – 3.12 show the distributions of some of the quantities listed below for simulated 100 GeV positrons and protons.

Energy related variables

- ***qtot*** → *total energy deposited in the calorimeter*
since up to energies of the order of 1 TeV the maxima of the electromagnetic cascades are well contained inside the PAMELA calorimeter [64] and $\sim 40\%$ of the hadronic particles pass through the calorimeter without interacting, *qtot* is expected to be greater for electromagnetic than for hadronic events for a given incident energy (see figure 3.8);
- ***qtrack*** → *energy deposited in the strips along the track and in the neighbouring strips on each side*
as described in section 3.1, since about 90 % of the energy of an electromagnetic shower is deposited in a cylinder of radius ρ_M around the shower axis, *qtrack* has higher values in the electromagnetic case than in the hadronic one;
- ***qstrack*** → *energy deposited in the hit strips along the reconstructed track*
in electromagnetic showers *qstrack* is greater than in hadronic cascades (see also *qtrack*);
- ***qmax*** → *the maximum energy deposited in a single strip*
the released energy in each strip reflects the secondary particle multiplicity density; thus, for electromagnetic showers, characterised by a larger number of secondaries, this value is expected to be larger compared to hadronic showers;
- ***qcyl*** → *energy deposited in a cylinder of radius eight strips around the shower axis*
since eight silicon strips in the PAMELA calorimeter correspond to $\sim 2\rho_M$ [64], more than 90 % of the energy of an electromagnetic shower is released in a cylinder of radius eight strips around the shower axis; thus, *qcyl* is greater in the electromagnetic case than in the hadronic one;

- ***qpre*** → energy deposited in a cylinder of radius eight strips around the shower axis, and only in the first three calorimeter planes
since the mean free path for electromagnetic interactions is shorter than for hadronic interactions, the probability that an electromagnetic shower starts in the first three planes of the calorimeter is greater than for hadronic showers ($\sim 89\%$ [64]); thus, *qpre* is greater in the electromagnetic case (see also *qcyl*);
- ***qtr*** → energy deposited in a cylinder of radius four strips around the shower axis
due to the topology of the transverse shower profile, this variable is greater for electromagnetic cascades than for hadronic ones (see also *qcyl*);
- ***qpresh*** → energy deposited in a cylinder of radius two strips around the shower axis and only in the first four planes of the calorimeter
due to differences in shower topology, *qpresh* assumes higher values in the electromagnetic case than in the hadronic one; the *qpresh* distribution (see figure 3.10-top) shows that showers induced by positrons start mostly in the first calorimeter planes while protons with the same initial energy interact deeper (see also *qcyl* and *qpre*);
- ***qcore*** → sum of the convolution of the energy q_{hit} released on each calorimeter plane within a cylinder of radius $2\rho_M$ around the shower axis and the number of the plane itself; the sum is performed on both views and only up to the plane pl_{max} closest to the electromagnetic shower maximum

$$qcore = \sum_{i=1}^{pl_{max}} \sum_{j=Xview}^{Yview} q_{hit}(i,j) \cdot i$$

since the transverse shower profile for electromagnetic cascades is smaller than for hadronic ones, *qcore* has greater values for electromagnetic events (see also *ncore*);

- ***e0imp*** → ratio between the energy released in the calorimeter and the rigidity reconstructed by the tracker; the energy released in the calorimeter is extrapolated from the fit of the longitudinal shower development
this variable is almost constant for positron and electron events because electromagnetic showers are more confined than hadronic ones, thus the energy in the calorimeter is proportional to the initial energy of the particle, i.e. the energy reconstructed by the tracker; this is not the case in hadronic interactions where part of the energy is not detected in the calorimeter due to emission of neutrinos, neutrons, etc.
- ***v4sig*** → energy released in the strip hit by the track and in the one to the right and to the left, and only in the first two calorimeter planes
due to the shower topology, this variable is greater for electromagnetic cascades than for hadronic ones (see also *qcyl*, *qpre* and *qpresh*);

- ***enfitatmax*** → difference between discrete and continuous values of the energy released in the planes around the maximum longitudinal development of the shower
due to the shower topology, this variable assumes greater values for electromagnetic showers than for hadronic ones;
- ***enfitatmaxns*** = *enfitatmax* / *nstrip*
- ***asymmetry*** → ratio between the energy released in the calorimeter planes above and up to the plane where the energy released is maximum, $plane_{max}$, and the energy released below $plane_{max}$
this variable represents the asymmetry of the longitudinal shower profile, thus it is almost constant for electromagnetic showers while assumes different values for hadronic cascades;
- ***aveder*** → average derivative of the longitudinal shower profile fit done on the first seven calorimeter planes
due to the shower topology this variable assumes higher values for electromagnetic showers than for hadronic ones;
- ***qtotimp*** = *qtot* / *rigidity*
the *qtotimp* distribution (see figure 3.9-*top*) is essentially flat for protons with a peak at low energies for the non-interacting ones; in the positron case, the energy is normally distributed as long as most of the shower is contained inside the calorimeter [64]; its behaviour is similar to the distribution of *qtot*, i.e. the total energy detected in the calorimeter;
- ***qm*** = *qmax* / *qtrack*
this variable (see figure 3.12-*bottom*) is sensitive to the transverse shower profiles: in the shower induced by positrons the maximum energy is released along the event track and thus the *qm* distribution shows a narrow peak close to zero; *qm* assumes higher values in the proton case, since hadronic interactions or nuclei fragmentations can take place far away from the shower axis;
- ***q0*** = *qstrack* / *qtot*
it is the fraction of the calorimeter energy deposited on the hit strips along the reconstructed track and it assumes greater values for electromagnetic showers (see also *q3*)
- ***q1*** = *qcyl* / *qtot*
this variable (see figure 3.11-*bottom*) is the fraction of calorimeter energy deposited inside a cylinder of radius eight strips ($\sim 2\rho_M$) around the shower axis; thus, in the electromagnetic showers $q1 \sim 0.9$, i.e. 90 % of the energy released in the calorimeter is detected within eight strips from the shower axis;

- $q2 = q_{track} / q_{tr}$
this variable (see figure 3.11-*top*) is the ratio between the energy deposited in the strip closest to the track and that deposited inside a cylinder of radius four strips around the shower axis; showers initiated by positrons have $q2 \sim 0.6 - 0.7$ (see also *qt1*);
- $q3 = q_{track} / q_{tot}$
this variable is similar to $q1$ but in this case it is the fraction of calorimeter energy deposited in the strips closest to the event track; showers initiated by positrons have $q3 \sim 0.5 - 0.6$ (see figure 3.10-*bottom*);
- $q4 = q_{tr} / q_{tot}$
this variable is very similar to $q1$ and $q3$; in this case, it is the fraction of calorimeter energy deposited inside a cylinder of radius four strips around the shower axis; showers initiated by simulated positrons have $q4 \sim 0.8$;
- $qt1 = q_{track} / q_{cyl}$
a simple calculation shows that $qt1 = q_{track} / q_{cyl} = q3 / q1$ and its distribution in the positrons case has a sharp peak around 0.6: this means that $\sim 60\%$ of the energy detected within eight strips from the shower axis is deposited in the strips closest to the track (see figure 3.12-*top*).

Strip number related variables

- $nstrip \rightarrow$ total number of strips hit in the calorimeter
since electromagnetic and hadronic events have a very different shower topology, the distribution of $nstrip$ is very different in the two cases; generally, for a given incident energy, due to the different interaction types and to the calorimeter sizes, it assumes higher values in the electromagnetic case than in the hadronic one;
- $ncyl \rightarrow$ number of strips hit in a cylinder of radius eight strips around the shower axis
eight silicon strips in the PAMELA calorimeter correspond to $\sim 2\rho_M$ [64], thus this variable has much higher values for electromagnetic showers than for hadronic ones (see also $nstrip$);
- $npre \rightarrow$ number of strips hit in a cylinder of radius eight strips around the shower axis in the first three calorimeter planes
the probability that an electromagnetic shower starts in the first three planes of the calorimeter is greater than 89% [64], thus $npre$ is greater in the electromagnetic case than in hadronic one (see also $nstrip$ and $ncyl$);
- $v3sihit \rightarrow$ number of strips hit in the first three calorimeter planes
this variable has greater values in the electromagnetic case (see also $npre$);

- n_{core} → sum of the convolution of the number of hit strips n_{hit} on each calorimeter plane within a cylinder of radius $2\rho_M$ around the shower axis and the number of the plane itself; the sum is performed on both views and only up to the plane pl_{max} closest to the electromagnetic shower maximum

$$n_{core} = \sum_{i=1}^{pl_{max}} \sum_{j=X_{view}}^{Y_{view}} n_{hit}(i, j) \cdot i$$

since the transverse shower profile for electromagnetic cascades is smaller than for hadronic ones, n_{core} has greater values for electromagnetic events (see figure 3.9-bottom).

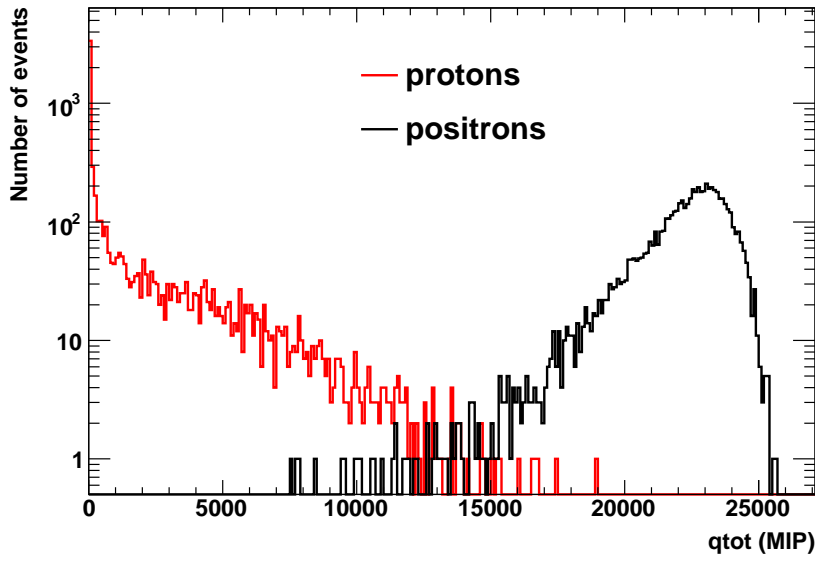


Figure 3.8. Distribution of the total energy $qtot$ detected in the calorimeter for 100 GeV simulated positrons (black line) and protons (red line). 1 MIP is the average energy deposited by a minimum ionising particle.

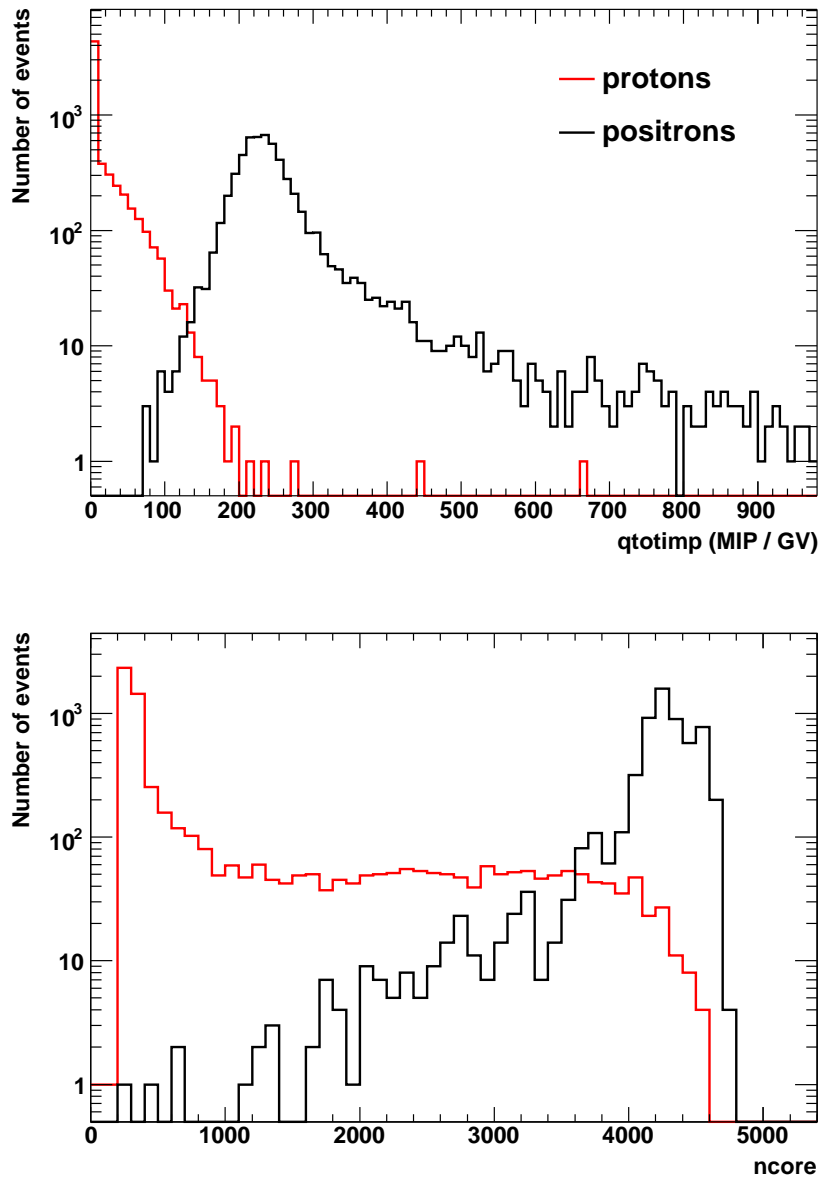


Figure 3.9. Distributions of some shower profile variables for 100 GeV simulated positrons (black line) and protons (red line). *Top*: distribution of the variable $qtotimp = qtot / rigidity$. *Bottom*: distribution of $ncore$ as defined in the text. 1 MIP is the average energy deposited by a minimum ionising particle.

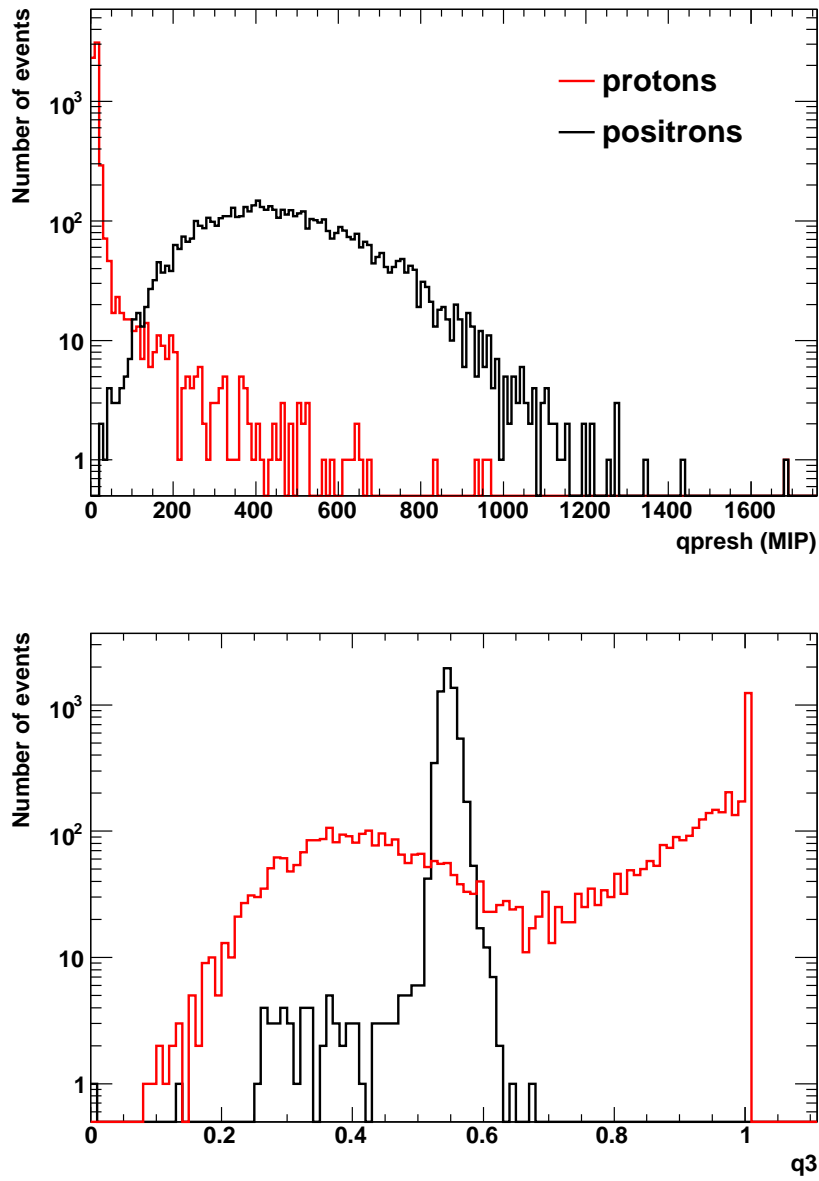


Figure 3.10. Distributions of some shower profile variables for 100 GeV simulated positrons (black line) and protons (red line). *Top:* distribution of q_{presh} as defined in the text. *Bottom:* distribution of $q_3 = q_{track} / q_{tot}$. 1 MIP is the average energy deposited by a minimum ionising particle.

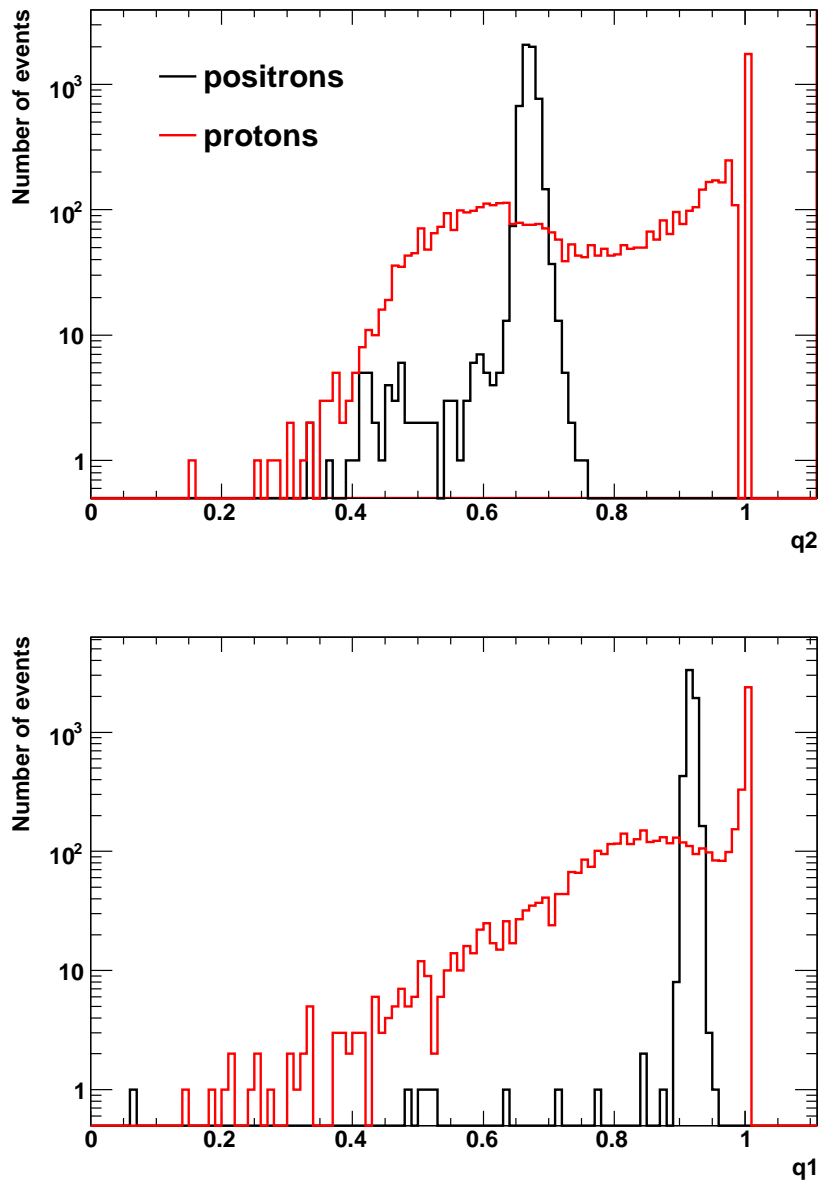


Figure 3.11. Distributions of some shower profile variables for 100 GeV simulated positrons (black line) and protons (red line). *Top:* distribution of $q2 = q_{track} / q_{tr}$. *Bottom:* distribution of $q1 = q_{cyl} / q_{tot}$. 1 MIP is the average energy deposited by a minimum ionising particle.

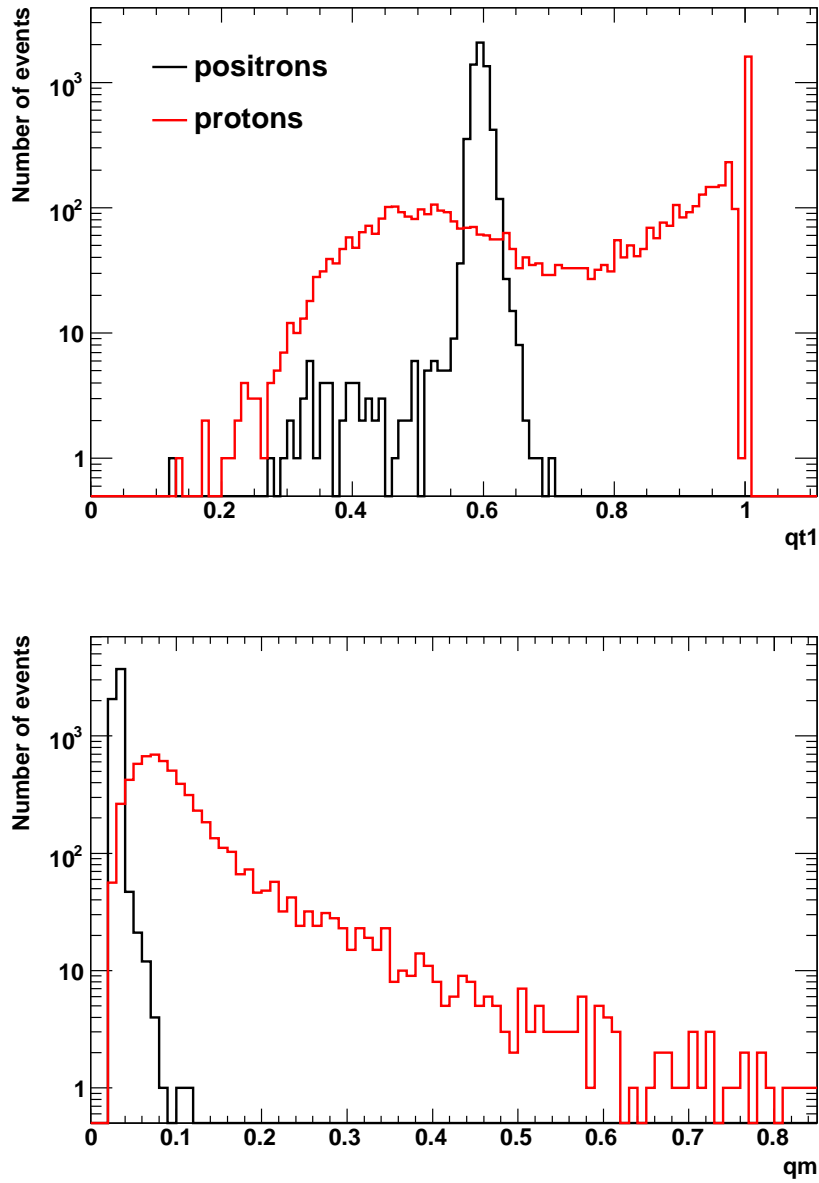


Figure 3.12. Distributions of some shower profile variables for 100 GeV simulated positrons (black line) and protons (red line). *Top:* distribution of $qt1 = q_{track} / q_{cyl}$. *Bottom:* distribution of $qm = q_{max} / q_{track}$. 1 MIP is the average energy deposited by a minimum ionising particle.

Chapter 4

Simulation studies of π^0 contamination

Among all the secondary particles produced in a hadronic interaction (see section 3.2), neutral pions are of particular interest because they almost immediately decay into two photons (see section 3.3). These photons initiate electromagnetic showers which develop inside the hadronic cascades and which may result in a proton being misidentified as a positron.

In order to study this electromagnetic component in hadronic showers, simulations of hadronic and electromagnetic showers induced by protons and positrons respectively have been produced and studied. The simulation of the entire apparatus is a Monte Carlo program based on the GEANT code, version 3.21, and was developed by the PAMELA Collaboration. The simulation code was also modified in order to artificially increase the number of neutral pions produced in hadronic showers and study the consequences for positron identification.

In this chapter part of the simulation code and the related changes used in this analysis are described. An approach using shower profile variables in the calorimeter has been tested on simulations in two different energy ranges and up to a maximum energy of 300 GeV. This approach has been also applied to flight data in order to select positron and electron events. The resulting positron fraction is shown at the end of the chapter.

4.1 GEANT3 simulations

As described in section 3.3, hadronic showers contain an electromagnetic component initiated by the neutral pions. In order to study this π^0 contamination in hadronic showers simulations of protons and positrons interacting in the calorimeter have been produced and studied.

The simulations have been performed using GPAMELA [72], the PAMELA Collaboration's official simulation code. GPAMELA is a Monte Carlo program based on the GEANT package [73] version 3.21. The simulation code reproduces in detail PAMELA subdetectors, including all the mechanical parts inside the experiment acceptance and the pressurized vessel which contains the apparatus.

The GPAMELA code consists of three main parts; each part calls different subroutines which were implemented for different tasks. These three main parts are:

1. *initialization* \rightarrow this is the initial phase where all the data structures and parameters are initialized and prepared for the event simulation. This phase is controlled by the user in the subroutine UGINIT. Each step is controlled both by default GEANT subroutines and GPAMELA user subroutines which are identified by the prefix GP:
 - the input datacards, chosen by the user in the subroutine GPFFR, are interpreted;
 - the subroutine GSPART creates the data structure JPART which describes the particle properties;
 - the subroutine GPMAT creates the data structure JMATE which describes the characteristics of the materials used;
 - the geometrical volumes which constitute the detector are defined in the subroutines GPGE0 and GPDAT and stored in the JVOLUM data structures;
 - the tracking medium parameters are defined in the subroutine GPMED;
 - the sensitive elements of the geometrical volumes are defined in the subroutine GPHIT;
 - all the geometrical information defined by the user are processed in the subroutine GGCLOS;
 - the energy loss and cross section tables are calculated and stored in the data structure JMATE by the subroutine GPHYSI.

At the end of this phase everything is ready for the particle transportation;

2. *event processing* \rightarrow this is the main phase where primary particles are followed inside the detector, from the generation point to the final step; it is controlled by the subroutine GRUN. Each step of the generated events is analysed by different subroutines. Here a list of the most important ones:

GUKINE reads or generates the kinematics of the primary particle track (i.e. particle arrival direction (θ, ϕ) , energy, etc.) and stores it in specific data structures;

GUTREV controls the propagation of each particle by calling the subroutine GUTRACK;

GUTRACK controls the tracking of one event; if a particle passes through a sensitive detector, all useful information “hits” are stored in the data structure JHITS;

GUSTEP controls each tracking step along the track. This subroutine can store a hit or transfers a secondary product; also, coordinates of points along the track are stored;

GUPHAD calls the hadronic package for cross section calculation, in case of hadronic interaction; the hadronic package is selected by the user;

GUDIGI controls the response of different detectors using information stored during the particle transportation in the data structures JHITS; the results are then stored in a specific data structure;

GUOUT is called at the end of one event and performs the final processes, such as output the relevant data structures.

3. *termination* → this is the last phase, where final results are printed and histograms are saved; it is controlled by the subroutine UGLAST.

The default configuration of geometric volumes defined in GPAMELA is shown in figure 4.1. The geometric volumes included in this configuration are: the time-of-flight system (S1, S2 and S3), the magnetic spectrometer, the electromagnetic calorimeter, the anticoincidence system (CAS, CAT and CARD), the neutron detector and the bottom scintillator plane S4. The pressurized vessel which encloses the whole apparatus is also included. With respect to the PAMELA reference system (figure 2.2) the GPAMELA reference system is shifted 49.229 cm down along the z-axis; thus, in the GPAMELA reference system, the origin of the PAMELA reference system has coordinates $(x_0, y_0, z_0) = (0, 0, 49.229)$ [74]. Also, all the simulated events presented in this work have been generated on a surface with dimensions $2 \text{ m} \times 2 \text{ m}$ positioned at $z = 1.095 \text{ m}$ (see figure 4.1).

Proton events have been simulated using the FLUKA hadronic generator package¹. In FLUKA different models of hadronic processes are used depending on the type and on the energy of the primary particle. The total cross section for hadronic interactions is evaluated during the *event processing* phase since it depends on the nature of the incident particle. Thus the cross section is evaluated during the particle tracking process by FLUKA subroutines [73]. A study of the PAMELA calorimeter performance using the FLUKA hadronic package is reported in [64].

¹version 2006.3b-7.

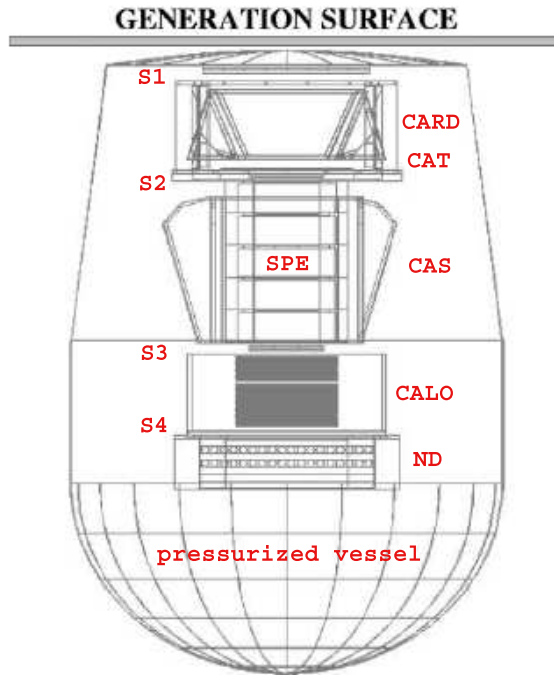


Figure 4.1. Configuration of the PAMELA apparatus as simulated by the GPAMELA code [74]. This configuration includes: the time-of-flight system (consisting of the scintillator planes S1, S2 and S3), the magnetic spectrometer (SPE), the electromagnetic calorimeter (CALO), the anticoincidence system (CAS, CAT and CARD), the neutron detector (ND) and the bottom scintillator plane S4. The pressurized vessel which contains the whole apparatus is also included. The generation surface is shown on the top: it has dimensions $2\text{ m} \times 2\text{ m}$ and it is positioned at $z = 1.095\text{ m}$.

4.2 “Only- π^0 case” simulations

As described in section 3.3, hadronic showers contain an electromagnetic component which could have consequences for positron identification. Thus, a primary goal of this work was to quantify the electromagnetic contamination of hadronic showers using GEANT3 simulations (see section 4.1).

The number of π^0 s produced in hadronic showers has been increased and the characteristics of the corresponding shower profiles studied. An artificial way of increasing the number of π^0 s is to change all the charged pions produced in a hadronic shower into neutral ones, assuming similar production characteristics for charged and neutral pions, like for instance angular distribution and cross section. Of course, this is a non-physical process but it allows the π^0 contamination to be studied in a straight-forward way, without modifying the interaction cross section of the primary proton in the GEANT3 simulation package. As mentioned in section 4.1 the cross section is evaluated by FLUKA subroutines during the particle tracking process since it depends on the nature of the particle and on the interaction type. Thus changing the cross section of the primary proton implies changes in the cross section calculations of all the other secondary interaction processes, and this requires a deep modification in the GEANT3 simulation code.

Charged pions were converted into neutral ones in the GUSTEP subroutine of the GPAMELA code where the secondary particles are processed (section 4.1). In this subroutine secondary particles are transferred either to the JSTAK stack or to the JVERTX and JKINE event structures by calling the GSKING subroutine. In the JSTAK data structure secondary particles generated by the current transported particle are processed before proceeding to the next particle [74]. The changes were written at the end of the GUSTEP subroutine, just before the call to the GSKING subroutine. Furthermore, this change was made for all the π^+ and π^- produced in hadronic interactions in all the PAMELA apparatus, but in the subsequent analysis only events interacting in the calorimeter have been considered (see selections described in section 4.4).

Note that, from now on, proton simulations produced with this change will be referred to as the **only- π^0** case while usual proton simulations will be mentioned as the *normal case*.

4.3 Simulation analysis

In order to study the electromagnetic contamination of hadronic showers, simulations of positron and proton events have been produced and studied. Standard selection criteria for positron identification (see section 4.4) have been applied to:

- the simulated positron sample, in order to find the selection efficiencies
- the simulated proton sample (*normal case*), in order to study the contamination

- the simulated proton sample (*only- π^0 case*), in order to study the contamination

Two sets of simulations have been produced in different energy ranges:

- 20 – 100 GeV
- 100 – 300 GeV

All the incident particles have been randomly generated with an inclination angle $\theta = (0, 20)^\circ$ (the maximum track inclination allowed by the PAMELA geometrical factor is 20° [63]) and an azimuth angle $\phi = (0, 359)^\circ$. The events have been generated with an energy spectrum $\propto E^{-2.7}$ for protons and $\propto E^{-3.0}$ for positrons, in agreement with cosmic ray measurements of proton and electron spectra (see section 1.1).

The simulations produced in this work are summarized in table 4.1. Hadronic shower development in the *only- π^0 case* are also shown in figure 4.2: the events belong to simulations produced in the energy range 20 – 100 GeV. The shower development in the calorimeter looks very different in the two cases: the event depicted in figure 4.2-*top* is similar to a hadronic cascade without any pion modifications (see figure 3.5); the event shower development shown in figure 4.2-*bottom* has instead a very pronounced core and is more similar to an electromagnetic cascade (see figure 3.4). This last case could be problematic and may result in a proton being misidentified as a positron.

E = (20 – 100) GeV	E = (100 – 300) GeV
10^5 positrons	$6 \cdot 10^4$ positrons
10^5 protons (<i>normal case</i>)	10^5 protons (<i>normal case</i>)
$5 \cdot 10^5$ protons (<i>only-π^0 case</i>)	$5 \cdot 10^5$ protons (<i>only-π^0 case</i>)

Table 4.1. Number of simulated positrons and protons (*normal* and *only- π^0 case*) produced in two different energy ranges and used in the analysis described in following sections.

In the following section, the analysis of the simulations listed in table 4.1 is described.

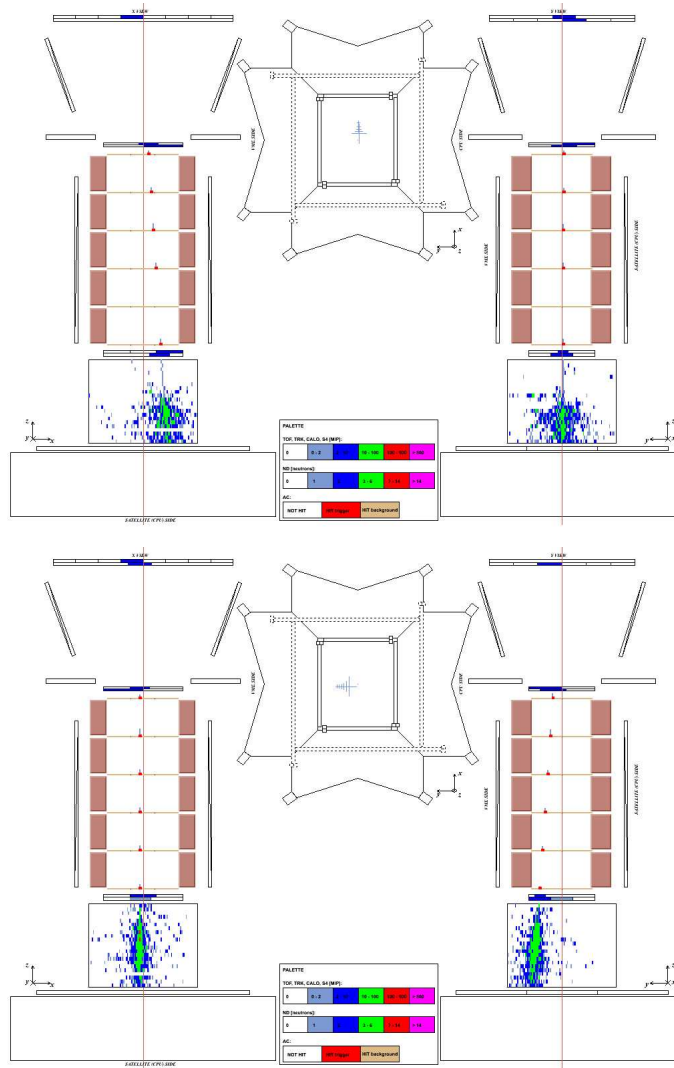


Figure 4.2. Two different examples of hadronic shower development in the PAMELA calorimeter in the *only- π^0* case simulations. The events have been randomly generated with an inclination angle $\theta = (0, 20)^\circ$ and an azimuth angle $\phi = (0, 359)^\circ$, also according to an energy spectrum $\propto E^{-2.7}$. The vertical red line corresponds to the z-axis. *Top*: event with a tracker reconstructed rigidity of 47.6 GV; the shower development is similar to a hadronic one generated in the normal case (see figure 3.5). *Bottom*: event with a tracker reconstructed rigidity of 41.6 GV; in this case the shower development has a very pronounced core and is more similar to an electromagnetic shower development (see figure 3.4).

4.4 Positron selection criteria

The standard positron selection criteria, used for both simulated and flight data, can be summarized as:

- tracker selections
- time-of-flight selections
- anticoincidence selections
- calorimeter selections

The requirements applied to each subdetector are described in the following sections.

4.4.1 Tracker selections

As described in section 2.1.2, the magnetic spectrometer allows charged particle deflection, η , to be measured as well as the rigidity. Furthermore, particle tracks are reconstructed using spatial information from the energy released in the six silicon layers. The following criteria are used in order to select events with a good reconstructed track:

1. $\chi^2 > 0$
2. number of integration steps in the track fitting algorithm < 100
3. $\chi^2 < 6.8014 + 138.876 \cdot \eta^2 - 9.69343 \cdot \eta^4$
4. $\chi_x^2 < 3.58161 + 88.334 \cdot \eta^2 - 7.64979 \cdot \eta^4$
5. number of hits in the x-view ≥ 4
6. number of hits in the y-view ≥ 3
7. rigidity $< \text{MDR}$
8. dE/dx averaged over all the planes $< 2 \text{ MIP}$

The first and the second criteria put constraints on the quality of the fitted track and select events with a single track reconstructed by the tracker. The third and fourth selections set an upper limit respectively on the evaluated global χ^2 and on the χ^2 evaluated on the x -view, rejecting particles scattered on the tracker planes or events with multiple tracks. The fifth and the sixth criteria ensure a good quality of the track. Furthermore, the track fitting procedure determines the particle deflection η ; the error associated to the measured deflection η is used as an estimate of the MDR for each event (see section 2.1.2). Thus, the seventh selection requires that the reconstructed rigidity for each event should be smaller than the estimated MDR, eliminating all the events with a large error on the measured

deflection η . The last criterion selects events which do not release an energy greater than 2 MIP in all the silicon layers (1 MIP is the average energy deposited by a minimum ionising particle); thus, particles which pass through the tracker without interacting are selected [38].

4.4.2 Time-of-flight selections

The time-of-flight system (see section 2.1.1) provides the main PAMELA trigger, where coincidental energy deposits are required in the three scintillator planes. The absolute value of charge, z , of the incident particles is also determined by measuring the ionisation energy loss (dE/dx) in the scintillators. Furthermore, the ToF system measures the time-of-flight of the particles passing through its planes. Thus, the velocity β of incident particles is derived combining this information with the track length obtained from the spectrometer. The selection criteria regarding the time-of-flight system are the following:

1. no more than one hit paddle in the scintillator layers S11, S12, S21 and S22
2. released energy in S1 less than 3 MIP
3. released energy in S2 less than 3 MIP
4. the sum of the energy released in S1 and S2 must be higher than 0.2 MIP
5. $\beta > 0$

The first four conditions select non-interacting particles in the silicon layers above the tracker and also reject multiparticle events. No constraints are put on the scintillator layer S3 because events interacting in the calorimeter can produce secondary particles which are backscattered towards S3. Furthermore, albedo particles crossing PAMELA from bottom to top are rejected by requiring a positive velocity β (fifth selection) [38].

4.4.3 Anticoincidence selections

As already mentioned in section 2.1.5, the anticoincidence system permits identification of secondary particles produced via interactions of the primary ones with the PAMELA apparatus. In order to remove these *false trigger events*, the following events are selected:

1. events without signals in CARD scintillators
2. events without signals in CAT scintillator

Events which produce signals in the CAS scintillators are instead not rejected since particles backscattered from the calorimeter can hit the anticoincidence scintillators surrounding the tracker [38].

4.4.4 Calorimeter selections

The main task of the electromagnetic calorimeter is the identification of electromagnetic and hadronic showers through its longitudinal and transverse segmentation (see section 2.1.3).

Since a radius of $2 \rho_M$ around the shower axis corresponds to 8.5 silicon strips [64] only events that shower $\sim 8 - 9$ strips away from the calorimeter borders are selected thus ensuring that $\sim 95 \%$ of the shower energy is contained inside the calorimeter. Selections regarding the shower development are also considered:

1. $tmaximp = tmax / \log(qtot) < 1.5$
2. $noint < 5 \cdot (1 + 5 \cdot e^{-0.1 \cdot R})$

where $qtot$ is the total energy detected in the calorimeter (see section 3.4.1).

The first selection is related to the shower longitudinal development: for each event, the shower longitudinal development in the calorimeter is fitted with a gamma function [75] and the maximum, $tmax$, of the fit is evaluated in units of radiation length X_0 . Simulations in the energy range 20 – 100 GeV show that $tmaximp < 1.5 X_0/\text{MIP}$ selects 97.8 % of positrons and 44.0 % of protons (see figure 4.3). This is because hadronic showers develop deeper in the calorimeter than electromagnetic showers.

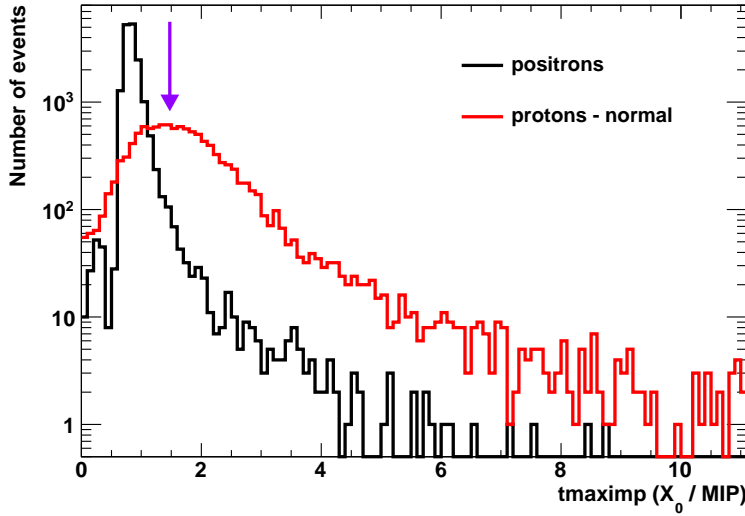


Figure 4.3. Distribution of the variable $tmaximp$ for simulated positrons (black line) and protons in the *normal case* (red line). The violet arrow shows the cut $tmaximp < 1.5 X_0/\text{MIP}$ which selects 97.8 % of positrons and 44.0 % of protons. The distributions are obtained from simulated events in the energy range 20 – 100 GeV.

The second selection is related to the starting point of the shower. The variable *noint* is defined as follows:

$$noint = \sum_{j=1}^2 \sum_{i=1}^{22} \theta(i, j) \cdot i \quad (4.1)$$

where $\theta(i, j) = 1$ if the deposited energy is typical of a proton (~ 1 MIP) within 4 mm from the reconstructed shower axis, otherwise $\theta(i, j) = 0$. The final value is evaluated summing over all the 22 calorimeter tungsten planes and for both the *x-view* and *y-view*. The *noint* value increases as the interactions start deeper in the calorimeter: thus, it assumes low values for electromagnetic showers which have a high probability to start in the first three calorimeter planes.

4.5 The “Nature analysis” approach

As described in Chapter 3, showers induced by hadronic events differ significantly from those induced by electromagnetic ones. In the hadronic case the lateral profile is broader than in electromagnetic showers which also have a pronounced central core surrounded by a more diffuse halo.

Information about the energy deposit in a direction perpendicular to the shower axis is provided by the variable $qtrack/qtot$, where $qtrack$ is the energy deposited in the strips along the track and in the neighbouring strips on each side and $qtot$ is the total energy detected in the calorimeter (see section 3.4.1 for a further description). This variable describes the fraction of calorimeter energy deposited in the strips closest to the shower axis as reconstructed by the tracker.

The selections described in section 4.4 have been used to produce the widely discussed² positron fraction published in the journal Nature [31] (see section 1.5.1). The selection approach primarily uses the longitudinal development and the starting point of the shower in the calorimeter in order to separate electromagnetic and hadronic events; furthermore, evaluating these variables in the upper and in the lower part of the calorimeter, a clean sample of protons and positrons was obtained. The procedure is the following: the 22 tungsten planes which constitute the calorimeter have been divided in two parts: the upper part from plane 1 to plane 20, and the lower part from plane 3 to plane 22. All the variables related to the calorimeter, i.e. the total detected energy and the shower profile variables, have been evaluated separately for both parts. Among positively charged events a clean sample of protons can be obtained selecting particles that do not interact in the first two planes, i.e. considering only the lower part of the calorimeter, since only 2 % of positrons with rigidities greater than 1.5 GV pass this condition [31]. For positron identification only the upper part of the calorimeter has been used. The number of electron and positron candidates in each energy interval was evaluated by a parametric bootstrap analysis [76] (see also section 5.4) with maximum

²There have been 858 citations to date, 12 - 4 - 2012, according to SPIRES.

likelihood fitting applied to the calorimeter energy fraction distributions along the track ($qtrack/qtot$) [31].

Schubnell [77] argues that the rise in PAMELA positron fraction for energies greater than 10 GeV could be due to π^0 contamination of hadronic showers. In order to investigate this, the selections used in the Nature approach were applied to proton (*normal* and *only- π^0 case*) and positron simulated samples. The $qtrack/qtot$ distributions for the selected events are shown in the upper panels of figures 4.4, 4.5 and 4.6 and are plotted in three different rigidity ranges. Simulations show that distributions for protons in the *only- π^0 case* are well separated from those of positrons. The distributions related to simulated positrons and protons in the *only- π^0 case* have then been compared to the $qtrack/qtot$ distributions for positively charged particles in flight data selecting through the Nature approach (figures 4.4-*bottom*, 4.5-*bottom* and 4.6-*bottom*). In this procedure it has been assumed that all the positive particles in flight data are protons (the proton-to-positron flux ratio is $\sim 10^4$ at 100 GV). The $qtrack/qtot$ distribution for positively charged particles in flight data (red line) appears as a mixture of two components: one for $qtrack/qtot < 0.5$ and one which lies around $qtrack/qtot \sim 0.5 - 0.6$. This means that the $qtrack/qtot$ distribution for positively charged particles in flight data can not be explained considering only the $qtrack/qtot$ distribution for simulated protons in the *only- π^0 case*. Thus, in order to fully describe it a considerable component of positrons must be introduced. The $qtrack/qtot$ distribution for simulated positrons well reproduces the distribution for positive flight data with $qtrack/qtot \sim 0.5 - 0.6$. Furthermore, the distribution for simulated protons in the *only- π^0 case* is consistent with the proton component of positively charged events in flight data, thus indicating that an artificial increase of neutral pions does not drastically affect the hadronic shower development in the calorimeter and that it is still possible to obtain a clean sample of protons and positrons.

Looking at the $qtrack/qtot$ distribution for negatively charged particles in flight data selected as electrons in the upper part of the calorimeter (figure 4.7) it is possible to see that a cut $qtrack/qtot \geq 0.5$ selects about 99 % of electrons in all the three rigidity ranges. Thus, considering the comparison between positive flight particles and simulated protons in the *only- π^0 case*, the cut on $qtrack/qtot$ selects how many protons in this artificial configuration fake the positron distribution. The selection $qtrack/qtot \geq 0.5$ was used in the rigidity range 28 – 42 GV while the selection $q^3 \geq 0.52$ was used in the rigidity ranges 42 – 65 GV and 65 – 100 GV.

Furthermore, the positron fraction can be evaluated for each rigidity range and the results are shown in table 4.3. The number of positrons N_{e^+} is evaluated as difference between positively charged events in flight data and simulated protons in the *only- π^0 case* (see table 4.2) and the number of electrons N_{e^-} are negatively charged particles in flight data selected by $qtrack/qtot \geq 0.5$ (in the range 28 – 42 GV) and $qtrack/qtot \geq 0.52$ (in the ranges 42 – 65 GV and 65 – 100 GV). The last column shows the positron fraction values published by the PAMELA Collaboration in Nature [31].

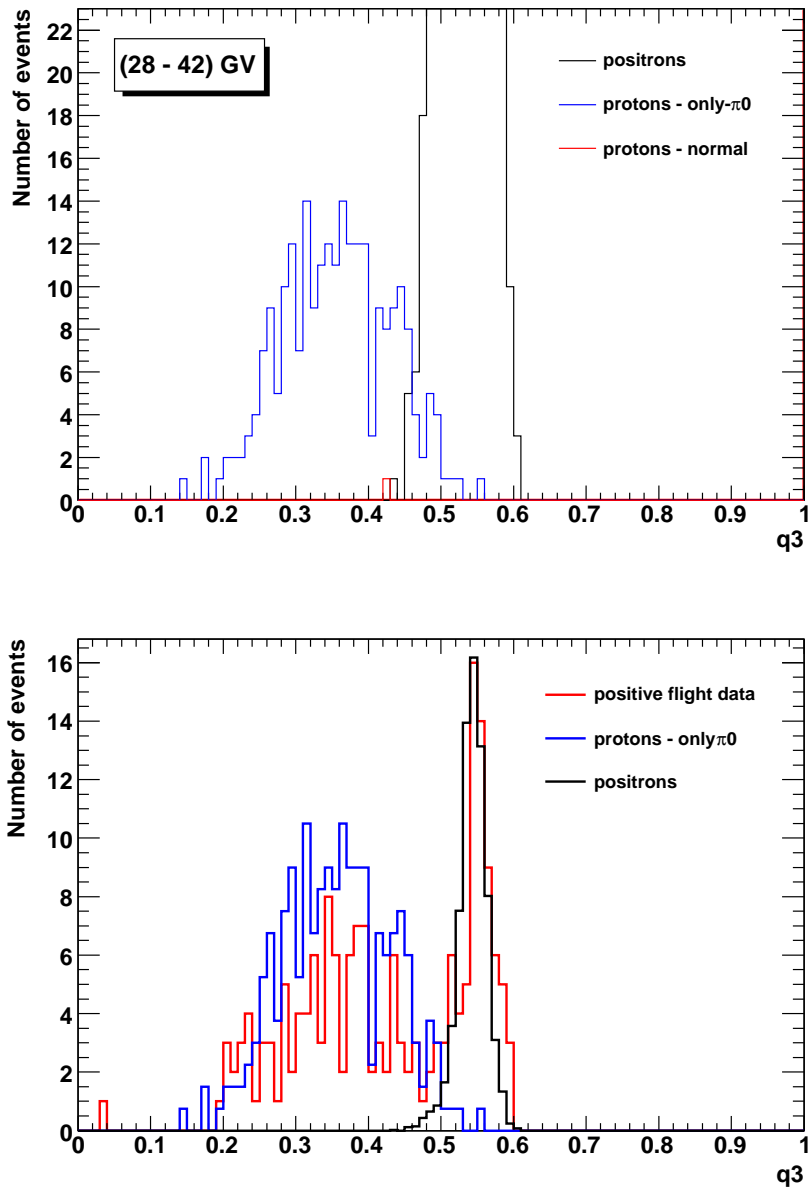


Figure 4.4. Calorimeter energy fraction in the rigidity range 28 – 42 GV. *Top:* q_{track}/q_{tot} distribution for simulated positron and proton events (*normal* and *only- π^0* case). *Bottom:* q_{track}/q_{tot} distribution for simulated positron (black line) and proton events in the *only- π^0* case (blue line) compared to the q_{track}/q_{tot} distribution for positively charged events in flight data (red line). The q_{track}/q_{tot} distributions for simulated positron and proton events are normalized to the q_{track}/q_{tot} distribution for positively charged events in flight data.

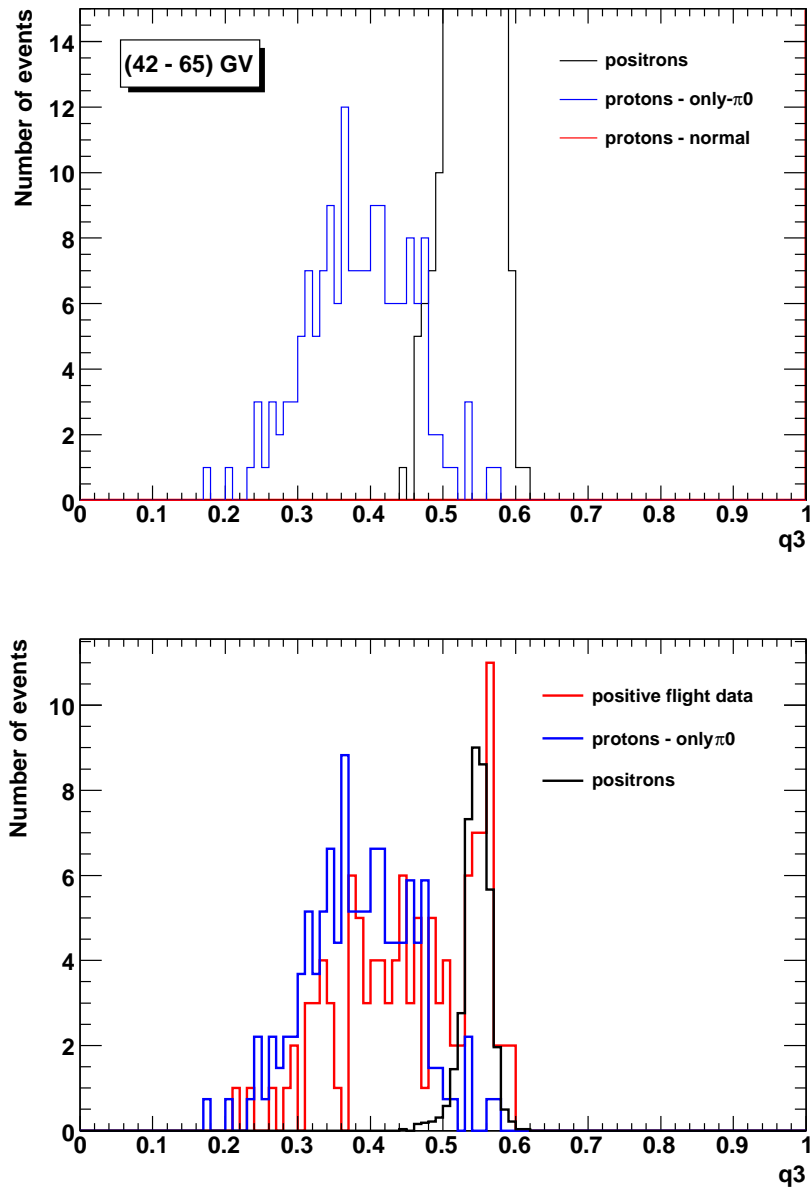


Figure 4.5. Calorimeter energy fraction in the rigidity range 42 – 65 GV. *Top:* $q_{\text{track}}/q_{\text{tot}}$ distribution for simulated positron and proton events (*normal* and *only- π^0* case). *Bottom:* $q_{\text{track}}/q_{\text{tot}}$ distribution for simulated positron (black line) and proton events in the *only- π^0* case (blue line) compared to the $q_{\text{track}}/q_{\text{tot}}$ distribution for positively charged particles in flight data (red line). The $q_{\text{track}}/q_{\text{tot}}$ distributions for simulated positron and proton events are normalized to the $q_{\text{track}}/q_{\text{tot}}$ distribution for positively charged events in flight data.

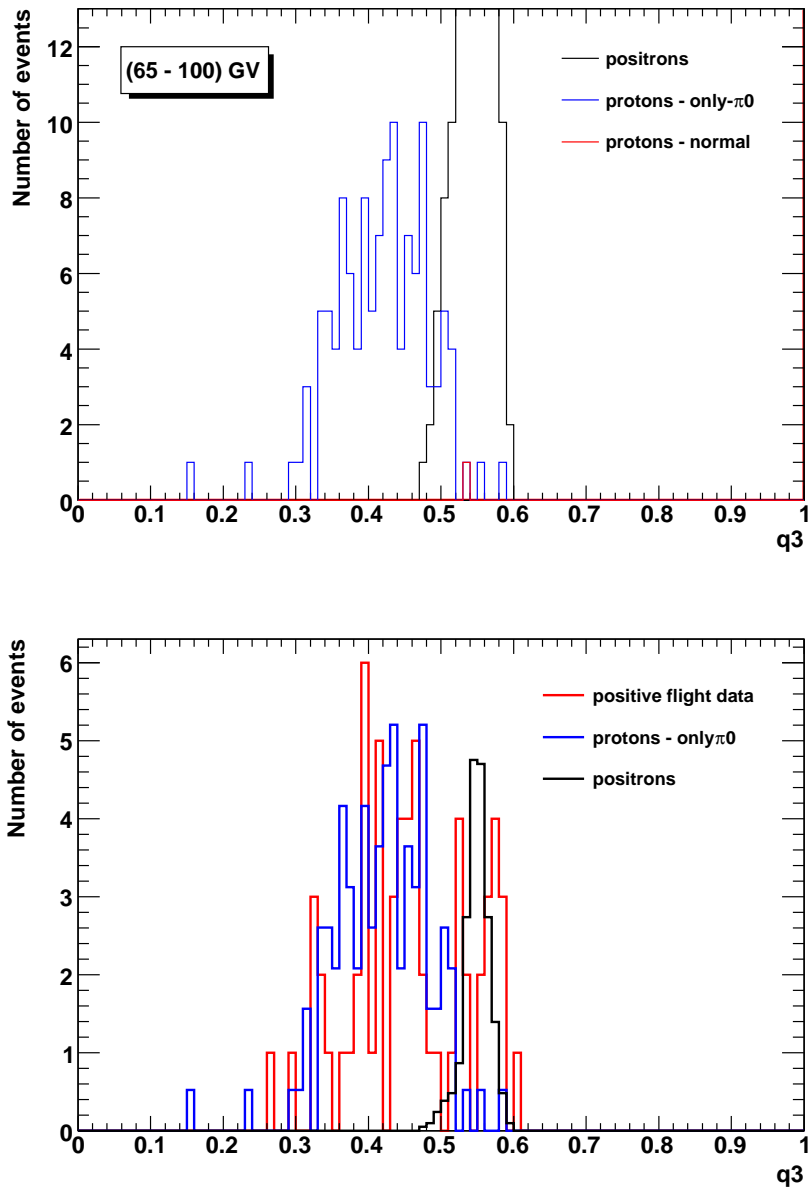


Figure 4.6. Calorimeter energy fraction in the rigidity range 65 – 100 GV. *Top:* $q_{\text{track}}/q_{\text{tot}}$ distribution for simulated positron and proton events (*normal* and *only- π^0* case). *Bottom:* $q_{\text{track}}/q_{\text{tot}}$ distribution for simulated positron (black line) and proton events in the *only- π^0* case (blue line) compared to the $q_{\text{track}}/q_{\text{tot}}$ distribution for positively charged particles in flight data (red line). The $q_{\text{track}}/q_{\text{tot}}$ distributions for simulated positron and proton events are normalized to the $q_{\text{track}}/q_{\text{tot}}$ distribution for positively charged events in flight data.

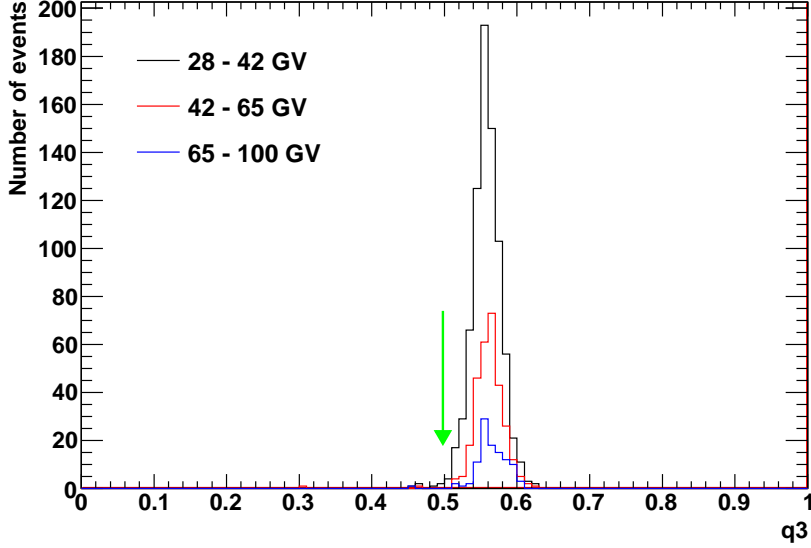


Figure 4.7. q_{track}/q_{tot} distribution for negatively charged particles in flight data selected as electrons in the upper part of the calorimeter and in the rigidity range 28 – 42 GV (black line), 42 – 65 GV (red line), 65 – 100 GV (blue line). The green arrow shows the cut $q_{track}/q_{tot} \geq 0.5$ which selects 99 % of electrons.

Rigidity (GV)	p <i>only-π^0</i>	positive particles	p <i>only-π^0</i> / positive particles
28 - 42	$3 \begin{smallmatrix} + 5 \\ - 2 \end{smallmatrix}$	71	$0.042 \begin{smallmatrix} + 0.066 \\ - 0.030 \end{smallmatrix}$
42 - 65	$4 \begin{smallmatrix} + 5 \\ - 3 \end{smallmatrix}$	39	$0.102 \begin{smallmatrix} + 0.131 \\ - 0.067 \end{smallmatrix}$
65 - 100	$2 \begin{smallmatrix} + 4 \\ - 2 \end{smallmatrix}$	19	$0.105 \begin{smallmatrix} + 0.226 \\ - 0.086 \end{smallmatrix}$

Table 4.2. Number of events selected by the criteria listed in section 4.4 for simulated protons in the *only- π^0* case and for positively charged events in flight data in three different rigidity ranges (related to bottom plots of figures 4.4, 4.5 and 4.6). Also, the selection $q_{track}/q_{tot} \geq 0.5$ was used in the rigidity range 28 – 42 GV and the selection $q_3 \geq 0.52$ was used in the rigidity ranges 42 – 65 GV and 65 – 100 GV. The last column shows how many protons in this artificial configuration can fake the positron q_{track}/q_{tot} distribution. The errors have been evaluated at 90 % confidence level.

The comparison between the positron fraction evaluated in this artificial configuration with the positron fraction published in Nature is also shown in figure 4.24. The agreement is good thus indicating that the rise in the positron fraction for energies greater than 10 GeV is not due to misidentified positrons from π^0 contamination.

Rigidity (GV)	N_{e^+}	N_{e^-}	$N_{e^+} / (N_{e^+} + N_{e^-})$ this analysis	$N_{e^+} / (N_{e^+} + N_{e^-})$ Nature analysis
28 - 42	$68 \pm \begin{smallmatrix} 14 \\ -13 \end{smallmatrix}$	780	$0.080 \pm \begin{smallmatrix} 0.016 \\ -0.015 \end{smallmatrix}$	0.0831 ± 0.0093
42 - 65	$35 \pm \begin{smallmatrix} 11 \\ -10 \end{smallmatrix}$	292	$0.107 \pm \begin{smallmatrix} 0.031 \\ -0.029 \end{smallmatrix}$	$0.106 \pm \begin{smallmatrix} 0.022 \\ -0.023 \end{smallmatrix}$
65 - 100	$17 \pm \begin{smallmatrix} 8 \\ -7 \end{smallmatrix}$	101	$0.144 \pm \begin{smallmatrix} 0.061 \\ -0.054 \end{smallmatrix}$	$0.137 \pm \begin{smallmatrix} 0.048 \\ -0.043 \end{smallmatrix}$

Table 4.3. Values of the positron fraction in three different rigidity ranges. The number of positrons N_{e^+} is evaluated as difference between positively charged events in flight data and simulated protons in the *only- π^0 case* (see table 4.2); the number of electrons N_{e^-} are negatively charged particles in flight data selected by $qtrack/qtot \geq 0.5$ in the rigidity range 28 – 42 GV and by $qtrack/qtot \geq 0.52$ in the rigidity ranges 42 – 65 GV and 65 – 100 GV; the errors have been evaluated at 90 % confidence level. The last column shows the positron fraction values published by the PAMELA Collaboration in Nature [31].

The conclusions of this analysis can be summarized as follows:

- the approach followed in the Nature analysis permits a clean sample of positrons and protons to be selected; this clearly appears in the $qtrack/qtot$ distribution of positively charged particles in flight data which can be fully described considering two components: these components are well reproduced by simulations of protons in the *only- π^0 case* and positrons (see figures 4.4, 4.5 and 4.6);
- even in the artificial case when all the charged pions are converted into neutral ones, it is impossible to reproduce a double peaked $qtrack/qtot$ distribution. The distribution is consistent with the proton component in positive flight data; π^0 contamination can therefore be excluded;
- the positron fraction evaluated from proton simulations in the *only- π^0 case* is compatible with the positron fraction values published by the PAMELA Collaboration in Nature [31] (see table 4.3 and figure 4.24); thus the rise in the positron fraction for energies greater than 10 GeV is not due to misidentified positrons from π^0 contamination as argued by Schubnell [77];
- the discrimination between positron and proton events following the Nature approach becomes problematic at energies around 100 GeV.

The remainder of this chapter describes a method to improve positron selection in the calorimeter for energies greater than 100 GeV.

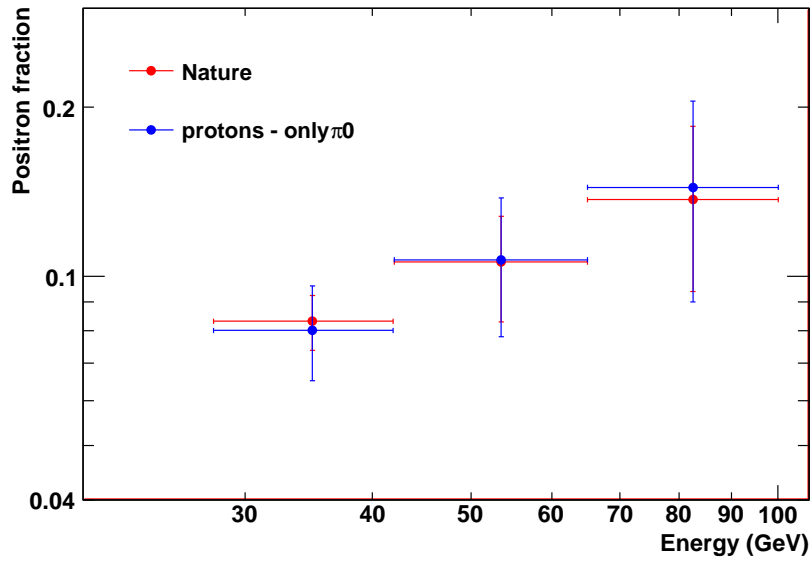


Figure 4.8. Positron fraction as function of the energy evaluated using simulations of protons in the *only- π^0* case (blue points) compared to the values published in Nature [31] (red points); the values with errors are listed in table 4.3. The full version of the positron fraction measured by the PAMELA experiment is shown in figure 1.10 [31].

4.6 A new approach for positron identification

As described in section 4.5, around 100 GeV the discrimination of the energy fraction distribution between electromagnetic and hadronic showers starts being less efficient. Thus, in view of extending the positron fraction up to ~ 300 GeV, a new approach for positron identification, based on a combination of shower profile variables in the calorimeter, has been tested on simulations in the energy ranges 20 – 100 GeV and 100 – 300 GeV.

As described in section 3.4.1, shower profile variables assume different values in hadronic and electromagnetic showers (see also figures ?? and 3.10). Thus, these variables could be very efficient in selecting proton or positron events. Variable distributions for both proton and positron events have been studied in order to obtain an efficient positron selection. In particular, the goal of this selection study is to answer the following questions:

- is it possible to discriminate between positrons and protons (*only- π^0 case*) for energies greater than 100 GeV in an efficient way?
- what are the shower profile variables which permit the most efficient selection?

All the shower profile variables depend on the reconstructed rigidity of the simulated particles. Thus, in order to identify which variables permit the most efficient discrimination between positrons and protons, distributions of variables as a function of the reconstructed rigidity have been studied. Figure 4.9 shows the ratio between the energy deposited in a cylinder of radius eight silicon strips around the shower axis, $qcyl$, and the number of strips hit inside the same cylinder, $ncyl$, for simulated positrons (black points) and protons (red points).

The first step in this procedure was to choose shower profile variables for which distributions as function of the rigidity are well separated between positron and proton simulated events (as in figure 4.9). Then, the χ^2 variable was constructed using different shower profile variable combinations in order to find the one that selects positrons in the most efficient way.

The χ^2 variable is constructed in the following way:

$$\chi^2 = \sum_{i=1}^n \chi_{variable[i]}^2 = \sum_{i=1}^n \frac{(variable[i] - \overline{variable[i]})^2}{\sigma_{variable[i]}^2} \quad (4.2)$$

where n is the number of shower profile variables considered.

For each variable, the mean and the standard deviation values are functions of the tracker reconstructed rigidity. For instance, figure 4.10-*top* shows the distribution of the energy fraction along the track ($qtrack/qtot$) as a function of the rigidity for simulated positrons in the energy range 20 – 100 GeV. The variable $qtrack$ is the energy deposited in the strips along the track and in the neighbouring strips on each side of the track and $qtot$ is the total energy detected in the calorimeter (see section 3.4.1 for further description). Observing this plot in rigidity slices, the values of the energy fraction follow a Gaussian distribution with a certain mean and

standard deviation in each rigidity interval. The distribution of the energy fraction in the rigidity interval 30 – 32 GV is shown in figure 4.10-*bottom* and is well described by a Gaussian distribution. This procedure was repeated for each rigidity interval, thus obtaining a distribution of $\overline{qtrack/qtot}$ and $\sigma_{qtrack/qtot}$ as a function of the rigidity. These distributions have been fitted in the reconstructed rigidity range 20 – 100 GV and the best fit equations are respectively (see figure 4.11):

$$\overline{qtrack/qtot} = 0.5367 + 0.0001929 \cdot rigidity \quad (4.3)$$

$$\sigma_{qtrack/qtot} = -0.6308 + e^{-0.423 - 0.0001909 \cdot rigidity} \quad (4.4)$$

The same procedure as illustrated for the variable $qtrack/qtot$ has been applied to other shower profile variables. The distributions of $variable[i]$ and $\sigma_{variable[i]}$ have been fitted with linear or exponential functions.

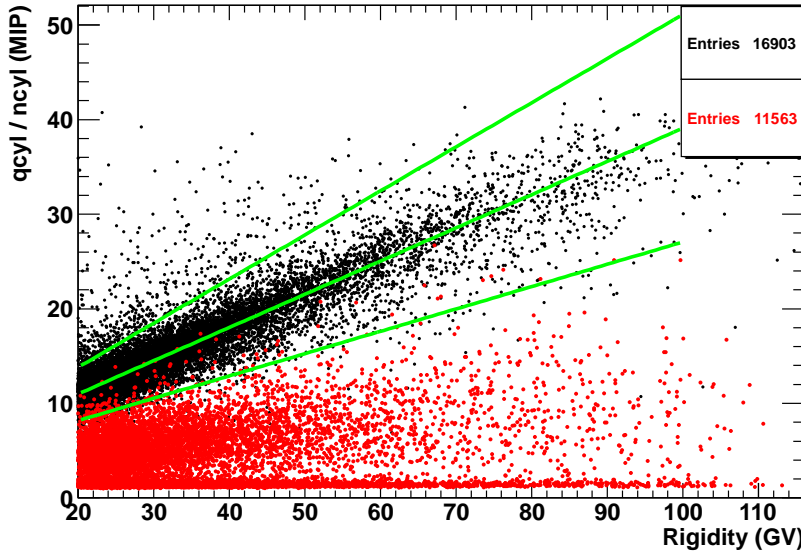


Figure 4.9. Distribution of $qcyl/ncyl$ as function of the reconstructed rigidity for simulated positrons (black points) and protons *normal case* (red points) in the energy range 20 – 100 GeV; the green lines show the mean value $qcyl/ncyl$ and $qcyl/ncyl \pm 3 \cdot \sigma_{qcyl/ncyl}$.

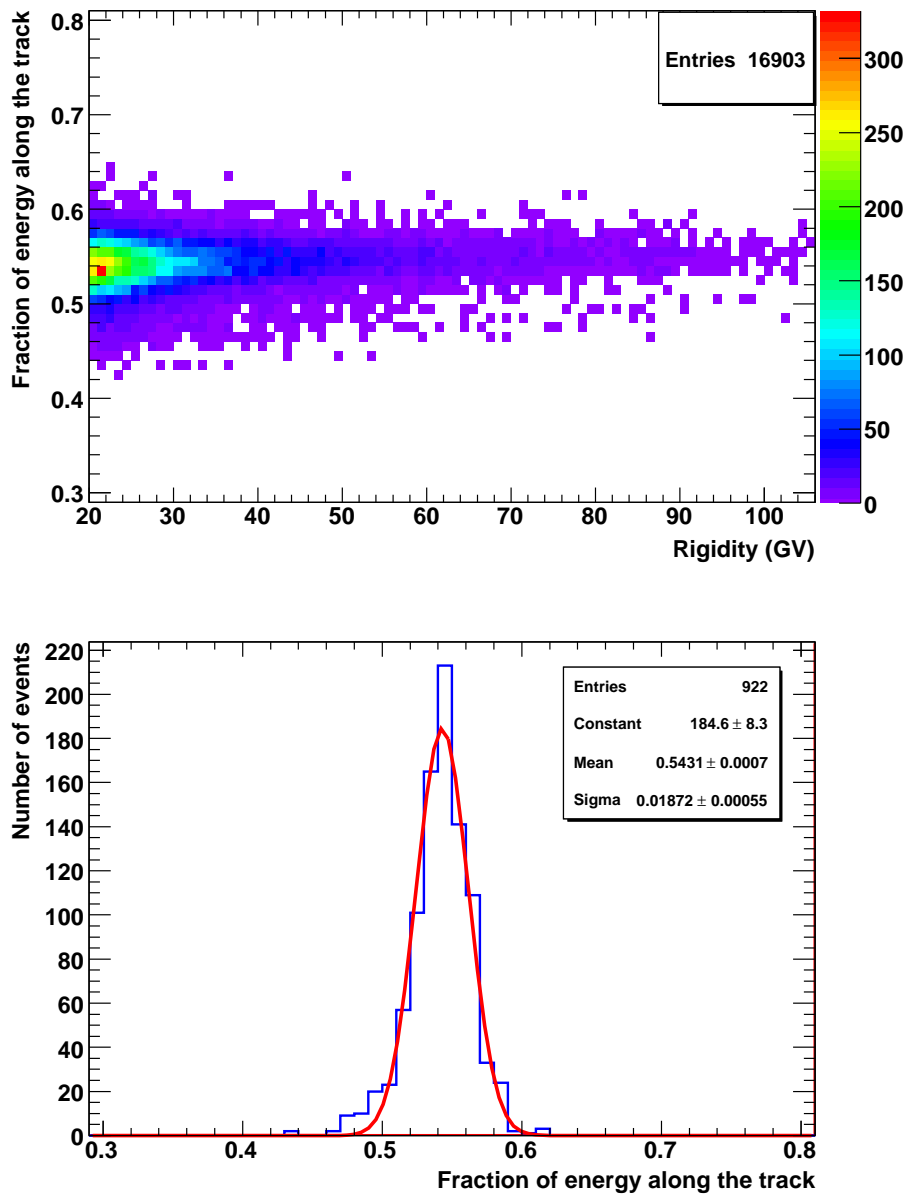


Figure 4.10. *Top:* distribution of the energy fraction along the track (q_{track}/q_{tot}) as a function of the reconstructed rigidity for simulated positrons in the energy range 20 – 100 GeV. *Bottom:* distribution of the energy fraction along the track (q_{track}/q_{tot}) in the rigidity interval 30 – 32 GV for simulated positrons in the energy range 20 – 100 GeV (blue line). The values are well approximated by a Gaussian distribution (red line).

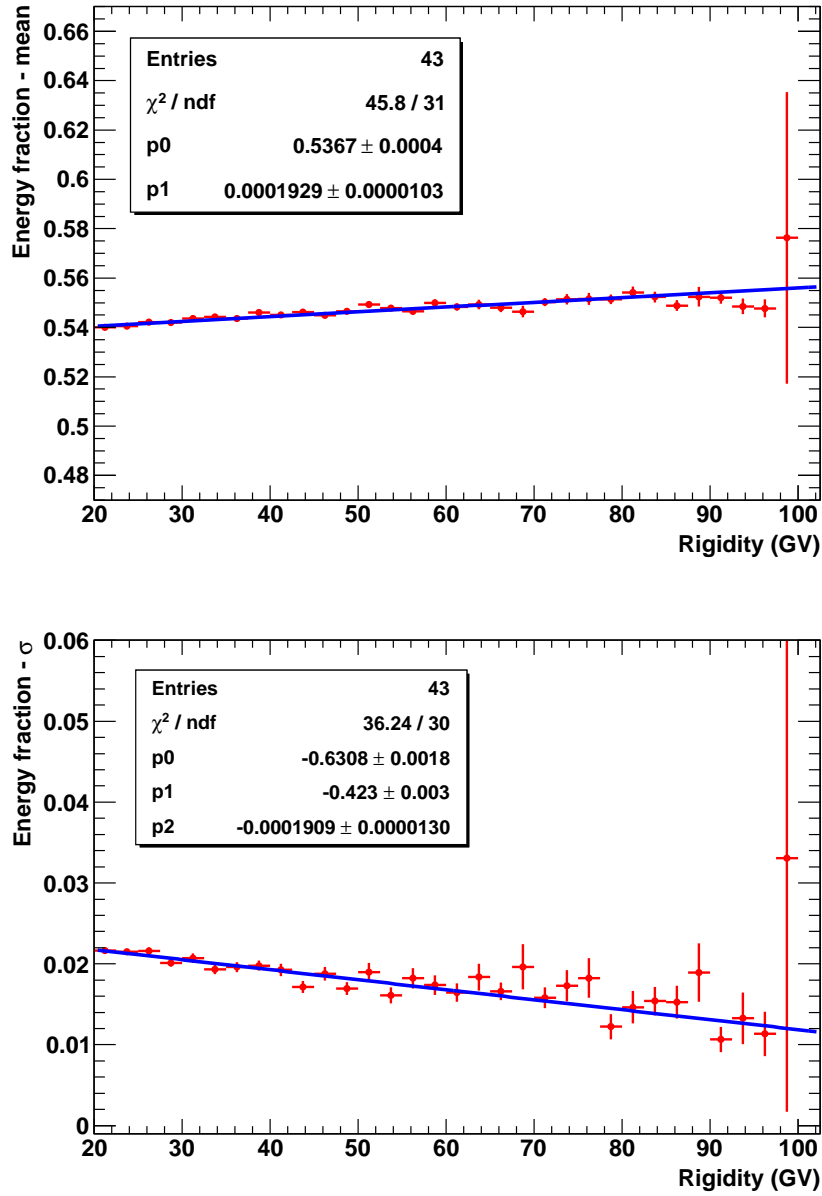


Figure 4.11. *Top*: distribution of mean values of the energy fraction along the track as a function of the reconstructed rigidity (red points); the best fit is also shown (blue line) and has equation: $\overline{q_{track}/q_{tot}} = 0.5367 + 0.0001929 \cdot \text{rigidity}$. *Bottom*: distribution of standard deviation values of the energy fraction along the track as a function of the reconstructed rigidity (red points); the best fit is also shown (blue line) and has equation: $\sigma_{q_{track}/q_{tot}} = -0.6308 + e^{-0.423 - 0.0001909 \cdot \text{rigidity}}$.

4.7 Analysis in the energy range 20 – 100 GeV

As already mentioned in section 4.5, the method [31] followed to evaluate the positron fraction starts being less efficient at energies around 100 GeV. In order to extend the positron fraction up to ~ 300 GeV, a new approach based on a combination of shower profile variables in the calorimeter has been studied. This new method has been initially tested in the energy range 20 – 100 GeV and the resulting positron fraction has been compared to the one published in [66] (see section 4.9).

4.7.1 Positron selection efficiencies

As already mentioned in section 4.6, selection criteria on shower profile variables have been studied in order to obtain an efficient positron selection. Positron selection criteria have been tuned on simulated positron samples in order to obtain a good positron selection efficiency. These same positron selection criteria have then been applied to proton simulation samples (both *normal* and *only- π^0 case*) in order to study the electromagnetic contamination of hadronic showers, i.e. how many protons are misidentified as positrons. The combination which selects positrons with the highest efficiency and with the lowest proton contamination (see section 4.7.2) was found to be:

1. $\overline{ncore} - 3 \cdot \sigma_{ncore} < ncore < \overline{ncore} + 3 \cdot \sigma_{ncore}$
2. $ncyl > \overline{ncyl} - 3 \cdot \sigma_{ncyl}$
3. $\overline{qcyl/ncyl} - 3 \cdot \sigma_{qcyl/ncyl} < qcyl/ncyl < \overline{qcyl/ncyl} + 3 \cdot \sigma_{qcyl/ncyl}$
4. $qpresh > 50$
5. $qtot/nstrip > 6$
6. $\chi^2 < \chi_{cut}^2$

where

$$\begin{aligned} \chi^2 &= \sum_{i=1}^6 \chi_{variable[i]}^2 \\ &= \chi_{ncore}^2 + \chi_{q3}^2 + \chi_{qpresh}^2 + \chi_{ncyl}^2 + \chi_{qcyl/ncyl}^2 + \chi_{qtot/nstrip}^2 \end{aligned} \quad (4.5)$$

Thus, criteria listed in section 4.4.4 have been substituted by these new six selections.

The cut on the χ^2 variable dominates the selection efficiency and many combinations of different shower profile variables have been used in order to obtain the best positron selection efficiency with the smallest proton contamination (see section 4.7.2). By definition, equation 4.2 is a χ^2 distribution with n degrees of freedom, where n is the number of shower profile variables considered. In this case (equation 4.5) the χ^2 is constructed using six variables: thus, if the six variables

are totally independent the probability for a χ^2 distribution to be ≤ 6 for 6 degrees of freedom is $\sim 60\%$. Figure 4.12 shows the χ^2 distribution as a function of the reconstructed rigidity. The distribution shows a peak around $\chi^2 = 2$ and a cut $\chi^2 < 6$ selects 63.3% of the events.

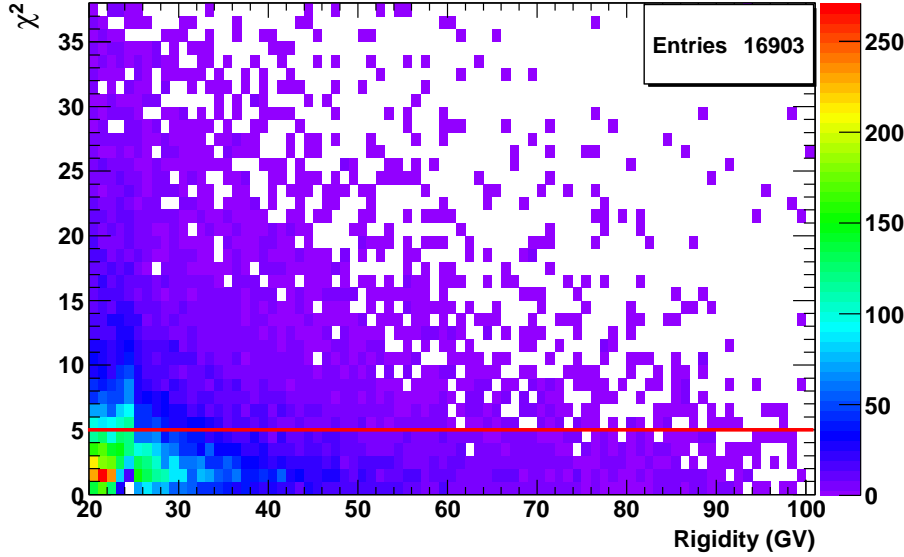


Figure 4.12. Distribution of the χ^2 variable (equation 4.5) as a function of rigidity for simulated positrons in the energy range 20 – 100 GeV; the red line shows $\chi^2 = 5$. The cut $\chi^2 < 5$ selects 56.9% of the events as positrons.

Using all the selections described in section 4.4 the selection efficiencies of the cuts described above were studied for different values of χ^2_{cut} . The positron selection efficiency is given by the ratio between the selections listed above and those listed in section 4.4. The number of positrons which pass the selections listed in section 4.4 are 16903 for 10^5 simulated positrons. Figure 4.13-*bottom* shows the trend of the selection efficiencies for different values of χ^2_{cut} for simulated positrons in the energy range 20 – 100 GeV. Thus, choosing for instance a value of $\chi^2_{cut} = 5$, the positron selection efficiency is $\sim 57\%$. Some results for different values of χ^2_{cut} shown in figure 4.13-*bottom* are also summarized in table 4.4.

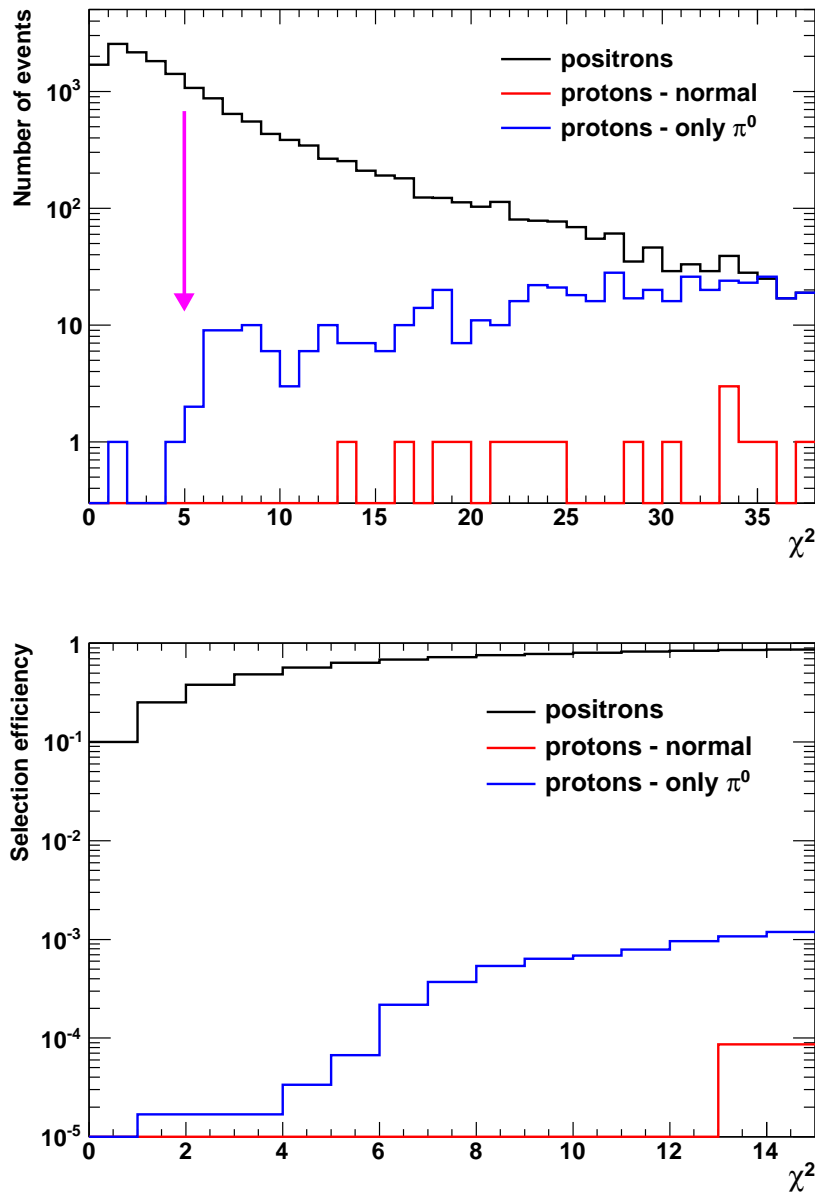


Figure 4.13. *Top:* distribution of the χ^2 variable (equation 4.5) for simulated positrons (black line), protons in the *normal case* (red line) and protons in the *only- π^0 case* (blue line); simulations have been produced in the energy range 20 – 100 GeV; the purple arrow shows $\chi^2 = 5$. *Bottom:* selection efficiencies for different cut values on the variable χ^2 (equation 4.5); the positron selection efficiency (black line) is compared to the protons selection efficiency in the *normal case* (red line) and in the *only- π^0 case* (blue line).

4.7.2 Proton contamination

The same selections described in sections 4.4 and 4.7.1, previously applied to simulated positrons, have been then applied to simulated protons in order to study the contamination, i.e. how many protons pass the positron selections. Figure 4.13-*bottom* shows the trend of the selection efficiency as a function of χ_{cut}^2 for protons in the *normal case* (red line) and in the *only- π^0 case* (blue line) together with the positron selection efficiency (black line). In this case, the proton selection efficiency is given by the ratio between the number of proton events which pass the selections listed in section 4.7.1 and those which pass the selections listed in section 4.4. Simulating 10^5 protons in the *normal case* and $5 \cdot 10^5$ protons in the *only- π^0 case*, the number of protons in the two cases which pass the selections listed in section 4.4 are respectively 11563 and 59575. Observing figure 4.13-*bottom* one can notice that:

- no proton events are selected as positrons in the *normal case* up to high χ_{cut}^2 values (> 13);
- the number of proton events selected as positrons in the *only- π^0 case* is of order of 10^{-5} for $\chi_{cut}^2 < 6$.

Furthermore, for each value of χ_{cut}^2 the proton contamination is evaluated considering the corresponding positron selection efficiency:

$$\text{proton contamination} = \frac{\text{proton selection efficiency}}{\text{positron selection efficiency}} \quad (4.6)$$

Some results for different χ_{cut}^2 values are summarized in table 4.4.

<i>Only-π^0 case</i>			
χ_{cut}^2	e ⁺ efficiency	p efficiency	proton contamination
3	0.379 ± 0.007	$(1.7 \begin{smallmatrix} + 6.3 \\ - 1.6 \end{smallmatrix}) \cdot 10^{-5}$	$(0.45 \begin{smallmatrix} + 1.67 \\ - 0.42 \end{smallmatrix}) \cdot 10^{-4}$
4	0.486 ± 0.008	$(1.7 \begin{smallmatrix} + 6.3 \\ - 1.6 \end{smallmatrix}) \cdot 10^{-5}$	$(0.35 \begin{smallmatrix} + 1.30 \\ - 0.33 \end{smallmatrix}) \cdot 10^{-4}$
5	0.569 ± 0.009	$(3.4 \begin{smallmatrix} + 7.2 \\ - 2.8 \end{smallmatrix}) \cdot 10^{-5}$	$(0.60 \begin{smallmatrix} + 1.27 \\ - 0.49 \end{smallmatrix}) \cdot 10^{-4}$
6	0.633 ± 0.010	$(6.7 \begin{smallmatrix} + 8.6 \\ - 4.4 \end{smallmatrix}) \cdot 10^{-5}$	$(1.06 \begin{smallmatrix} + 1.36 \\ - 0.70 \end{smallmatrix}) \cdot 10^{-4}$
7	0.684 ± 0.010	$(2.2 \pm 1.0) \cdot 10^{-4}$	$(3.22 \pm 1.46) \cdot 10^{-4}$

Table 4.4. Proton selection efficiency and proton contamination for different values of χ_{cut}^2 (equation 4.5). The analysis was performed on $5 \cdot 10^5$ simulated protons in the *only- π^0 case* and in the energy range 20 – 100 GeV. The errors have been evaluated at 90 % confidence level. The number of protons which passes the selections listed in section 4.4 are 59575.

Thus, choosing a value of $\chi_{cut}^2 = 5$ no contamination is found for simulated protons in the *normal case* while a contamination of $6.0 \cdot 10^{-5}$ is found for protons

in the *only- π^0* case. Using this kind of analysis some conclusions can be summarized as follows:

- the shower profile variables $ncore$, $q3$, $qpresh$, $ncyl$, $qcyl/ncyl$ and $qtot/nstrip$ permit a relatively efficient positron selection ($\sim 57\%$ considering a $\chi^2_{cut} = 5$);
- the shower profile variables used for positron selection yield no proton contamination in the *normal case* sample;
- considering that the proton-to-positron flux ratio at 100 GV is approximately 10^4 [31], the proton contamination should be lower than $\sim 10^{-5}$. The proton contamination in the *only- π^0* case sample is of order of 10^{-5} with a corresponding positron selection efficiency of $\sim 57\%$, i.e. the discrimination between positrons and protons is acceptable considering the fact that this is an artificial case where all the charged pions are converted into neutral ones and thus the contamination should be highest.

4.8 Analysis in the energy range 100 – 300 GeV

The new method for positron identification described in section 4.6 and tested in the energy range 20 – 100 GeV (see section 4.7) can be extended to energies greater than 100 GeV. As described in section 1.5.1, many different interpretations were proposed in order to explain the PAMELA positron fraction rise above 10 GeV. Extending the measurement of the positron fraction to energies greater than 100 GeV could possibly help in understanding the reason behind this rise. Thus, the new approach has been tested on simulations in the energy range 100 – 300 GeV and then applied to flight data in order to estimate the number of positron and electron events. The positron fraction has been consequently evaluated in a new energy range and is presented in section 4.9.

At energies above 100 GeV some shower profile variables used for the analysis in the energy range 20 – 100 GeV are no longer efficient in separating between electromagnetic and hadronic cascades. Above 100 GeV a non-negligible fraction of electromagnetic showers are not fully contained in the calorimeter, thus some shower profile variables can no longer be used to identify positron events over the overwhelming proton background. Some of these variables are for instance the number of hit strips and the energy released in the last calorimeter planes, and the average energy released in each calorimeter strip i.e. $qtot/nstrip$. Many variable distributions have been studied as a function of rigidity in order to find the combination that selects the greatest number of positrons with the lowest proton contamination. Figure 4.14 shows the distribution of the variable $qcore/ncore$ (see section 3.4.1) as a function of rigidity for simulated positrons (black points) and protons in the *normal case* (red points). The mean and the standard deviation are also a function of the reconstructed rigidity and have been evaluated following the method described in section 4.6. The mean value $\overline{qcore/ncore}$ and the functions $\overline{qcore/ncore} \pm 3 \cdot \sigma_{qcore/ncore}$ are also shown in figure 4.14 (green lines).

The selection criterion $qcore/ncore > \overline{qcore/ncore} - 3 \cdot \sigma_{qcore/ncore}$ was first applied to simulated positron and proton samples and, after this selection, other shower profile variables have been studied as a function of rigidity. Figures 4.15 and 4.16 show the distribution of some shower profile variables for simulated positrons (black points) and protons in the *normal case* (red points). Looking at these shower profile variable distributions it is evident that even if many proton events still overlap the positron ones, for most of the variables considered protons lie in the tails of the positron distributions. Thus, the χ^2 method could help in removing part of these proton events.

The following two selections have been applied to the simulated positron and proton sample (see section 3.4.1 for variable definitions):

1. $qcore/ncore > \overline{qcore/ncore} - 3 \cdot \sigma_{qcore/ncore}$
2. $\chi^2 < \chi_{cut}^2$

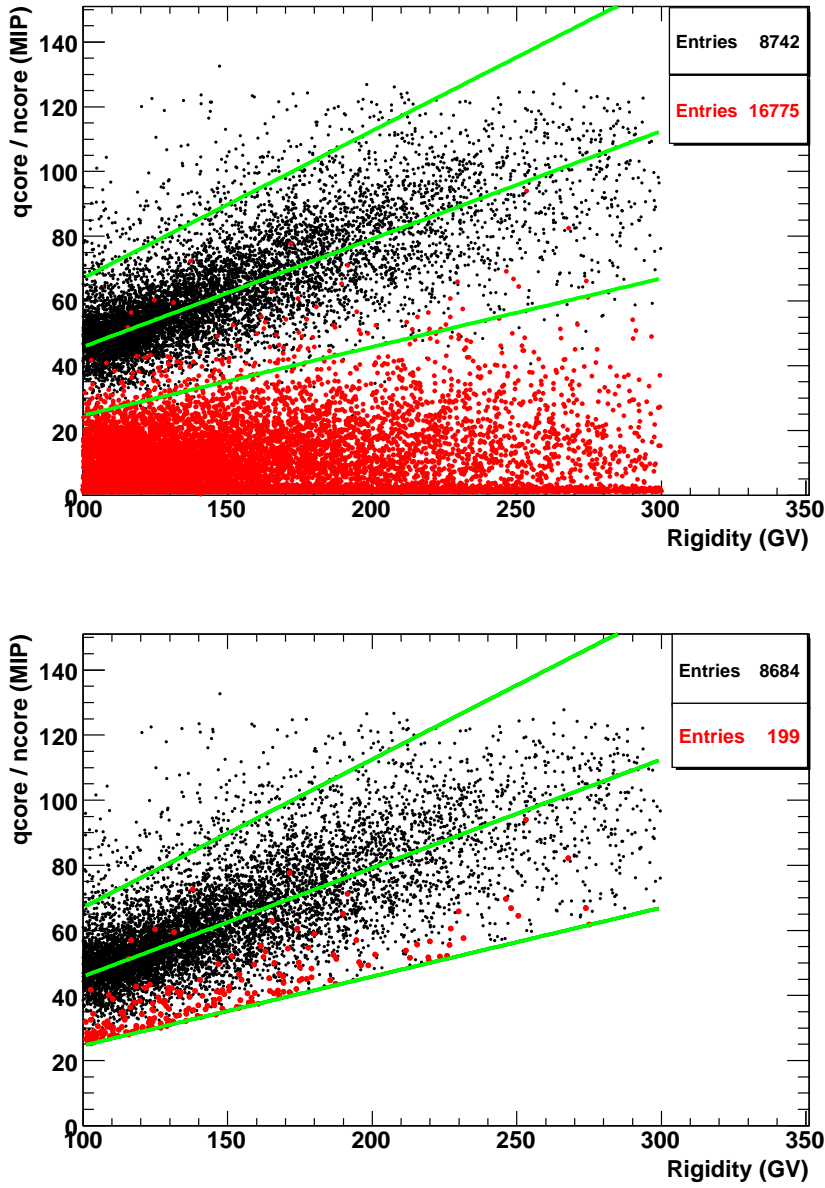


Figure 4.14. *Top:* q_{core}/n_{core} distribution as a function of rigidity for simulated positrons (black points) and protons *normal case* (red points); the green lines show the mean q_{core}/n_{core} and $q_{core}/n_{core} \pm 3 \cdot \sigma_{q_{core}/n_{core}}$. *Bottom:* q_{core}/n_{core} distribution for simulated positrons (red points) and protons (black points) after the selection $q_{core}/n_{core} > q_{core}/n_{core} - 3 \cdot \sigma_{q_{core}/n_{core}}$. Simulations have been produced in the energy range 100 – 300 GeV.

where

$$\begin{aligned}
 \chi^2 &= \sum_{i=1}^8 \chi_{variable[i]}^2 \\
 &= \chi_{qpre/npre}^2 + \chi_{qpre}^2 + \chi_{q0}^2 + \chi_{e0imp}^2 + \chi_{v3sihit}^2 + \chi_{asymmetry}^2 \\
 &\quad + \chi_{enfitatmaxns}^2 + \chi_{aveder}^2
 \end{aligned}
 \tag{4.7}$$

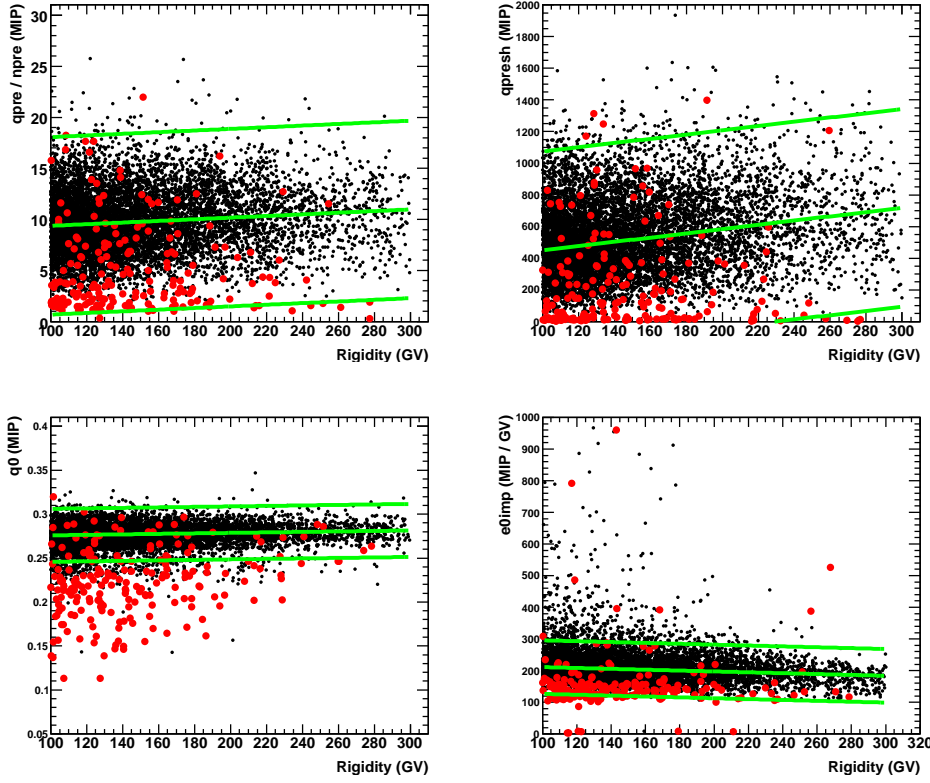


Figure 4.15. Distribution of shower profile variables as a function of rigidity for simulated positrons (black points) and protons *normal case* (red points); the green lines show the mean *variable* and $variable \pm 3 \cdot \sigma_{variable}$. Simulations have been produced in the energy range 100 – 300 GeV.

Using all the selections described in section 4.4 the positron selection efficiencies of the cuts described above and the corresponding proton contamination were

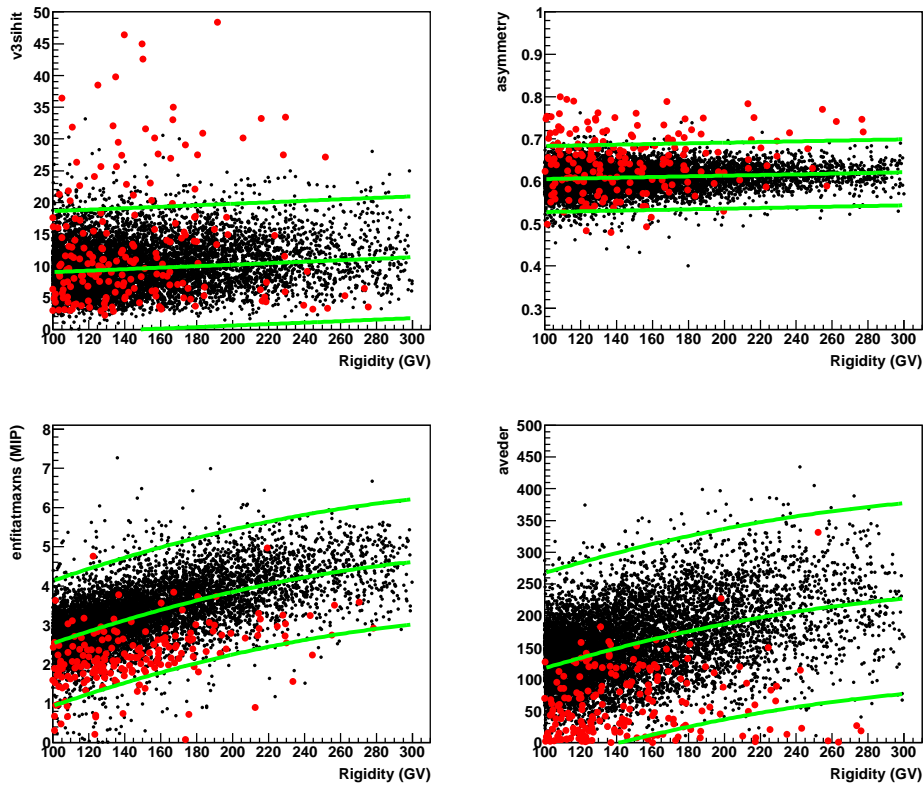


Figure 4.16. Distribution of shower profile variables as a function of rigidity for simulated positrons (black points) and protons *normal case* (red points); the green lines show *variable* and $variable \pm 3 \cdot \sigma_{variable}$. Simulations have been produced in the energy range 100 – 300 GeV.

studied for different values of χ^2_{cut} . In this case the χ^2 is constructed using eight variables: thus, if the eight variables are totally independent the probability for a χ^2 distribution to be ≤ 8 for 8 degrees of freedom is $\sim 50\%$. Figure 4.17 shows the χ^2 distribution as a function of the reconstructed rigidity for simulated positrons (black line), protons in the *normal case* (red line) and in the *only- π^0 case* (blue line). The distribution for simulated positrons shows a peak around $\chi^2 = 4$ and a cut $\chi^2 < 8$ selects 52.3 % of positron events. This appears also in figure 4.18 where the efficiency of the selections listed above is plotted as a function of χ^2_{cut} for simulated positron and proton events. Thus, considering the selection $\chi^2 < 8$, the corresponding proton contamination (equation 4.6) is $1.1 \cdot 10^{-4}$ for protons in the *normal case* and $2.5 \cdot 10^{-4}$ for protons in the *only- π^0 case*.

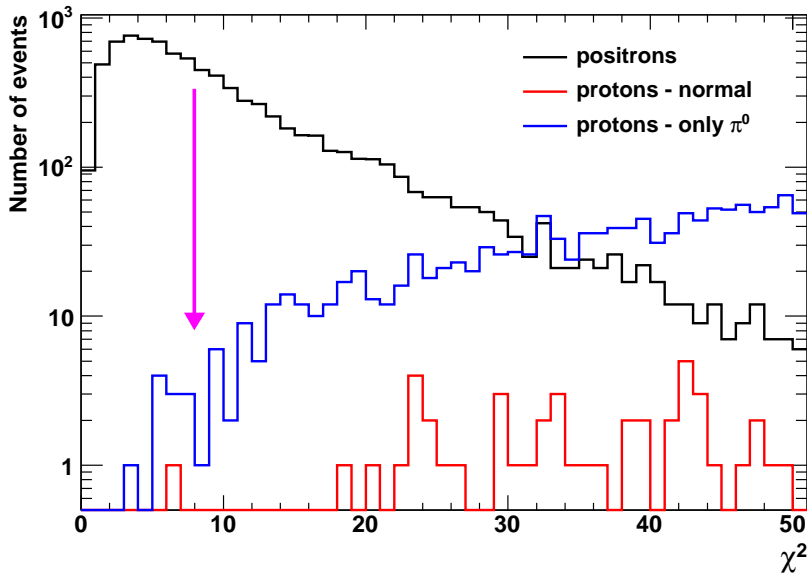


Figure 4.17. Distribution of the χ^2 variable (equation 4.7) for simulated positrons (black line), protons in the *normal case* (red line) and in the *only- π^0 case* (blue line); simulations have been produced in the energy range 100 – 300 GeV; the purple arrow shows $\chi^2 = 8$.

The purpose of this study is to find a method which selects positrons with the highest efficiency and with the lowest proton contamination, i.e. lower than $\sim 10^{-5}$. The positron sample selected through the criteria listed in section 4.7 is still contaminated by protons. Thus, in order to reduce the proton contamination, it is necessary to add other selections using different shower profile variables. Figure 4.19 shows some variable distributions as a function of rigidity for simulated positrons and protons after the selections listed in section 4.4 and with $\chi^2_{cut} = 8$ (equa-

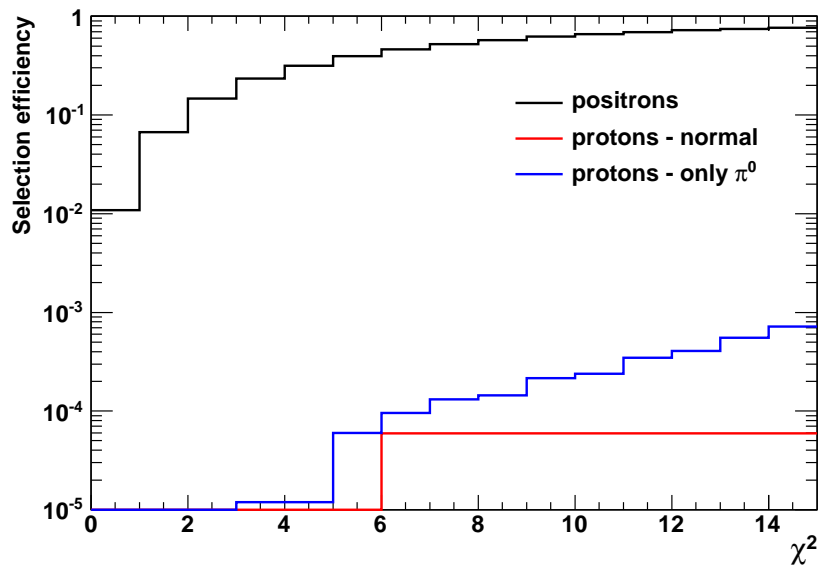


Figure 4.18. Selection efficiency as function of cut values on χ^2 (equation 4.7) and for simulations in the energy range 100 – 300 GeV; the positrons selection efficiency (black line) is compared to the protons selection efficiency in the *normal case* (red line) and in the *only- π^0* case (blue line).

tion 4.7). Few simulated proton events in the *only- π^0* case lie in the tails of the positron distributions. Thus, the proton contamination could be reduced applying a cut on the χ^3 distribution constructed as follows (see section 3.4.1 for variable definitions):

$$\begin{aligned}\chi^3 &= \sum_{i=1}^3 \chi_{variable[i]}^3 \\ &= \chi_{qtotimp}^3 + \chi_{v4siq}^3 + \chi_{q4}^3\end{aligned}\quad (4.8)$$

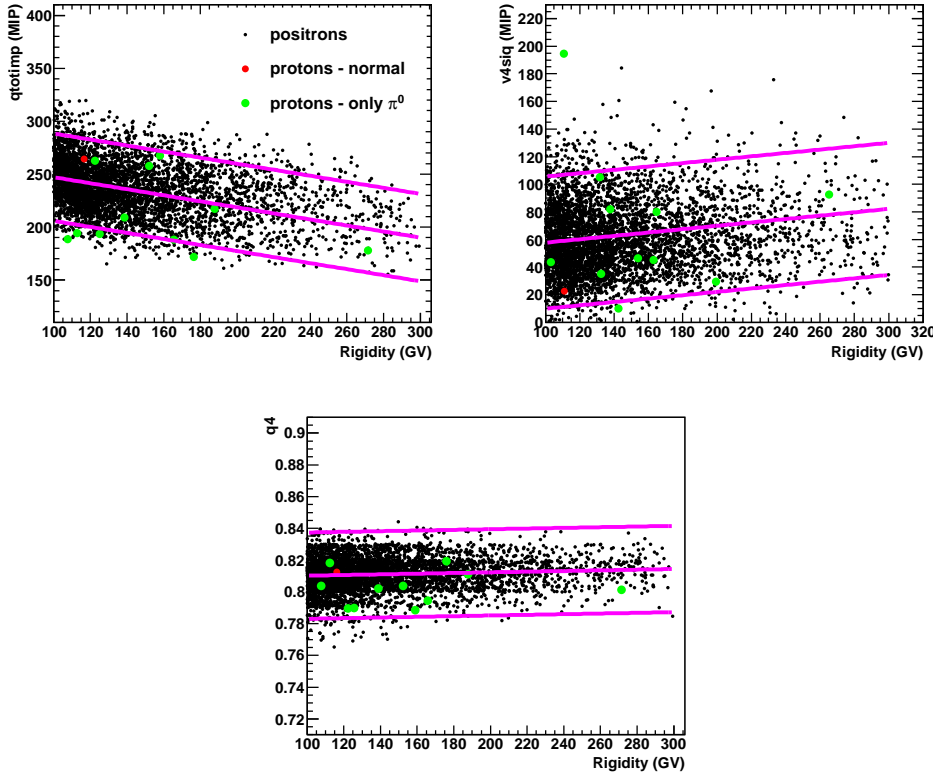


Figure 4.19. Distribution of shower profile variables as function of rigidity for simulated positrons (black points), protons *normal case* (red points) and *only- π^0* case (green points); the purple lines show the mean *variable* and *variable* $\pm 3 \cdot \sigma_{variable}$; simulations have been produced in the energy range 100 – 300 GeV. Samples have been selected using selections listed in section 4.7 with $\chi^2 < 8$.

Figure 4.20 shows the efficiency of the two selections listed above with $\chi_{cut}^2 = 8$ as a function of χ_{cut}^3 . Some positron selection efficiencies and the corresponding

proton contamination for different values of χ_{cut}^3 are summarized in table 4.6. For instance, a cut $\chi^3 > -10$ selects positrons with an efficiency of 49 % and with a corresponding proton contamination of $1.22 \cdot 10^{-4}$ in both the *normal* and *only- π^0* case. As shown in tables 4.5 and 4.6 (see also figure 4.20) it is impossible to find a compromise between an efficient positron selection efficiency and a proton contamination of the order of 10^{-5} . Thus, proton contamination should be taken into account during the flight data analysis for energies greater than 100 GeV.

The selections described in this section have been then applied to positively and negatively charged particles in flight data in order to estimate the number of positrons and electrons respectively and evaluate the positron fraction. The flight data analysis is described in the following section.

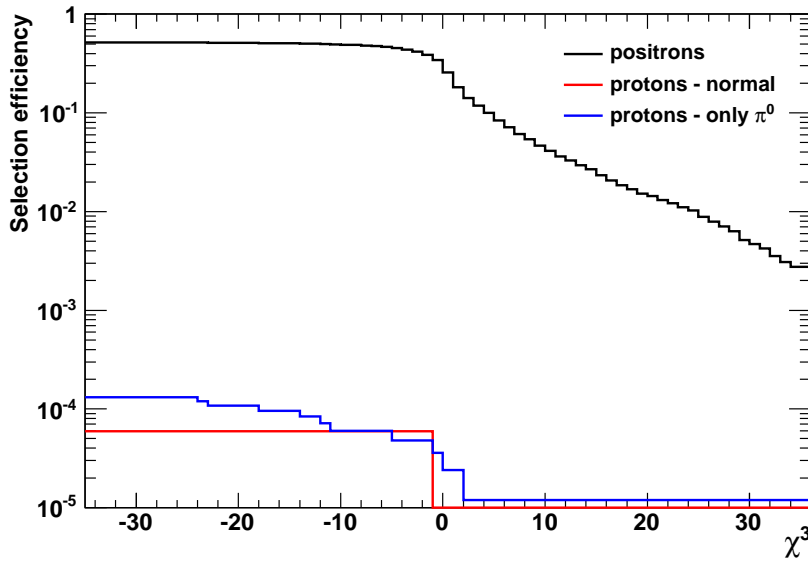


Figure 4.20. Selection efficiency of cuts listed in section 4.7 with $\chi^2 < 8$ (equation 4.7) as a function of cut values on χ^3 (equation 4.8) and for simulations in the energy range 100 – 300 GeV; the positron selection efficiency (black line) is compared to the proton selection efficiency in the *normal case* (red line) and in the *only- π^0* case (blue line).

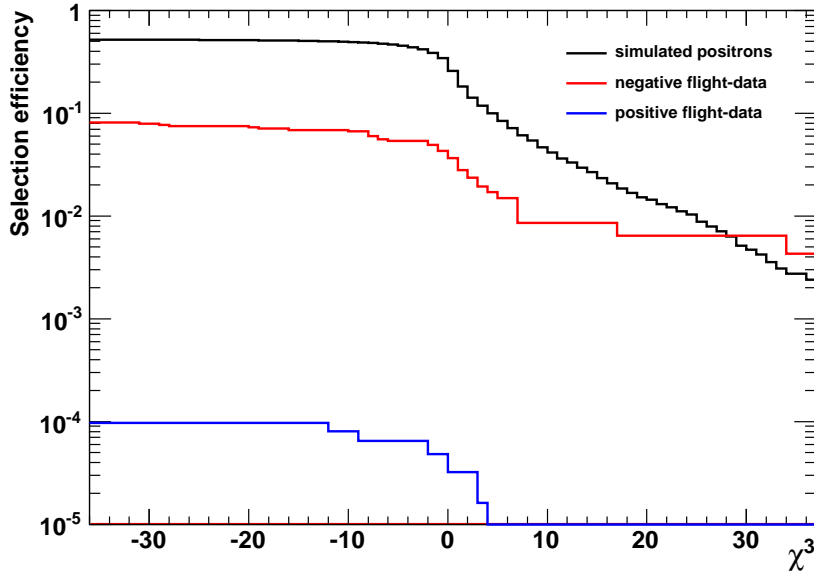


Figure 4.21. Selection efficiency of cuts listed in section 4.8 with $\chi^2 < 8$ (equation 4.7) as a function of cut values on χ^3 (equation 4.8); the selection efficiency for simulated positrons in the energy range 100 – 300 GeV (black line) is compared to the selection efficiency for negatively (red line) and positively (blue line) charged events in flight data.

<i>Normal case</i>			
χ_{cut}^3	e^+ efficiency	p efficiency	proton contamination
-12	0.500 ± 0.012	$(6.0 \pm 22.3) \cdot 10^{-5}$	$(1.20 \pm 4.46) \cdot 10^{-4}$
-10	0.491 ± 0.012	$(6.0 \pm 22.3) \cdot 10^{-5}$	$(1.22 \pm 4.53) \cdot 10^{-4}$
-8	0.482 ± 0.012	$(6.0 \pm 22.3) \cdot 10^{-5}$	$(1.24 \pm 4.61) \cdot 10^{-4}$
-5	0.454 ± 0.011	$(6.0 \pm 22.3) \cdot 10^{-5}$	$(1.32 \pm 4.91) \cdot 10^{-4}$
-2	0.386 ± 0.011	$(6.0 \pm 22.3) \cdot 10^{-5}$	$(1.55 \pm 5.76) \cdot 10^{-4}$

Table 4.5. Proton selection efficiency and proton contamination for different values of χ_{cut}^3 (equation 4.8) after the selection $\chi^2 < 8$ (equation 4.7). The analysis was performed on 10^5 simulated protons in the *normal case* and in the energy range 100 – 300 GeV. The errors have been evaluated at 90 % confidence level. The number of protons which pass the selections listed in section 4.8 are 17838.

<i>Only-π^0 case</i>			
χ_{cut}^3	e ⁺ efficiency	p efficiency	proton contamination
-12	0.500 ± 0.012	$(7.2 \pm_{4.1}^{7.0}) \cdot 10^{-5}$	$(1.44 \pm_{0.82}^{1.40}) \cdot 10^{-4}$
-10	0.491 ± 0.012	$(6.0 \pm_{3.6}^{6.6}) \cdot 10^{-5}$	$(1.22 \pm_{0.74}^{1.34}) \cdot 10^{-4}$
-8	0.482 ± 0.012	$(6.0 \pm_{3.6}^{6.6}) \cdot 10^{-5}$	$(1.24 \pm_{0.75}^{1.36}) \cdot 10^{-4}$
-5	0.454 ± 0.011	$(4.8 \pm_{3.1}^{6.2}) \cdot 10^{-5}$	$(1.06 \pm_{0.68}^{1.37}) \cdot 10^{-4}$
-2	0.386 ± 0.011	$(4.8 \pm_{3.1}^{6.2}) \cdot 10^{-5}$	$(1.24 \pm_{0.80}^{1.60}) \cdot 10^{-4}$

Table 4.6. Proton selection efficiency and proton contamination for different values of χ_{cut}^3 (equation 4.8) after the selection $\chi^2 < 8$ (equation 4.7). The analysis was performed on $5 \cdot 10^5$ simulated protons in the *only- π^0 case* and in the energy range 100 – 300 GeV. The errors have been evaluated at 90 % confidence level. The number of protons which pass the selections listed in section 4.8 are 89095.

4.9 Positron fraction

The method presented in sections 4.7 and 4.8 and tested on simulations in the energy range 20 – 100 GeV and 100 – 300 GeV respectively has been applied to positively and negatively charged particles in flight data in order to measure the positron fraction. The analysis has been applied to the data set collected between July 2006 and January 2010, consisting of over $2 \cdot 10^9$ triggered events (see section 2.2.1) accumulated during a total acquisition time of ~ 1200 days [38].

The selections listed in section 4.4 have been first used in order to select events with a good reconstructed track and to remove false trigger events. Afterwards, selections listed in section 4.7 have been applied to positively and negatively charged particles in order to select positrons and electrons with a tracker reconstructed rigidity $20 < |R| < 100$ GV. The χ^2 (equation 4.5) has been constructed tuning the shower profile variable mean and standard deviation on the negative flight data distributions. Simulation studies showed that $\chi^2 < \chi_{cut}^2 = 5$ selects positrons with a selection efficiency of ~ 57 % and with a corresponding proton contamination of order of 10^{-5} (see section 4.7.2). Thus, a selection $\chi^2 < 5$ has been used also for the analysis on flight data. The results obtained are listed in table 4.7 and shown in figure 4.24 (green points).

In the same way, selections listed in section 4.8 have been applied to positively and negatively charged particles in order to select positrons and electrons with a tracker reconstructed rigidity $100 < |R| < 300$ GV. Simulation studies above 100 GeV showed that a positron selection efficiency of ~ 50 % can be obtained with a corresponding proton contamination of $\sim 1.2 \cdot 10^{-4}$ in both the *normal* and *only- π^0 case*. Thus, the number of positron and electron events has been initially estimated by applying to positively and negatively charged events respectively the selections listed in section 4.8 with $\chi^2 < 8$ (equation 4.7) and $\chi^3 > -10$ (equation 4.8). The

results of this analysis are summarized in the first three rows of table 4.8 and in figure 4.24 (blue points).

Furthermore, as already mentioned in section 4.8 and shown in tables 4.5 and 4.6, while the positron selection efficiency decreases by varying the cut on the χ^3 variable, the proton contamination remains almost constant within errors and is never below the value of 10^{-4} . Thus, it is important to consider a possible proton contamination in the analysis of positively charged events in flight data.

The number of electron and positron events has been consequently evaluated by applying to negatively and positively charged flight data respectively the selections listed in section 4.8 with $\chi^2 < 8$ (equation 4.7) and for $\chi^3 > \chi_{cut}^3$ (equation 4.8). The resulting positron fraction is shown in figure 4.22. The trend of the positron fraction for different values of χ_{cut}^3 can be explained following the selection efficiency for flight data shown in figure 4.21 (from left to right):

- the positron fraction smoothly increases up to $\chi_{cut}^3 = -13$ because the selection efficiency for positively charged events is constant up to $\chi_{cut}^3 = -13$ and the selection efficiency for negatively charged events decreases smoothly;
- for $-13 < \chi_{cut}^3 < -9$ the positron fraction decreases because the selection efficiency for positively charged events decreases faster than the one for negatively charged events;
- for $-6 < \chi_{cut}^3 < -3$ the positron fraction is constant because the selection efficiency for both positively and negatively charged events is constant;
- the positron fraction rises again for $-3 < \chi_{cut}^3 < 0$ because the selection efficiency for negatively charged events decreases faster than the one for positively charged events;
- the positron fraction drops again at $\chi_{cut}^3 = 0$ because the selection efficiency for positively charged events drops; this last feature is repeated up to $\chi_{cut}^3 = 4$ where the selection efficiency for positively charged events is approximately zero.

If no proton contamination was presented in the positron sample selected from the positively charged flight data, the positron fraction as a function of the cut on χ^3 would have been constant within statistical fluctuations. As it is shown in figure 4.22, this is not the case and the positron fraction is dependent on χ_{cut}^3 . As the value of χ_{cut}^3 increases, the residual proton contamination decreases up to a value of $\chi_{cut}^3 = 4$ where the number of positively charged events selected becomes approximately zero. Thus, a possible proton contamination needs to be evaluated.

Considering only one rigidity interval in the range 100 – 300 GV, the number of positively charged events in flight data selected as positrons through the selections

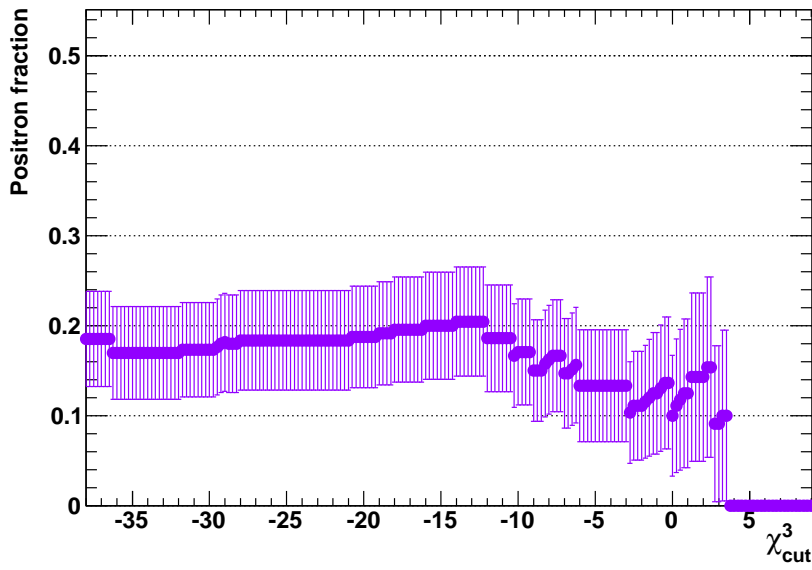


Figure 4.22. Different values of the positron fraction after the selection $\chi^2 < 8$ (equation 4.7) and varying the cut on χ^3 (equation 4.8); the number of positron and electron events has been evaluated by applying the selections respectively on positively and negatively charged events in flight data with a tracker reconstructed rigidity $100 < |R| < 300$ GV.

listed in section 4.8 with $\chi^2 < 8$ (equation 4.7) and $\chi^3 > -10$ (equation 4.8) are (see table 4.8, third row):

$$N_{e^+} = 5 \quad (4.9)$$

The corresponding proton contamination can be estimated using the selection efficiency for simulated protons in the *normal case* (see table 4.5). The proton contamination is then obtained by multiplying the proton selection efficiency (p efficiency) by the total number of positive flight data events ($N_+^{befCALO}$) which pass all the selections before the calorimeter (listed in section 4.4). Assuming that $N_+^{befCALO}$ is dominated by protons:

$$\begin{aligned} N_p^{cont} &= N_+^{befCALO} \cdot \text{p efficiency} \\ &= 61946 \cdot 6.0 \cdot 10^{-5} \\ &= 3.7 \end{aligned} \quad (4.10)$$

Thus, in the evaluation of the positron fraction, the estimated proton contamination has then been considered as a systematic error (see table 4.8, fourth row).

Due to the difficulty in identifying a selection on the χ^3 which gives an efficient positron selection efficiency with the lowest proton contamination, an alternative method has been applied in order to remove possible proton contamination from the final estimated number of positrons. This method is based on the difference in χ^3 distributions for proton and positron events.

The χ^3 distribution for simulated positrons shown in figure 4.23-*top* (black line) was fitted with the following function (red line):

$$F(\chi^3) = p_0 \cdot [e^{p_1 - p_2 \cdot \chi^3} + e^{p_3 - p_4 \cdot \chi^3}] \quad (4.11)$$

After that, $F(\chi^3)$ was divided by a factor A so that

$$f(\chi^3) = \frac{F(0)}{A} = 1 \quad (4.12)$$

Therefore, A has been chosen as $A = p_0 \cdot [e^{p_1} + e^{p_3}]$, and the function $f(\chi^3)$ becomes (green line):

$$f(\chi^3) = \frac{p_0 \cdot [e^{p_1 - p_2 \cdot \chi^3} + e^{p_3 - p_4 \cdot \chi^3}]}{p_0 \cdot [e^{p_1} + e^{p_3}]} \quad (4.13)$$

Function 4.13 has been evaluated for each value of χ^3 for negatively and positively charged events (figure 4.23-*bottom*) selected by the criteria listed in section 4.8 with $\chi^2 < 8$ (equation 4.7). The number of electrons has been selected by applying the criteria listed in section 4.8 with $\chi^2 < 8$, while the number of positrons has been estimated using

$$N_{e^+} = \frac{\sum_{i=1}^p f[\chi^3(i)]}{\sum_{i=1}^n f[\chi^3(i)]} \cdot n = 6.1 \quad (4.14)$$

where $n = 38$ and $p = 6$ are respectively the total number of negatively and positively charged events selected through the criteria listed in section 4.8, i.e. selections

based on $qcore/ncore$ and $\chi^2 < 8$. This method allows the proton contamination to be reduced by weighting more the positron-like events with respect to the proton ones. The results obtained in this case are listed in the last row of table 4.8 and shown in figure 4.24 (purple star).

Rigidity (GV)	N_{e^+}	N_{e^-}	e^- selection efficiency	$N_{e^+} / (N_{e^+} + N_{e^-})$
28 – 42	47	587	38.9 %	0.074 ± 0.017
42 – 65	11	148	23.1 %	0.069 ± 0.030
65 – 100	3	21	7.5 %	$0.125^{+0.177}_{-0.087}$

Table 4.7. Number of positron and electron events selected in three different rigidity intervals within 20 – 100 GV through the selections listed in section 4.7 with $\chi^2 < 5$. The selection efficiency for the three rigidity intervals is also reported. The last column shows the corresponding positron fraction. The errors have been evaluated at 90 % confidence level.

Rigidity (GV)	N_{e^+}	N_{e^-}	e^- selection efficiency	$N_{e^+} / (N_{e^+} + N_{e^-})$
100 – 200	4	30	10.6 %	$0.118^{+0.137}_{-0.074}$
200 – 300	1	1	0.5 %	$0.500^{+1.322}_{-0.336}$
100 – 300	5	31	6.6 %	$0.139^{+0.136}_{-0.080} (stat.)$
100 – 300	5	31	6.6 %	$0.139^{+0.136}_{-0.120} (stat.+syst.)$
100 – 300	$6.1^{+6.9}_{-4.9}$	38	8.1 %	$0.138^{+0.138}_{-0.101}$

Table 4.8. Number of positron and electron events selected by the criteria listed in section 4.8 with $\chi^2 < 8$ (equation 4.7) and $\chi^3 > -10$ (equation 4.8), considering two rigidity intervals or only one rigidity interval (first four rows). The errors of the positron fraction in the fourth row have been evaluated considering a proton contamination in the number of estimated positron events; the method is described further in section 4.9. The number of positron and electron events in the last row have been evaluated following the method also described in section 4.9 (see also figure 4.23). The errors have been evaluated at 90 % confidence level.

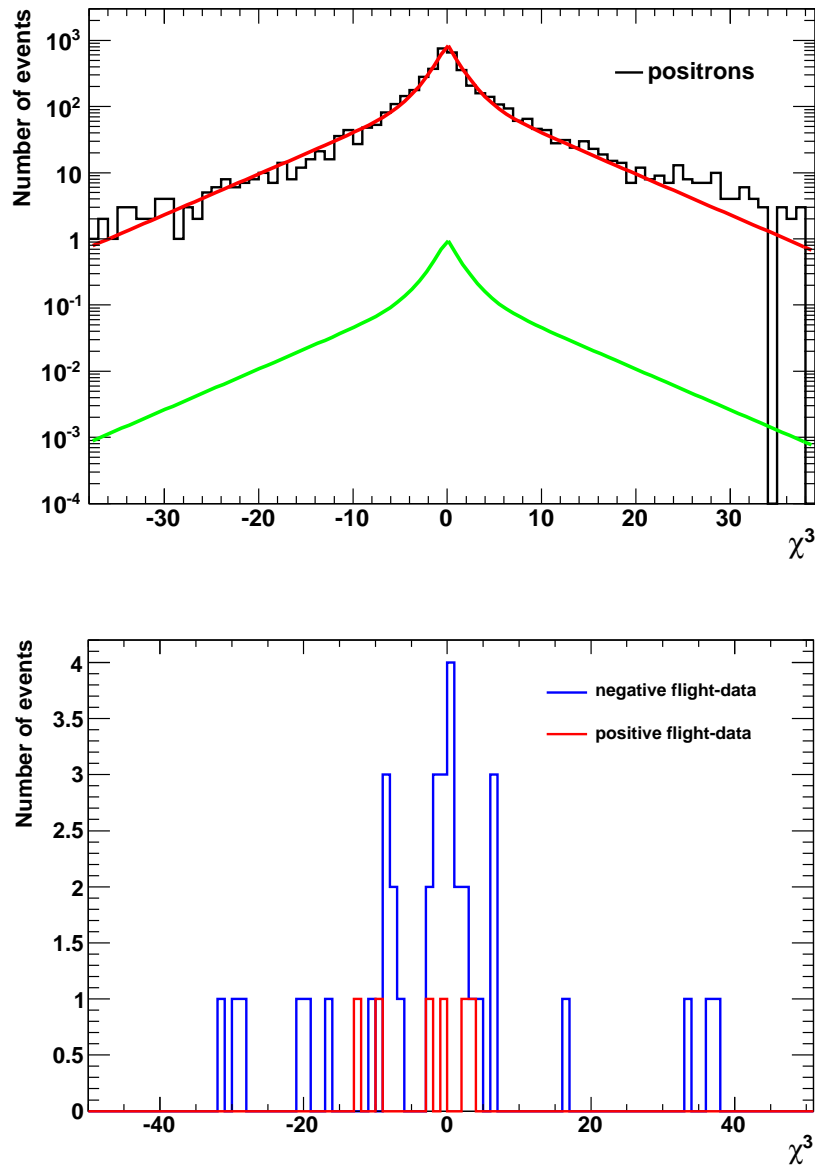


Figure 4.23. *Top:* Distribution of χ^3 (equation 4.8) for simulated positrons in the energy range 100 – 300 GeV; the fitted function (red line) is then normalized (green line) and used to estimate the number of electrons and positrons from flight data. *Bottom:* Distribution of χ^3 (equation 4.8) for flight data with a tracker reconstructed rigidity $100 < |R| < 300$ GV.

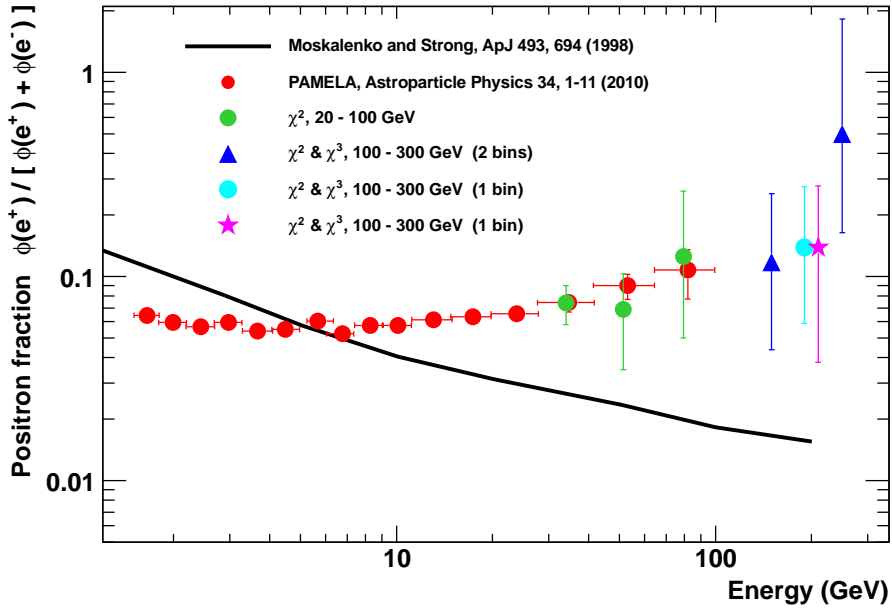


Figure 4.24. Positron fraction values evaluated following the analysis described in this section and summarized in tables 4.7 and 4.8. The analysis has been performed in the energy range 20 – 100 GeV (green points) and in the energy range 100 – 300 GeV considering two intervals (blue triangles) or only one interval (light blue point); the light blue point refers to the values in the third row of table 4.8 (statistical errors). The result indicated by the purple star refers to the values in the last row of table 4.8. Note that values indicated by the light blue point and by the purple star refer to an energy of 200 GeV but are displaced for clarity. The PAMELA positron fraction published in [66] is also shown (red points) together with the theoretical fraction for pure secondary positron production (black line) [32].

4.10 Conclusions

The aim of the analysis presented in this chapter was to study the electromagnetic component inside hadronic cascades, usually initiated by neutral pions during hadronic interactions in the calorimeter. The analysis was performed on simulated events generated by using a Monte Carlo program developed by the PAMELA Collaboration and based on the GEANT 3.21 code. Furthermore, the simulation code was modified in order to artificially increase the number of π^0 in hadronic showers and study the consequences for positron identification. The simulated event samples produced are listed in table 4.1.

The first part of the analysis consisted in evaluating the neutral pion contamination in the positron selection when following the approach used to evaluate the positron fraction published by the PAMELA Collaboration in Nature journal [31] (see section 4.5). The results show that this approach selects a mixture of two distributions which is still correct even when the number of π^0 in hadronic showers is artificially boosted (*only- π^0 case* simulations). The positron fraction evaluated considering this artificial case is in good agreement with the positron fraction published in Nature [31]. Thus, it is unlikely that the rise in the PAMELA positron fraction for energies greater than 10 GeV is due to π^0 contamination of hadronic showers.

As shown in section 4.5, the method followed to evaluate the positron fraction published in [31] starts being less efficient at energies around 100 GeV. In order to extend the positron fraction up to ~ 300 GeV, a new approach based on a combination of shower profile variables in the calorimeter has been studied. This new method has been initially tested in the energy range 20 – 100 GeV and then applied up to a maximum energy of 300 GeV.

The analysis results in the energy range 20 – 100 GeV can be summarized as follows:

- simulation studies showed that this new method allows a positron selection efficiency of $\sim 57\%$ to be obtained with a corresponding proton contamination of order of 10^{-5} (see table 4.4);
- the same selections studied on simulations have been then applied to positively and negatively charged events in flight data with a tracker reconstructed rigidity $20 < |R| < 100$ GV; the results obtained are listed in table 4.7;
- the corresponding positron fraction is shown in figure 4.24 (green points) and is compatible within errors with the positron fraction published in [66] (red points). Note that the positron fraction published in [66] is updated with more statistics compare to the positron fraction published in Nature [31].

The analysis results in the energy range 100 – 300 GeV can be summarized as follows:

- simulation studies showed that this new method allows a positron selection efficiency of $\sim 50\%$ to be obtained, with a corresponding proton contamination of $\sim 1.2 \cdot 10^{-4}$ (see table 4.6);

- the selections applied to simulated data have also been applied to positively and negatively charged events in flight data with a tracker reconstructed rigidity $100 < |R| < 300$ GV; the results obtained are listed in table 4.8;
- the new positron fraction values are shown in figure 4.24 for two energy intervals (blue triangles) or only one energy interval (light blue point); a method to reduce a possible proton contamination in the positron sample was also used (see section 4.9) and the resulting positron fraction (purple star) is compatible within errors with the results previously described (blue triangles and light blue point).

Chapter 5

Multivariate analysis approach

Above approximately 100 GeV the separation between electromagnetic and hadronic events becomes more difficult. The maximum longitudinal development of electromagnetic showers has a logarithmic dependence of the particle initial energy (see section 3.1.1) thus electromagnetic showers start deeper in the calorimeter with consequent energy leakage. The number of secondary particles produced increases directly with energy and electromagnetic showers also broaden (see section 3.1). Furthermore, the number of neutral pions produced in hadronic showers increases with energy and as a consequence the electromagnetic contamination enhances (see sections 3.2 and 3.3).

In order to improve positron selection for energies greater than 100 GeV, a new approach based on shower profile variables in the calorimeter was studied and tested on simulations in two different energy ranges, 20 – 100 GeV and 100 – 300 GeV (see sections 4.7 and 4.8). The method was then applied to flight data in order to reproduce the positron fraction (see section 4.9). As a cross-check to the results obtained with this method, a multivariate approach has also been applied to flight data in order to estimate the number of electron and positron events.

In this chapter the multivariate approach used in the flight data analysis at energies greater than 100 GeV is described. The estimation of the number of electron and positron events using a bootstrap technique is also presented. The resulting positron fraction is presented and compared to the one evaluated in section 4.9.

5.1 The Toolkit for Multivariate Analysis

The Toolkit for Multivariate Analysis (TMVA) [78] is a ROOT [79] environment for the processing, evaluation and application of different multivariate methods. A typical TMVA classification analysis consists of two independent phases: *training*

and *application*. During the training phase variables are passed as input to different multivariate methods. In the application phase the results obtained from the training are then applied to the classification problem they have been trained for.

The training phase is performed via a *Factory* object which permits the training and test data sample to be specified, to define the set of input variables and to book the multivariate methods. The results of this phase are written in files, so called *weights*, for each multivariate method.

The application of the training results to a data set is governed by a *Reader* object. The same variables defined in the training phase must be passed as argument to the *Reader* object, as well as the multivariate methods with the corresponding weights. For each data set event the input variables are evaluated together with the multivariate response values.

The main risk of using a multivariate approach is the so called *overtraining*. Overtraining happens if the classifier overfits data, so it looks at very special features of the training sample. For example, if too many input variables are associated to too few events, these are considered as representative of a bigger sample giving a result that could be biased. In order to avoid overtraining, the input events are usually copied and split into one training and one test sample, and then the performance results between the two samples are compared. This guarantees a statistically independent evaluation of the neural network. In the TMVA environment, if it is not specified by the user, the signal and background samples are automatically split into two halves, one for the training and one for the test sample [78].

For the specific classification problem presented by this analysis, the MultiLayer Perceptron (MLP) neural network has been chosen. Shower profile variables in the calorimeter, previously used for the χ^2 method in the energy range 100 – 300 GeV and described in section 4.8, have been used as input variables for the multivariate approach. The MLP method has been trained on the simulated positron sample (*signal*) and on the simulated proton sample in the *only- π^0 case* (*background*). The resulting *weights* have been then applied to positively and negatively charged events in flight data in order to estimate the number of positrons and electrons and evaluate the positron fraction at energies greater than 100 GeV.

The leading idea is to force the neural network to separate between electromagnetic and hadronic events even in the case where the number of neutral pions is artificially boosted and, as a consequence, a larger contamination of hadronic showers is expected.

It is important to note that, in addition to the MLP neural network, other methods have been tested, like for instance the k-nearest neighbour algorithm (k-NN). The resulting separation between positron and proton events was not competitive with MLP and these methods are not described further in this thesis.

5.2 The MultiLayers Perceptron neural network

Artificial neural networks are a branch of artificial intelligence. The general structure is formed by a simulated set of interconnected nodes, or neurons, with each

node producing a certain response at a given set of input signals. A neural network can therefore be seen as a map from a space of input variables x_n to a space of output variables y_m . In case of a signal-versus-background discrimination problem, the space of output variables is a one dimensional space. The mapping is nonlinear if at least one neuron has a nonlinear response to its input.

The MultiLayer Perceptrons (MLP) is a particular type of artificial neural network where connections between neurons do not form a cycle and thus information always moves in one direction. In general, the architecture of a multilayer perceptron consists of several layers of neurons with each layer fully connected to the next one. A neural network with n neurons can have n^2 directional connections, thus having a high complexity level. In the MLP neural network the complexity is reduced by organising the neurons in layers and only allowing direct connections from a given layer to the following one. This implies a direction of information processing, hence the multilayer perceptron is also known as a *feedforward* neural network. Figure 5.1 shows a sketch of the MLP neural network architecture. The first layer of a multilayer perceptron is the *input layer* and the last one is the *output layer*. All other layers are *hidden*. Considering for instance a classification problem with n input variables, the input layers consist of n neurons that hold the input values $\{x_1, \dots, x_n\}$, and the output layer consists of one neuron that holds as output variable the neural network estimator y_{ANN} . Each node of the network is a processing element with a nonlinear activation function, thus creating a nonlinear mapping between an input and an output signal. The output of a node is scaled by the connecting weight w_i and sent forward to be an input to the nodes in the next layer of the network.

The difference between the multilayer and a normal perceptron is that in the MLP case each neuron uses a nonlinear activation function which was developed to model the frequency of action potentials of biological neurons in the brain. This function is modeled in several ways, but must always be normalizable and differentiable.

The MLP neural network uses a *back propagation* technique for the training process. In this technique the output for every input event is known. During this process the network is supplied with N training events and n input variables $\{x_1, \dots, x_n\}$ are associated to each of these N events. For each training event i the neural network output y_{ANN}^i is computed and compared to the desired output y_i [78].

5.3 Analysis in the energy range 100 – 300 GeV

As already mentioned at the beginning of this chapter, a neural network approach has been used as a cross-check for the results obtained from the χ^2 method described in section 4.8. Thus, the MLP method has been trained using the same shower profile variables studied for the χ^2 method in the energy range 100 – 300 GeV. The training has been done on a *signal* sample and on a *background* sample, in the energy range 100 – 300 GeV. The *signal* sample comprises simulated positrons

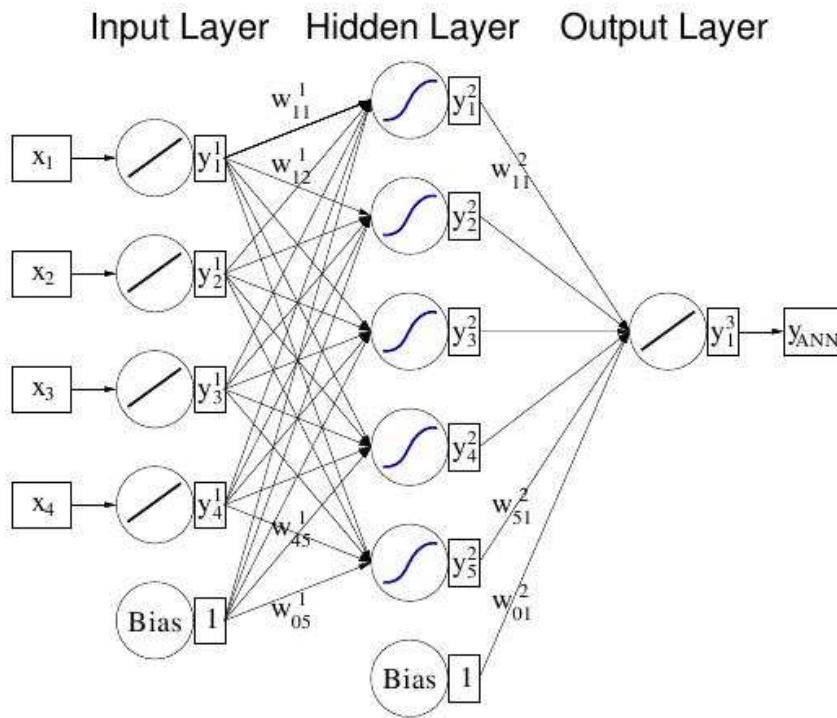


Figure 5.1. Sketch of the MLP neural network architecture. For a classification problem with n input variables, the input layers consists of n neurons that hold the input values $\{x_1, \dots, x_n\}$, and the output layer consists of one neuron that holds as output variable the neural network estimator y_{ANN} ; the output of each node is scaled by the connecting weight w_i and sent forward to be an input to the nodes in the next layer of the network [78].

while the *background* sample comprises simulated protons in the *only- π^0* case. The two samples have been first selected by the cuts listed in section 4.4 and the cut

$$q_{core}/n_{core} > \overline{q_{core}/n_{core}} - 3 \cdot \sigma_{q_{core}/n_{core}} \quad (5.1)$$

in order to reduce the huge proton background. The resulting *weights* obtained from the training process have then been applied to simulated positrons and to simulated protons in the *normal case* in order to obtain an efficient separation between positron and proton events in the real case at energies above 100 GeV. Results of the neural network for simulated samples are shown in figure 5.2. As shown in figure 5.2, the MLP method assigns the value -1 to hadronic events (simulated protons, red line) and the value 1 to electromagnetic events (simulated positrons, black line). The results for simulated positrons and protons in the *normal case* are also shown in figure 5.3 (first and third panel, starting from the top).

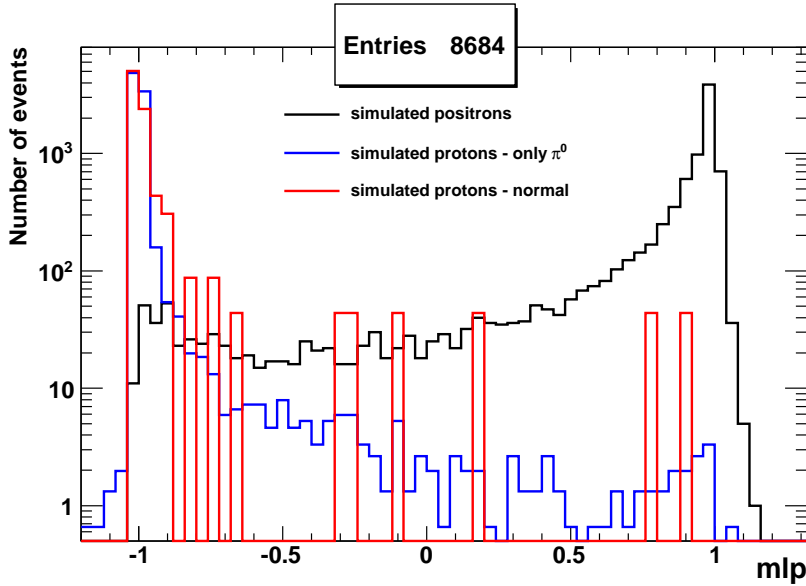


Figure 5.2. Results of the MLP neural network on simulated samples in the energy range 100 – 300 GeV. The *signal* sample is constituted by simulated positrons (black line) while the *background* sample is constituted by simulated protons in the *normal case* (red line) or in the *only- π^0* case (blue line); simulated protons have been normalized to simulated positrons.

The same *weights* have also been applied to negatively and positively charged events in flight data in order to estimate the number of electrons and positrons respectively. The second panel of figure 5.3 shows results of the MLP method for

negatively charged events (violet points). The distribution has a peak around 1 thus indicating that negatively charged events in flight data are dominated by electrons. Furthermore, the distribution for negative flight data has been fitted using the distribution for simulated positrons (first panel) with the normalization factor left as free parameter. The result of the fit (black line) gives an estimation of the number of electrons in flight data. The MLP distribution for negatively charged events shows also a peak around -1 . These events can be associated mainly to spillover protons (see section 2.1.2) which dominate the negatively charged part of hadronic events at energies above 100 GeV. A small fraction of these events are also antiprotons since the antiproton-to-electron flux ratio is of the order of 10^{-3} .

The bottom panel of figure 5.3 shows results of the MLP method for positively charged events (blue points). The positive flight data distribution is instead dominated by a peak around -1 associated to proton events and a peak around 1 associated to positron events. Thus, in this case the distribution has been fitted with a sum of the distribution for simulated positrons (black line) and the distribution for protons in the *normal case* (red line), with two normalization factors left as free parameters. The result of the fit (green dashed line) gives an estimation of the number of positrons and protons in flight data.

Both flight data distributions shown in figure 5.3 (second and fourth panel) were fitted in the range $[-1, 1]$. However, the fit does not reproduce the tail of positive flight data distribution for $MLP > 0$. Thus, it is difficult to estimate a possible proton contamination of candidate positron events. One way of improving the fit of positive flight data distribution for $MLP > 0$ is to change the range of the fit. For instance, figure 5.4 (second and fourth panel) shows results of the MLP method by considering a fit in the range $[0, 1]$. Anyway, even in this case, the tail of the distribution for positive flight data for $MLP > 0$ is not well reproduced by the fit.

Another way of estimating the proton contamination is shown in figure 5.5-*top* and consists of the following steps:

- the distribution for positive flight data is fitted in the range $[0, 0.7]$ with a constant function (purple line);
- this constant value is subtracted from the distribution for positive flight data in the range $[-1, 1]$, thus obtaining a new distribution shown in figure 5.5-*bottom*;
- the number of positrons is extrapolated counting the remaining positively charged events in the range $[0.7, 1]$;
- the number of electrons is extrapolated counting the negatively charged events in the range $[0.7, 1]$.

In this case, the number of estimated positrons should not be affected by a possible proton contamination.

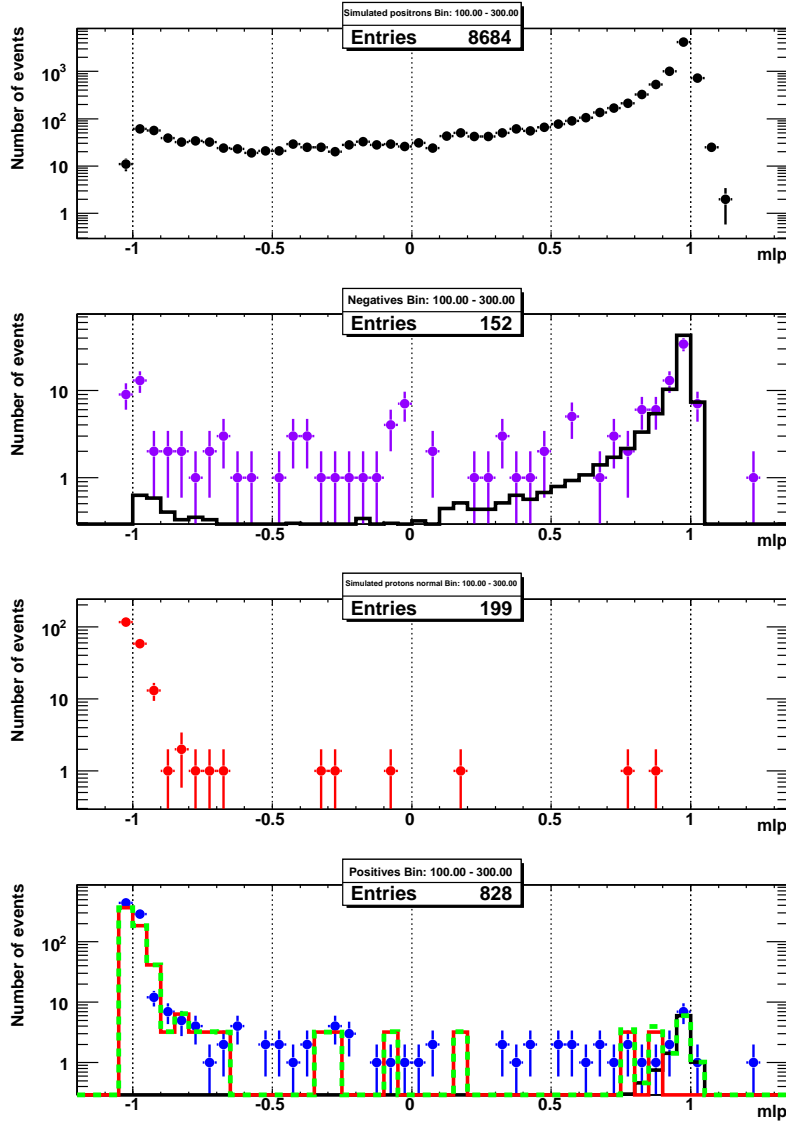


Figure 5.3. Results of the MLP method. *First panel:* MLP distribution for simulated positrons (black points). *Second panel:* MLP distribution for negative flight data (violet points); the data have been fitted in the range $[-1, 1]$ with the distribution for simulated positrons (black line). *Third panel:* MLP distribution for simulated protons (red points). *Fourth panel:* MLP distribution for positive flight data (blue points); the data have been fitted in the range $[-1, 1]$ with a sum (green dashed line) of the distribution for simulated positrons (black line) and the distribution for protons in the *normal case* (red line).

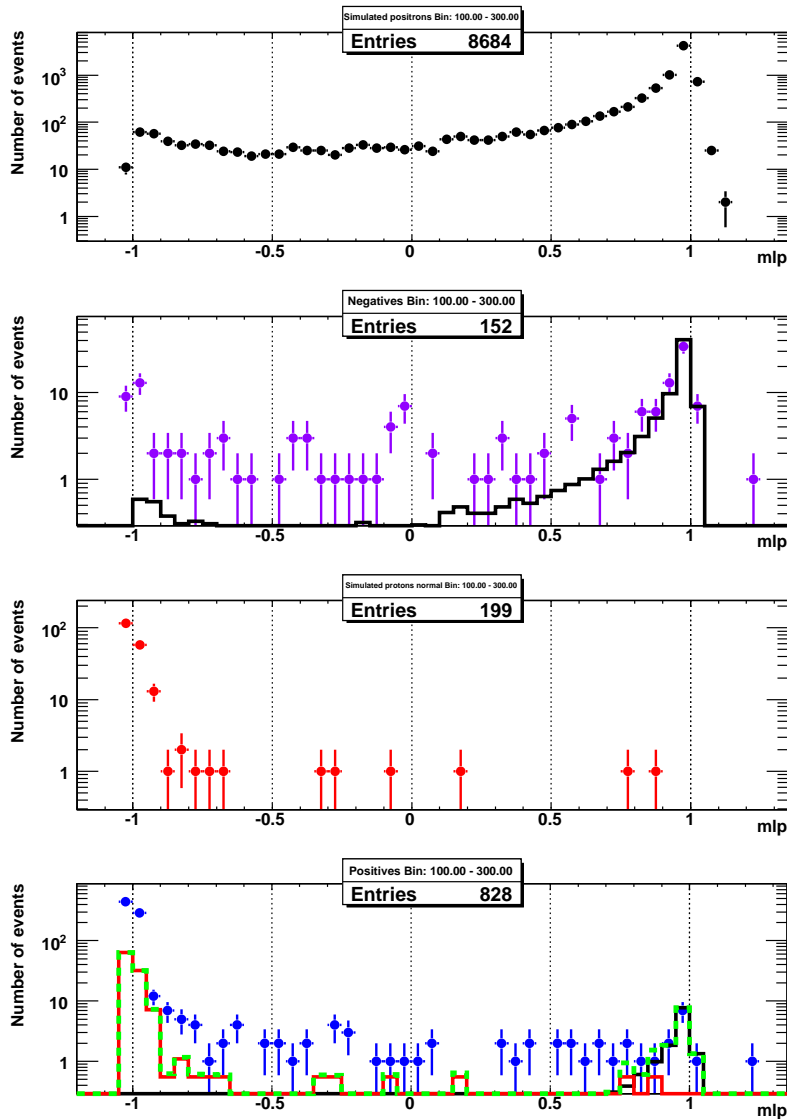


Figure 5.4. Results of the MLP method. *First panel:* MLP distribution for simulated positrons (black points). *Second panel:* MLP distribution for negative flight data (violet points); the data have been fitted in the range $[0, 1]$ with the distribution for simulated positrons (black line). *Third panel:* MLP distribution for simulated protons (red points). *Fourth panel:* MLP distribution for positive flight data (blue points); the data have been fitted in the range $[0, 1]$ with a sum (green dashed line) of the distribution for simulated positrons (black line) and the distribution for protons in the *normal case* (red line).

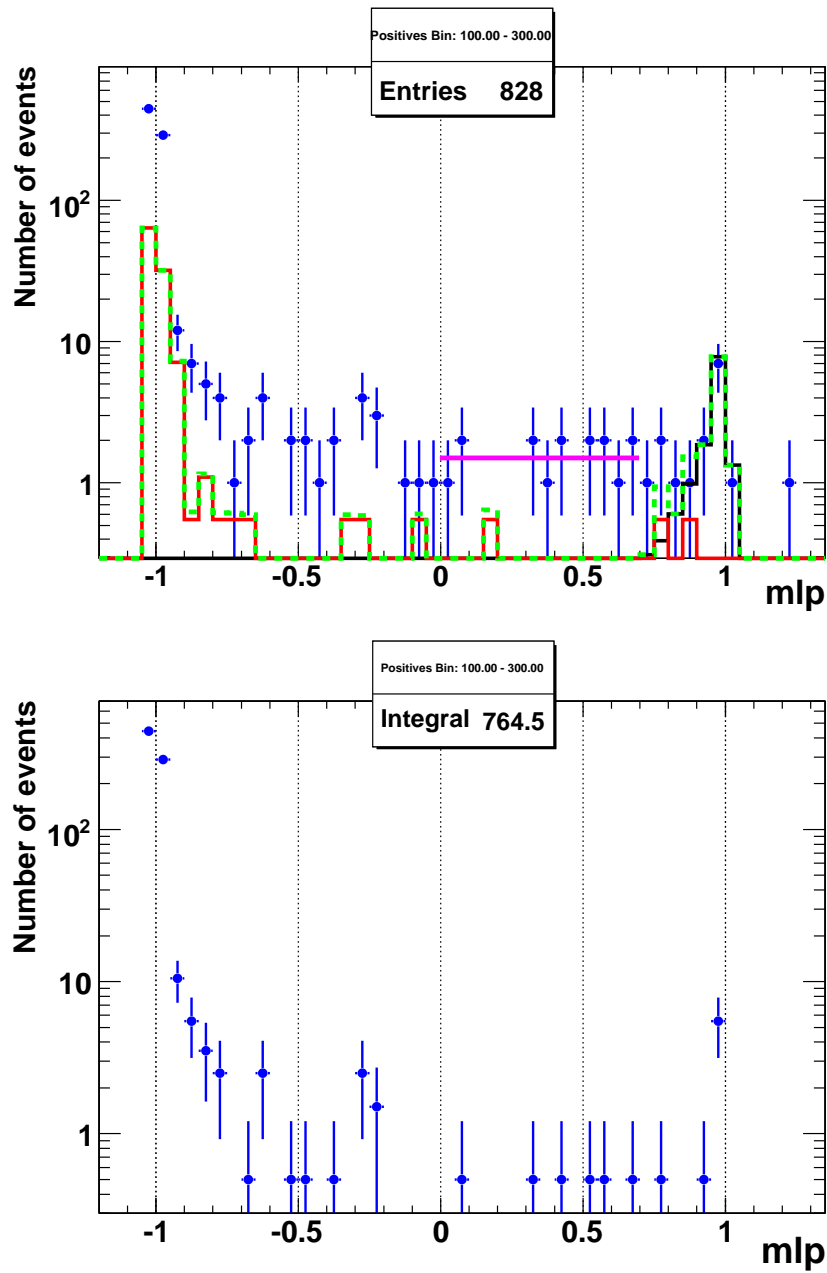


Figure 5.5. *Top:* MLP distribution for positive flight data (blue points); the data have been fitted in the range $[0, 1]$ with a sum (green dashed line) of the distribution for simulated positrons (black line) and the distribution for protons in the *normal case* (red line). The fit in the range $[0, 0.7]$ with a constant function is also shown (purple line). *Bottom:* new MLP distribution for positive flight data in the range $[-1, 1]$ obtained by subtracting the constant value from the distribution shown in the top panel.

5.4 Positron fraction

The multivariate analysis approach described in the previous section was used to estimate the number of electrons and positrons in flight data and consequently evaluate the positron fraction. The analysis has been applied to the same flight data set previously used for the χ^2 method (see section 4.9). The data have been collected between July 2006 and January 2010, and consist of over $2 \cdot 10^9$ triggered events accumulated during a total acquisition time of ~ 1200 days [38].

The number of electrons and positrons was estimated through a bootstrap analysis [76] applied to MLP distributions for flight data, as shown in figures 5.3, 5.4 and 5.5.

The bootstrap method used consists of the following steps:

- considering the original MLP distribution for negatively and positively charged events in flight data (e.g. second and fourth panel from the top of figure 5.3);
- creating a new sample of same size, the so-called *bootstrap sample*, by randomly sampling, with replacement, the values of the original sample;
- repeating this procedure N times;
- fitting each of these N bootstrap samples with the distribution for simulated positrons, in case of negatively charged events, or with a sum of the distribution for simulated positrons and protons in the *normal case*, in case of positively charged events.

The distribution of the number of electrons and positrons obtained from the normalization factor of each fit is in good agreement with a Gaussian distribution. The final numbers of electrons and positrons are then estimated by the mean and the standard deviation of the fitted Gaussian function. Figure 5.6 shows the results of the bootstrap analysis for negatively (*top*) and positively (*bottom*) charged events (see second and fourth panel of figures 5.3), where flight data distributions have been fitted in the range $[-1, 1]$. The fitted Gaussian function is also shown for both distributions (red line). The same procedure has been applied to the flight data distributions shown in figure 5.4. The final results are summarized in the first two rows of table 5.1.

The procedure used to remove a possible proton contamination (see figure 5.5) was also subjected to the bootstrap method described above. Figure 5.7 shows the bootstrap distributions for negatively and positively charged events. The results obtained are listed in the third row of table 5.1.

The corresponding positron fraction has been evaluated in the three different cases previously described. The results shown in the first three rows of table 5.1 are also reported in figure 5.8 (blue square, red triangle and green triangle). These results are also compared to that obtained following the χ^2 method described in section 4.8 and 4.9 and listed in the last two rows of table 5.1 (light blue point and purple star in figure 5.8).

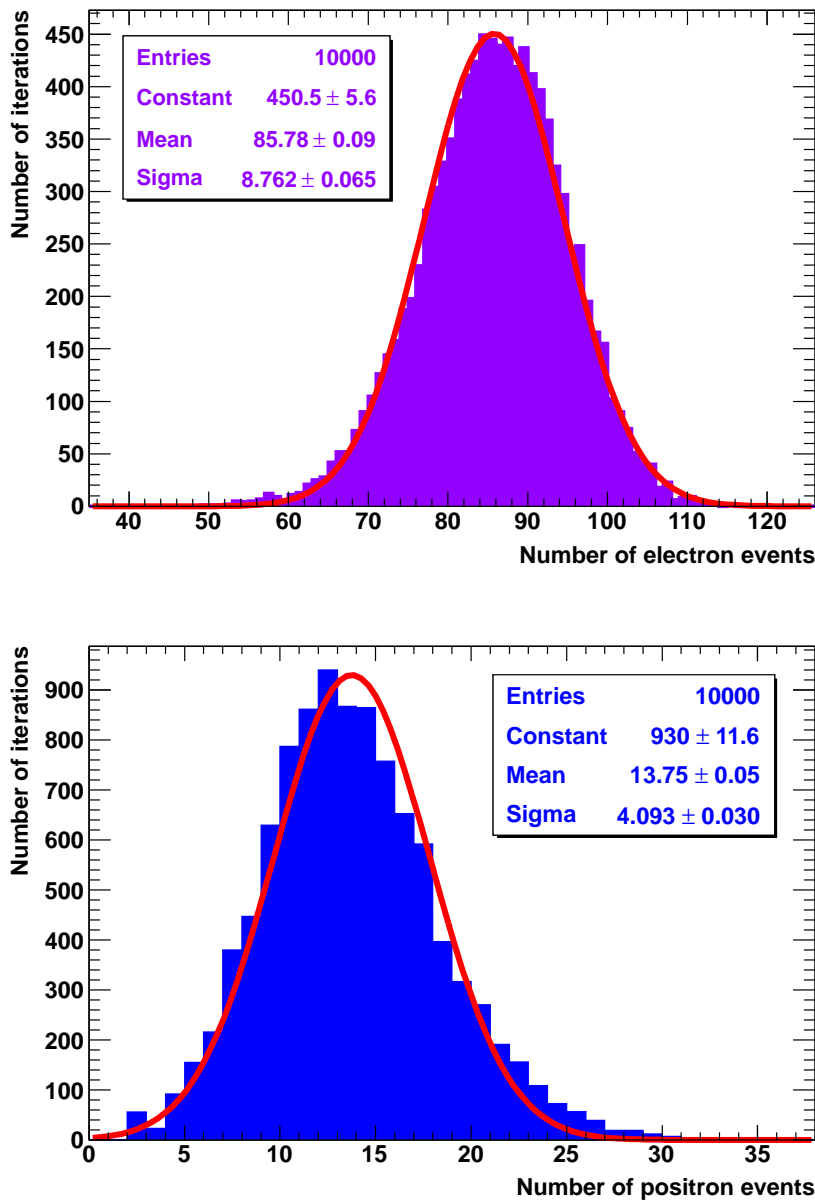


Figure 5.6. Results of the bootstrap analysis for negatively (*top*) and positively (*bottom*) charged events; the analysis refers to the second and fourth panel of figures 5.3, where flight data distributions have been fitted in the range $[-1, 1]$. The number of electrons (*top*) and positrons (*bottom*) were obtained from the normalization factor of each fit and follow a Gaussian distribution; the final number of electrons and positrons listed in table 5.1 (first row) are estimated by using the mean and the standard deviation obtained from a Gaussian fit of these bootstrap distributions (red line).

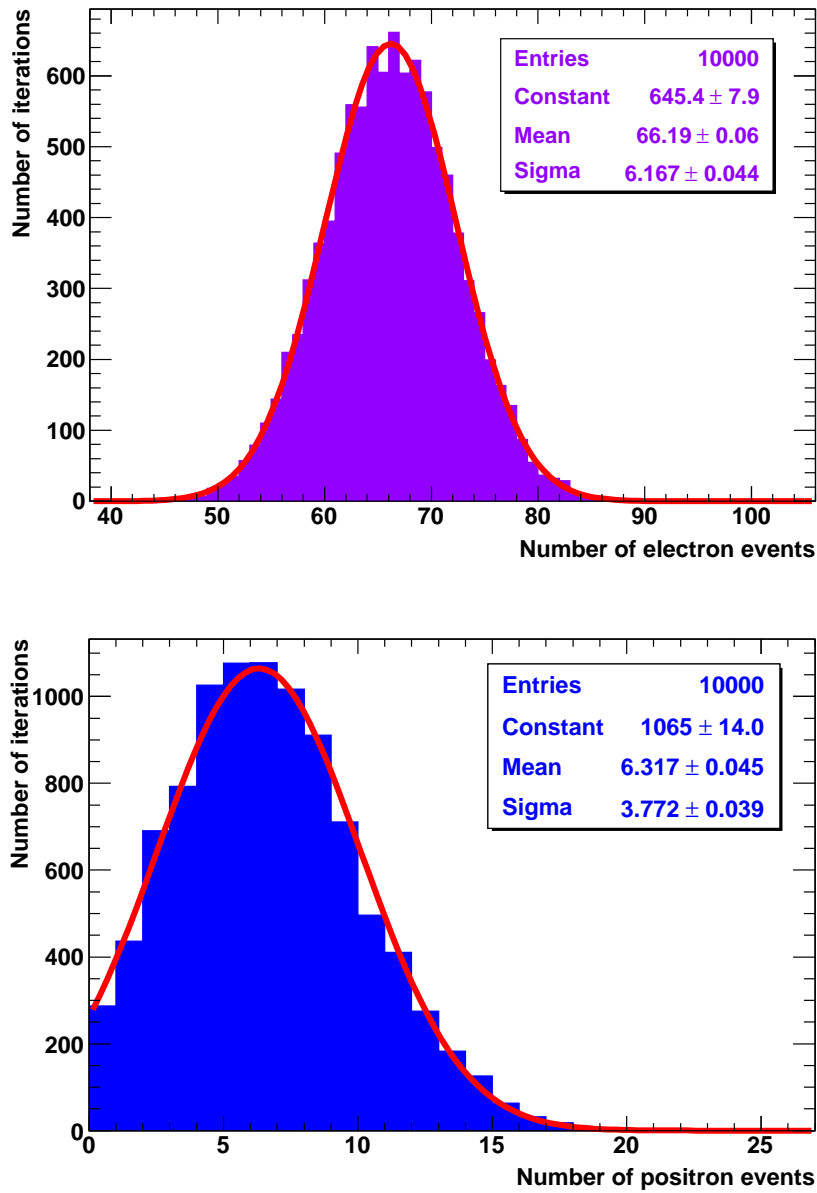


Figure 5.7. Results of the bootstrap analysis for negatively (*top*) and positively (*bottom*) charged events; the analysis refers to figure 5.5. The number of electrons (*top*) and positrons (*bottom*) follow a Gaussian distribution; they were obtained counting the negatively and the positively charged events in the MLP range [0.7 , 1] respectively. The final number of electrons and positrons listed in table 5.1 (last row) are estimated by using the mean and the standard deviation obtained from a Gaussian fit of these bootstrap distributions (red line).

Fit range	N_{e^+}	N_{e^-}	$N_{e^+} / (N_{e^+} + N_{e^-})$
$[-1, 1]$	13.7 ± 4.1	85.8 ± 8.8	0.138 ± 0.037
$[0, 1]$	16.2 ± 4.7	81.4 ± 8.5	0.166 ± 0.043
$[0, 0.7]$ with constant	6.3 ± 3.7	66.2 ± 6.2	0.087 ± 0.047
χ^2 and χ^3 method	5	31	$0.139 \begin{smallmatrix} + 0.136 \\ - 0.080 \end{smallmatrix} (stat.)$
χ^2 and χ^3 method	$6.1 \begin{smallmatrix} + 6.9 \\ - 4.9 \end{smallmatrix}$	38	$0.138 \begin{smallmatrix} + 0.138 \\ - 0.101 \end{smallmatrix}$

Table 5.1. Number of electron and positron events estimated from a bootstrap analysis applied to MLP distributions for negatively and positively charged events in flight data. The bootstrap procedure is described in this section. Values in the first row refer to figure 5.6; values in the third row refer to figure 5.7. The values in the last two rows refer to results obtained using the method described in section 4.8 and 4.9.

5.5 Conclusions

A multivariate approach based on the MLP method has been applied to flight data in order to estimate the number of electron and positron events. The final estimation, obtained by applying a bootstrap technique, has been used to evaluate the positron fraction. The results of this approach are shown in table 5.1 (first two rows) and in figure 5.8 (blue square and red triangle). Furthermore, a procedure was followed in order to remove a possible proton contamination. The resulting positron fraction (table 5.1, third row) is compatible, within statistical uncertainties, with previous results (figure 5.8, green triangle) The results obtained following a multivariate approach are also in good agreement with the one obtained following the χ^2 method described in sections 4.8 and 4.9.

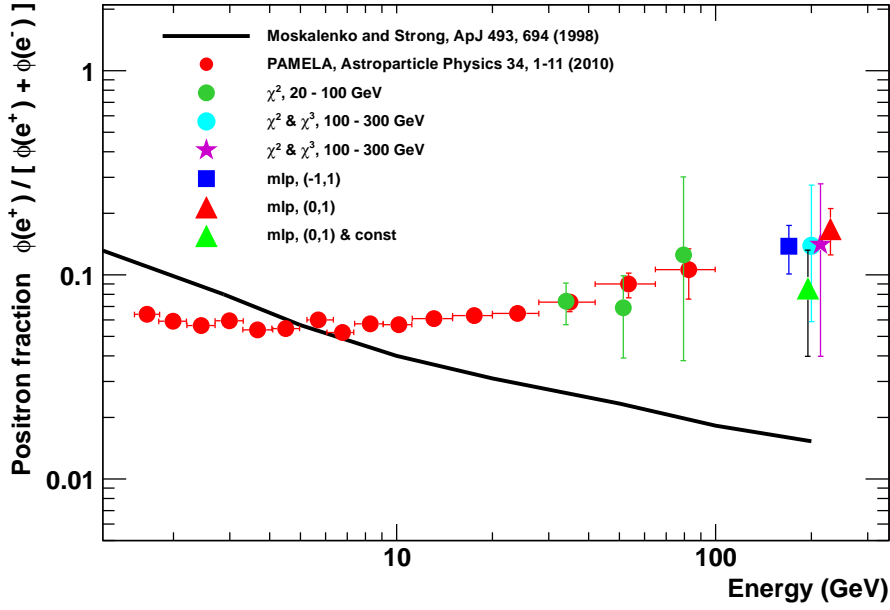


Figure 5.8. Positron fraction values evaluated following a bootstrap technique applied to the multivariate approach described in this section (blue square, red triangle and green triangle); the results are also summarized in table 5.1; the analysis have been done in the energy range 100 – 300 GeV. The results are compared to the ones obtained following the χ^2 method described in section 4.8 and 4.9 (light blue point and purple star). Note that values indicated by the blue square, red triangle, green triangle, light blue point and purple star refer to an energy of 200 GeV but are displaced for clarity. The results evaluated from the χ^2 method in the energy range 20 – 100 GeV are also shown (green points). The PAMELA positron fraction published in [66] is also shown as comparison (red points) together with the theoretical fraction for pure secondary positron production (black line) [32].

Chapter 6

Positron flux

As already discussed in section 1.5, cosmic ray positrons are believed to be mainly secondary particles produced by interactions of primary cosmic ray nuclei with the interstellar matter. However, the positron fraction measured by the PAMELA detector clearly increases with energy above 10 GeV [66], thus indicating a probable primary source of positrons. Moreover, the cosmic ray electron flux measured by PAMELA [38] might require refinements of the standard propagation models and additional sources of cosmic rays. In this context, a measurement of the cosmic ray positron flux above 10 GeV becomes extremely important.

The number of positron events estimated using the selections listed in section 4.4, and the method described in sections 4.7 and 4.8 was used to evaluate the positron flux up to ~ 300 GeV.

In this chapter, the procedure followed to evaluate the flux is described and the resulting positron flux is shown and compared to that evaluated by other experiments.

6.1 Flux evaluation

The flux is defined as the number of detected particles, as a function of the energy, per unit of area and time. The flux can be evaluated as follows:

$$\Phi(E) = \frac{N(E)}{\varepsilon(E)} \cdot \frac{1}{T_{live} \cdot G(E) \cdot \Delta E} \quad (6.1)$$

where E is the energy, $N(E)$ is the number of particles selected, $\varepsilon(E)$ is the total efficiency of all the selections considered, T_{live} is the live time, $G(E)$ is the geometrical factor and ΔE is the width of the energy bin. The calculation of these terms is explained in the following sections.

6.2 The live time

The live time T_{live} is the effective time the instrument is collecting data. On the contrary, the time the instrument is switched off or in a reading out/processing data mode, is called dead time. The live time of the apparatus was evaluated using the trigger system and was cross-checked with the on board time of the CPU allowing the acquisition time ($T_{live} + T_{dead}$) to be determined [67].

The Earth's magnetic field prevents low energy charged particles from reaching the top of the atmosphere. This effect, called geomagnetic cut-off, is maximum at the magnetic equator and minimum at the magnetic poles. Thus, the cut-off rigidity varies as a function of the magnetic latitude, from a maximum value of ~ 15 GV at the equator to a minimum value < 1 GV at the poles. In order to calculate the effective detector live time, it is necessary to evaluate the time spent by the detector in different orbital regions with the corresponding rigidity cut-off. Low energy particles are more affected by such an effect, resulting in a live time which increases as the rigidity increases up to a particle rigidity value of ~ 22 GV where the live time becomes constant. This is clearly visible in figure 6.2 where the live time is shown as a function of the particle rigidity.

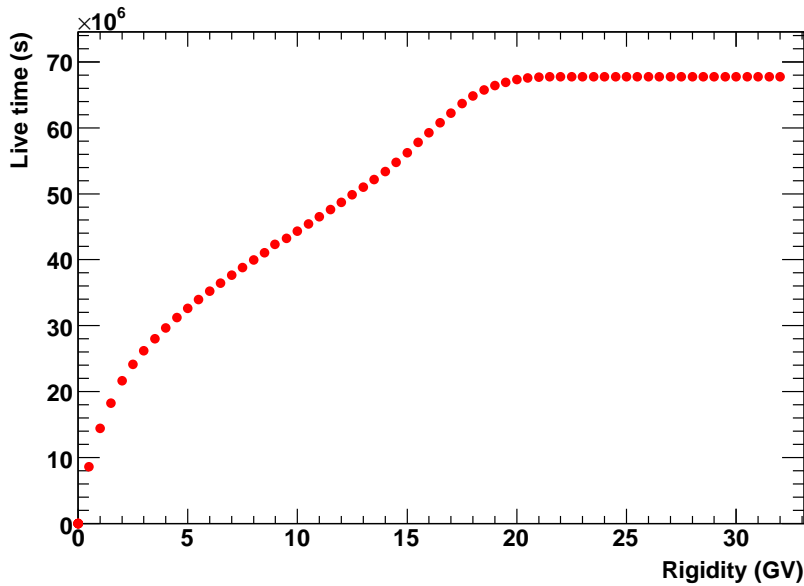


Figure 6.1. The live time T_{live} as a function of the particle rigidity.

6.3 The geometrical factor

The geometrical characteristics of the instrument are important in the flux evaluation. Considering an ideal detector, the counting rate C of the instrument is proportional to the incident intensity I by a factor called *gathering power* Γ :

$$C = \Gamma \cdot I \quad (6.2)$$

The gathering power is defined as follows:

$$\Gamma = \int_{\Omega} d\Omega \int_S d\vec{\sigma} \cdot \hat{r} F(\Omega) \quad (6.3)$$

where, as shown in figure 6.2, $d\Omega$ is an element of the solid angle Ω , S the total area of the detector, $d\vec{\sigma} \cdot \hat{r} = dS_{\perp}$ the effective element of area looking into $d\Omega$ and $F(\Omega)$ the intensity. If the intensity is isotropic, $F(\Omega) = 1$ and the gathering power is called the *geometrical factor* of the instrument. The geometrical factor G depends only on the geometry of the detector and its definition can be derived from equation 6.3 [80]:

$$G = \int_{\Omega} d\Omega \int_S d\vec{\sigma} \cdot \hat{r} = \int_{\Omega} d\Omega \int_S \cos \theta d\sigma \quad (6.4)$$

The geometrical factor is usually derived from equation 6.4 using numerical calculations or Monte Carlo simulations. A detailed study of the PAMELA geometrical factor performed with GEANT3 simulations is reported in [74]. In order to simplify the calculations, the PAMELA geometry was reduced only to those volumes which define the physical acceptance, i.e. the time-of-flight system and the magnetic cavity. These subdetectors have been considered as simple cuboids without any subdivision in paddles or strips. Also, insensitive volumes like boxes, aluminium frames, glue, etc. were not taken into account for calculations of the geometrical factor. The requirements which define the PAMELA acceptance are the following:

- the particle trajectory must cross at least one of the two layers in each plane of the ToF system (S11 or S12, S21 or S22, S31 or S32);
- the particle must cross all the six silicon planes of the tracking system;
- the particle trajectory must be fully contained inside the magnetic cavity, without crossing or touching the walls of the cavity.

Furthermore, the geometrical factor depends on the particle rigidity. As depicted in figure 6.3, low rigidity particles are strongly deflected by the magnetic field towards the cavity walls, thus resulting in a decreasing of the geometrical factor as the particle rigidity decreases. High rigidity particle trajectories are instead approximately straight, thus the geometrical factor assumes an almost constant value. In the analysis presented in this thesis, the geometrical factor was evaluated by defining a fiducial volume inside the $13.1 \text{ cm} \times 16.1 \text{ cm}$ magnetic cavity. Above 1 GV the geometrical factor is approximately constant and has a value of $(19.9 \pm 0.01) \text{ cm}^2 \text{ sr}$.

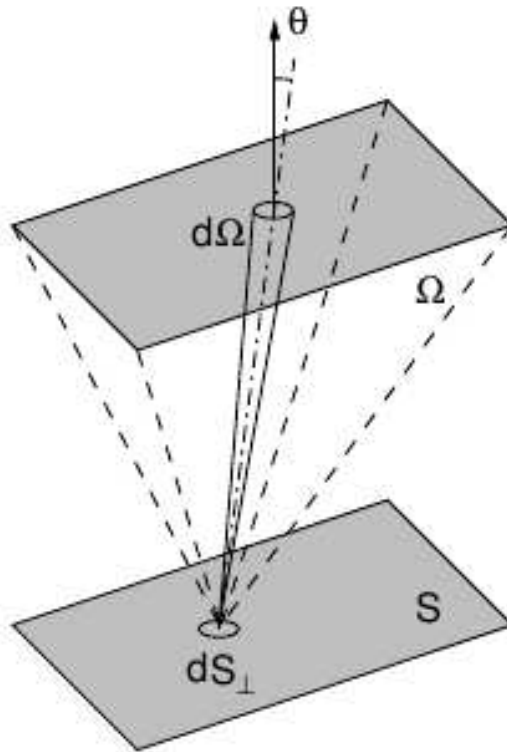


Figure 6.2. Schematic view of the geometrical factor calculation [74].

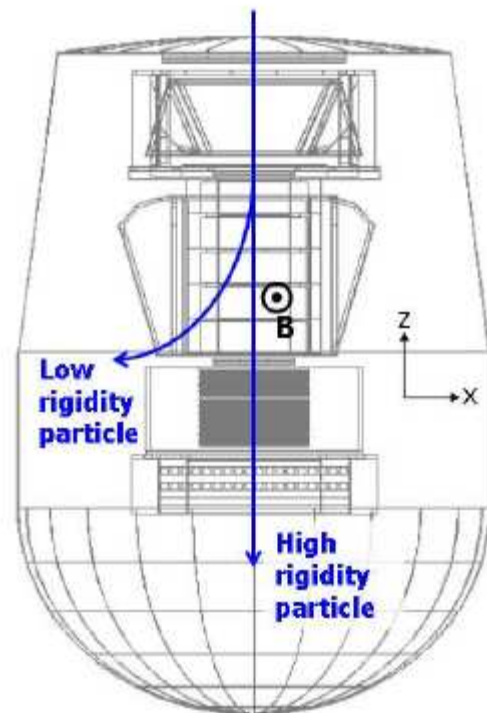


Figure 6.3. Sketch of the PAMELA apparatus with a representation of positive charged particle trajectories inside the magnetic cavity. Low rigidity particles are strongly deflected by the magnetic field resulting in a lower value of the geometrical factor compared to the one for high rigidity particles [74].

6.4 Selection efficiencies

The efficiency for each selection is the probability for an event, in this case a positron, to pass the selection criteria of each detector. The selection efficiencies depend on the particle type and rigidity. In order to evaluate the correct efficiency, a sample of events must be selected independently from the detector on which the selection criteria are applied. Selection efficiencies can be determined both from simulations and flight data. The advantage of using simulations is that a large statistics can be achieved. On the other hand, conditions of the whole apparatus can be slightly different during flight compared to simulations, thus resulting in a different efficiency between simulations and flight data. For this reason, if the statistics is high enough it is more precise to use flight data for the efficiency evaluation.

Since the selections for each single detector are independent, the total efficiency was evaluated as follows:

$$\varepsilon(E) = \varepsilon_{trigger}(E) \cdot \varepsilon_{aboveCalo}(E) \cdot \varepsilon_{calorimeter}(E) \quad (6.5)$$

where

- $\varepsilon_{trigger}(E)$ is the product of the trigger efficiency for each time-of-flight layer required in a particular trigger configuration;
- $\varepsilon_{aboveCalo}(E)$ is the selection efficiency for all requirements applied to the detectors above the calorimeter, i.e. the time-of-flight, the tracker and the anticoincidence system;
- $\varepsilon_{calorimeter}(E)$ is the efficiency for the selections used in the calorimeter.

6.4.1 Trigger efficiency

The total trigger efficiency $\varepsilon_{trigger}(E)$ is the product of the trigger efficiency for each time-of-flight layer required in a particular trigger configuration. Different trigger configurations are used in different orbital regions (see section 2.2.1) [67]. The total trigger efficiency is calculated to be $\varepsilon_{trigger}(E) = 0.999 \pm 0.001$ [81].

6.4.2 Efficiency of selections above the calorimeter

The efficiency $\varepsilon_{aboveCalo}(E)$ is the selection efficiency for all requirements applied to the detectors above the calorimeter, i.e. selections listed in section 4.4. The problem in this calculation is that, in order to evaluate the tracker efficiency it is necessary to select a sample without any requirements on the tracking system. Thus, the information about particle rigidity must be extrapolated from the energy released in the calorimeter. This analysis was applied selecting events from the whole flight data set acquired between July 2006 and January 2010 [38]. Initially, events with a total energy released in the calorimeter larger than 2000 MIP, i.e. $E > 10$ GeV, were selected, allowing non-interacting particles to be rejected. The

shower in the calorimeter was used to reconstruct the event track, backpropagating the shower axis through the tracker and the time-of-flight system. Only events with a reconstructed track which passes through the fiducial acceptance in the tracker cavity and intercepts the ToF planes S1, S2 and S3 have been selected. Furthermore, in the context of the positron analysis, several conditions on the shower characteristics were applied in order to select electromagnetic events, e.g. the fraction of energy along the track (q_{track}/q_{tot}), the dispersion of secondary particles produced in the shower (q_{core}/n_{core}) and the asymmetry of the cascade (*asymmetry*). Then, selections described in section 4.4 have been applied to the selected sample and $\varepsilon_{aboveCalo}(E)$ was consequently evaluated as

$$\varepsilon_{aboveCalo}(E) = \frac{N_{sel}}{N_{tot}}(E) \quad (6.6)$$

where N_{sel} is the number of events which pass conditions listed in section 4.4 and N_{tot} is the total number of events selected reconstructing the track from the calorimeter. Figure 6.4 shows the distribution of the evaluated efficiency as a function of the energy extrapolated from the calorimeter. The distribution has been fitted with the function (violet line)

$$f = p_0 \cdot (1 + p_1 \cdot e^{-p_2 \cdot E}) + p_3 \cdot E \quad (6.7)$$

where E is the energy extrapolated from the calorimeter.

6.4.3 Calorimeter efficiency

The calorimeter efficiency $\varepsilon_{calorimeter}(E)$ is the efficiency for all the selections used in the calorimeter and described in sections 4.7 and 4.8. Also in this case, efficiencies were calculated using the flight data set acquired between July 2006 and January 2010 [38]. Since different selections have been used for the analysis in the energy range 20 – 100 GeV and in the energy range 100 – 300 GeV, the efficiencies have been separately evaluated in the two cases. Calorimeter selection efficiencies were evaluated as follows:

$$\varepsilon_{calorimeter}(E) = \frac{N_{sel}}{N_{tot}}(E) \quad (6.8)$$

where N_{sel} is the number of negatively charged events selected by the method described in sections 4.7 and 4.8, and N_{tot} is the number of negatively charged events selected by the cuts listed in section 4.4. The resulting efficiencies for the four rigidity bins considered are reported in table 6.1.

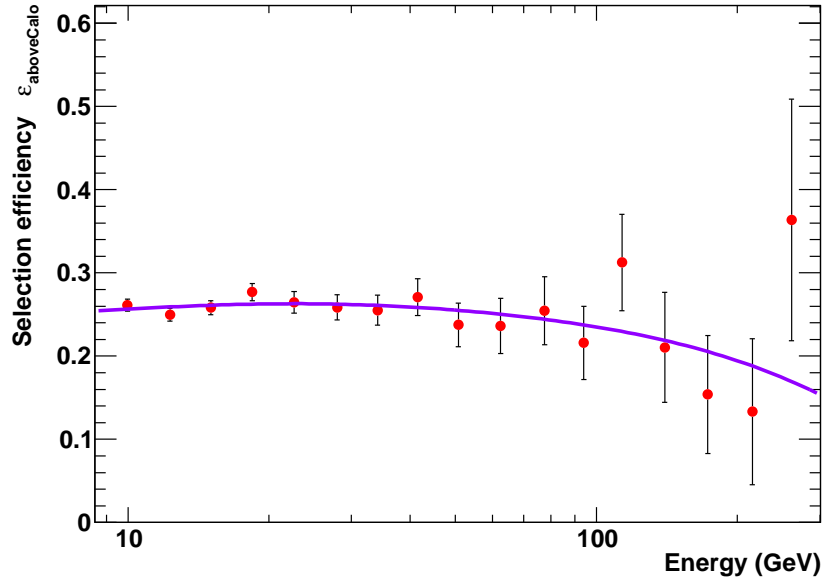


Figure 6.4. Distribution of the efficiency for selections listed in section 4.4 as a function of the energy extrapolated from the calorimeter; the distribution has been fitted with equation 6.7 (violet line).

Rigidity (GV)	calorimeter selection efficiency
28 – 42	0.389 ± 0.019
42 – 65	0.231 ± 0.021
65 – 100	0.075 ± 0.017
100 – 300	0.081 ± 0.014

Table 6.1. Calorimeter selection efficiencies evaluated using equation 6.8; values in the first three rows refer to selections listed in section 4.7; values in the last row refer to selections listed in section 4.8.

6.5 Positron flux

The positron flux has been evaluated using equation 6.1. The number of events $N(E)$ is the number of positron events selected using the requirements described in sections 4.4, 4.7 and 4.8, and previously used to evaluate the positron fraction shown in figure 4.24. The analysis has been performed on the flight data set acquired between July 2006 and January 2010, and consisting of over $2 \cdot 10^9$ triggered events accumulated during a total acquisition time of ~ 1200 days [38]. The other terms of equation 6.1, i.e. the live time, the geometrical factor and the total selection efficiency, have been previously described in this chapter in sections 6.2, 6.3 and 6.4 respectively. The resulting positron flux values are reported in table 6.2 and shown in figure 6.5 (green points). The result is in good agreement, within statistical uncertainties, with the positron flux evaluated by the PAMELA Collaboration (red points) [82], obtained using the number of positron events reported in [66] and the estimated electron flux published in [38]. The positron flux evaluated in this analysis shows evidence for a break in the spectral index around ~ 100 GeV. The resulting rise is in good agreement, within statistical uncertainties, with recent measurements from the Fermi LAT experiment (violet squares) [83]. Previous results from CAPRICE94 [84], HEAT94+95 [85] and AMS-01 [86] are also shown for comparison.

The theoretical trend for pure secondary positron production (see section 1.5), as evaluated by Moskalenko and Strong, is shown in figure 6.5 (black line) [32] but it does not reproduce the spectral break at high energies. In figure 6.6, the positron flux evaluated in this analysis is also compared with the theoretical model proposed by Delahaye et al. [87] (violet lines). This theoretical secondary positron flux is calculated using relativistic treatment of the energy losses (dotted violet line). The dashed violet line is instead estimated considering contributions from supernova remnants and pulsars within 2 kpc and a smooth astrophysical sources distribution beyond. The violet line represents the sum of these two contributions. Both the positron flux estimated in this analysis (green points) and the one evaluated by an independent analysis within the PAMELA Collaboration (red points) [82] are in good agreement, within statistical errors, with the model presented by Delahaye et al. up to ~ 100 GeV.

Rigidity (GV)	positron flux ($\text{s}^{-1} \text{sr}^{-1} \text{m}^{-2} \text{GeV}^2$)
28 – 42	9.99 ± 1.77
42 – 65	8.46 ± 2.69
65 – 100	17.57 ± 10.30
100 – 300	65.67 ± 27.61

Table 6.2. Positron flux values obtained by the procedure described in this section and reported also in figure 6.5 (green points). Positron events in the first three rows refer to selections listed in section 4.7; positron events in the last row refer to selections listed in section 4.8.

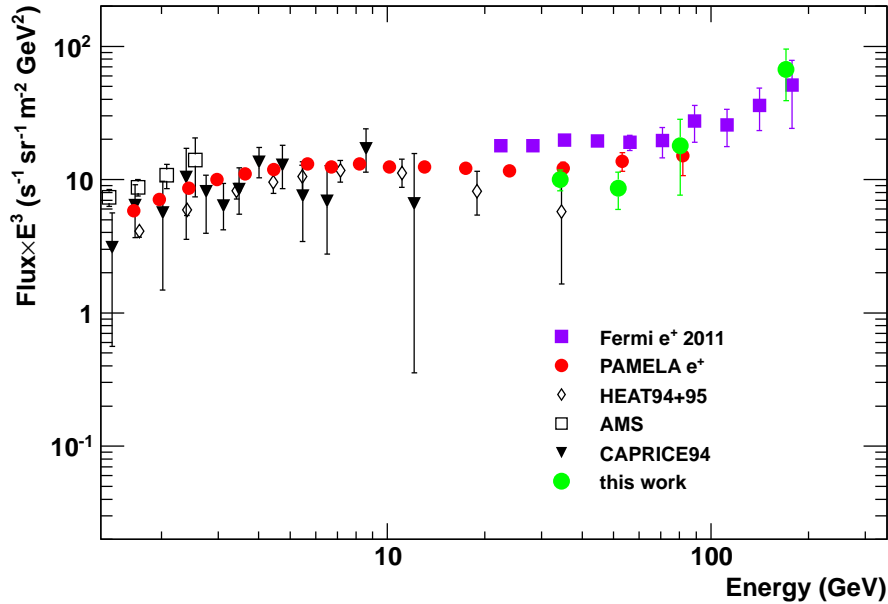


Figure 6.5. Positron flux as a function of the energy evaluated using the procedure described in this section (green points); the values refer to table 6.2. The positron flux is compared to the one evaluated by the PAMELA Collaboration using a different method (red points) [82]. Data from other experiments are also shown as comparison: Fermi LAT (violet squares) [83], HEAT94+95 (open diamonds) [85], AMS-01 (open squares) [86] and CAPRICE94 (black triangles) [84].

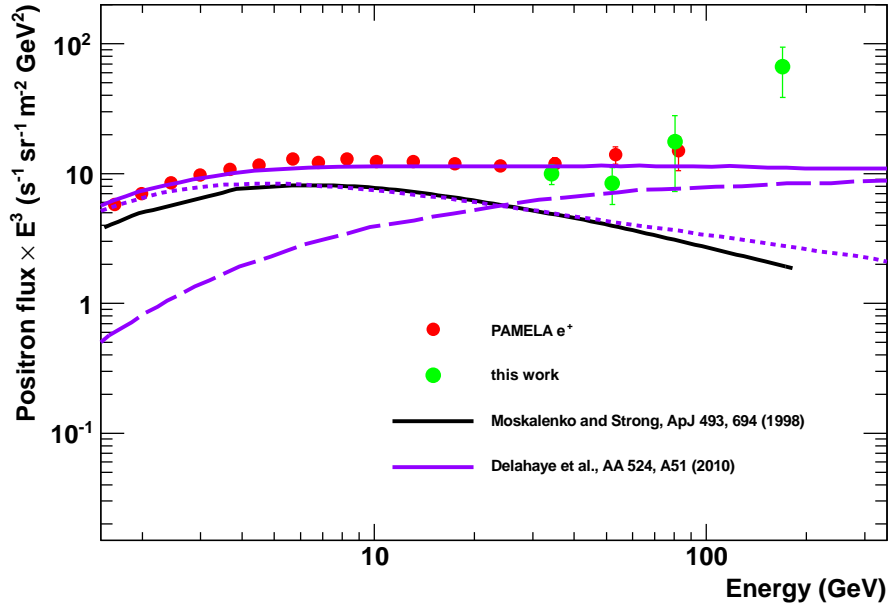


Figure 6.6. Positron flux as a function of the energy evaluated using the procedure described in this section (green points); the values refer to table 6.2. The positron flux is compared to the one evaluated by the PAMELA Collaboration using a different method (red points) [82]. The positron flux is compared to the theoretical trend evaluated by Delahaye et al. (violet line) [87] considering a pure secondary positron production and a primary positron components from pulsars and supernova remnants. The positron flux is also compared to the theoretical flux for pure secondary positron production as evaluated by Moskalenko and Strong (black line) [32].

Chapter 7

Conclusions

Positrons are believed to be mainly secondary particles, produced during interactions of primary cosmic ray nuclei with the interstellar matter. Positrons could be also created as primary particles in high energy astrophysical sources, such as pulsars and supernova remnants, or be produced by dark matter particle annihilations. Since positrons lose energy very efficiently as they propagate they could give useful information about acceleration mechanisms and propagation processes of cosmic rays in the local part of our galaxy. The interest in cosmic ray positron measurements considerably increased in the last years because of new experimental results. The positron fraction measured by the PAMELA detector clearly increases with energy above 10 GeV [66]. This is not in agreement with a pure secondary positron production, thus indicating a probable primary origin of positrons. Moreover, the cosmic ray electron flux measured by PAMELA [38] might also require refinements of the standard propagation models and additional sources of cosmic rays. In this context, a measurement of the positron fraction and of the positron flux up to ~ 300 GeV becomes extremely important.

The analysis described in this thesis is based on positron selections performed using the PAMELA electromagnetic calorimeter. The PAMELA experiment, mounted on board of the Russian Resurs DK1 satellite, was launched on June 15nd 2006 and since then is continuously acquiring data. Since leptons and hadrons interact in different ways, a powerful way to distinguish between these two types of events is to analyse the longitudinal and transverse shower profiles inside the calorimeter. The method followed to identify positron events over a large background of protons is presented in chapter 4. This method has been first tested on simulated positron and proton events produced in two different energy ranges (20 – 100 GeV and 100 – 300 GeV). A possible neutral pion contamination of hadronic showers, which could result in a proton being misidentified as a positron, has also been studied. The same method has been then applied to positively and negatively charged particles in flight data in order to identify positron and electron events respectively. The positron fraction has been consequently evaluated up to ~ 300 GeV and is shown in figure 4.24. As a cross-check of the results obtained with this method, a

multivariate approach has also been applied to flight data in order to estimate the number of positron and electron events at energies greater than 100 GeV (see chapter 5). The resulting positron fraction is shown in figure 5.8 and compared to the one evaluated with the method described in chapter 4 using selection on calorimeter variables. The positron fractions obtained with these two different methods are in good agreement within statistical uncertainties. Furthermore, the positron flux has been evaluated up to ~ 300 GeV using the method described in chapter 4. The resulting positron flux is shown in figures 6.5 and 6.6. The flux evaluated in this analysis is in good agreement, within statistical uncertainties, with the one estimated by the PAMELA Collaboration using a different method [82] and recent measurements from the Fermi LAT experiment [83]. A rise at energies greater than ~ 100 GeV is clearly visible and it is not reproduced by a theoretical trend for pure secondary positron production.

Many theoretical interpretations have been suggested in order to interpret the latest cosmic ray measurements. These interpretations mainly involve primary positron production from astrophysical sources (pulsars and supernova remnants) or from dark matter annihilation processes. New experimental data from the AMS-02 experiment [57] are expected soon. The AMS-02 experiment will provide measurements with a higher maximum energy cut-off compared to PAMELA. Moreover, in order to further extend positron measurements in the TeV scale, the PEBS long-duration electron positron balloon-borne mission has been proposed [58]. New results about positron and electron flux will be interesting in this scenario. The future data, together with the present ones, will probably provide a better understanding of all these open questions.

Acknowledgments

A great adventure is coming to the end and it is time to acknowledge all the persons that have been part of it.

First of all, I want to thank Prof. Mark Pearce to have accepted me as a PhD student in the Particle and Astroparticle Physics group at KTH in 2007 and for all the support in the daily work. Funding received from the Swedish National Space Board for my PhD position is gratefully acknowledged.

I would like to thank all the persons in the PAMELA Collaboration. A special thanks goes to Mirko Boezio for his continuous help during the work at this thesis, and to Francesco Cafagna and Alessandro Bruno for having helped me with GEANT3 simulations, the basis of all this analysis. To Emiliano Mocchiutti: thanks for having answered all my questions and doubts, and for your daily help, mainly in this last year. My thanks also to the PAMELA group at KTH (Per, William, Juan and Petter) for all the help and the interesting discussions.

I would like to thank all the people working in the Particle and Astroparticle Physics group at KTH for all the nice time and funny lunches we shared together. I will definitely miss lunch at “Phi Phi”, Friday fika and the very funny game “WKL”. A particular thanks goes to my office colleagues, Mózsi and Oscar, for sharing the daily work in a really nice atmosphere.

These five years spent in Stockholm would have not been the same without all the friends I have met here. First of all, thanks to all the people that lived with me in the corridor in Lappis (Amanuensvägen 5, first floor): it was really a pleasure to live together as a big family, sharing different food and cultures from all around the world, and enjoying deep and stupid discussions.

To Ana Catarina, Bego, Dian, Ellen, Ingeborg, Jelena, Jesper, Johann, Maja, Marc, Martjin, Matteo, Peter, Pia, Pierre, Sinéad, Usman: thank you so much for your great friendship!

To Cecilia: thanks for all your help, mainly at the beginning of my life here!

To Ines: thanks for the awesome time we spent in Linz.

To Ana Amelia: it was a great pleasure being invited to your wedding and thanks a lot for your hospitality in Curitiba.

A special thanks goes to Lukas: thank you so much for your daily support as a brother and for the funny time spent together, it was really nice having met someone more crazy than me!

Agli amici di Torino: anche se da lontano, grazie mille per il vostro continuo sostegno. A Clelia: grazie per la tua amicizia senza spazio e senza tempo. Al mio maestro di aikido Renzo Grande e a tutte le persone con cui ho praticato per più di tredici anni: grazie mille per avermi insegnato qualcosa che è ormai diventato parte di me.

Infine, ringrazio la mia famiglia per tutto l'aiuto e il sostegno datomi in questi anni di vita a Stoccolma e non solo. A mamma e papà: grazie per il piacevole tempo trascorso insieme e per avermi sempre dato la forza di andare avanti, soprattutto nei periodi più difficili. Un ringraziamento speciale ad Antonio: grazie per aver affrontato questa avventura insieme a me e, nonostante tutte le difficoltà, grazie per essermi sempre rimasto accanto e per avermi dato quella serenità che cercavo da tempo.



A new adventure is waiting for me...

Nästa: Tübingen!

List of Figures

1.1	The all particle energy spectrum of cosmic rays	6
1.2	Cosmic rays relative abundance	8
1.3	A schematic model of a pulsar	10
1.4	Hillas plot	11
1.5	B/C ratio measurements compared to theoretical propagation models of cosmic rays	14
1.6	The cosmic rays flux and the solar activity	16
1.7	Proton absolute fluxes measured by PAMELA	16
1.8	Representation of the heliosphere current sheet and drift trajectories for 2 GeV protons in an $A > 0$ solar magnetic field configuration	17
1.9	Pre-PAMELA positron fraction compared to a pure secondary positron production model	18
1.10	The PAMELA positron fraction	21
1.11	Electron flux measured by the PAMELA experiment	22
1.12	The electron-plus-positron flux and the positron fraction as measured by different experiments compared to a theoretical computations which consider contributions from galactic cosmic ray electrons and from nearby pulsars	24
1.13	Positron fraction resulting from the sum of all pulsars in our galaxy within 500 pc of the Solar System	25
1.14	Positron fraction considering dark matter particle annihilation models	26
2.1	The Resurs DK1 satellite	28
2.2	The PAMELA instrument	29
2.3	The time-of-flight system	30
2.4	The magnetic spectrometer	32
2.5	The tracker resolution and MDR	33
2.6	The electromagnetic calorimeter	35
2.7	The anticoincidence system	36
2.8	The PAMELA data acquisition system	37
2.9	PAMELA trigger rates	39
3.1	Development of an electromagnetic shower	42
3.2	Photon total cross section	43

3.3	Electromagnetic showers development in different material	46
3.4	Electromagnetic shower induced by a 100 GeV simulated positron	47
3.5	Hadronic shower induced by a 100 GeV simulated proton	49
3.6	Schematic overview of one calorimeter module	52
3.7	Energy resolution of the electromagnetic calorimeter	53
3.8	Distribution of $qtot$ for 100 GeV simulated positrons and protons .	58
3.9	Distribution of $qtotimp$ and $ncore$ for 100 GeV simulated positrons and protons	59
3.10	Distribution of $qpresh$ and $q3$ for 100 GeV simulated positrons and protons	60
3.11	Distribution of $q2$ and $q1$ for 100 GeV simulated positrons and protons	61
3.12	Distribution of $qt1$ and qm for 100 GeV simulated positrons and protons	62
4.1	Configuration of the PAMELA apparatus as simulated by the GPAMELA code	66
4.2	Hadronic shower development in the calorimeter in the <i>only-π^0</i> case simulations	69
4.3	Distribution of the shower longitudinal development in the calorime- ter for simulated positrons and protons (<i>normal case</i>) in the energy range 20 – 100 GeV	72
4.4	Calorimeter energy fraction in the rigidity range 28 – 42 GV . . .	75
4.5	Calorimeter energy fraction in the rigidity range 42 – 65 GV . . .	76
4.6	Calorimeter energy fraction in the rigidity range 65 – 100 GV . .	77
4.7	Calorimeter energy fraction for negative charged particles in flight data	78
4.8	Positron fraction as function of the energy	80
4.9	Distribution of $qcyl/ncyl$ as a function of rigidity for simulated positrons and protons (<i>normal case</i>) in the energy range 20 – 100 GeV . . .	82
4.10	Energy fraction distribution as a function of rigidity for simulated positrons in the energy range 20 – 100 GeV	83
4.11	Distribution of mean and standard deviation values of the energy fraction as a function of rigidity	84
4.12	Distribution of the χ^2 variable as a function of rigidity for simulated positrons in the energy range 20 – 100 GeV	86
4.13	Distribution of the χ^2 variable for simulated positrons and protons (<i>normal</i> and <i>only-π^0</i> case) in the energy range 20 – 100 GeV, with the corresponding selection efficiencies	87
4.14	Distribution of $qcore/ncore$ as a function of rigidity for simulated positrons and protons (<i>normal case</i>) in the energy range 100 – 300 GeV	91
4.15	Distribution of $qpre/npre$, $qpresh$, $q0$ and $e0imp$ as a function of rigidity for simulated positrons and protons (<i>normal case</i>) in the energy range 100 – 300 GeV	92

4.16	Distribution of v_{3sihit} , $asymmetry$, $enfitatmaxns$ and $aveder$ as a function of rigidity for simulated positrons and protons (<i>normal case</i>) in the energy range 100 – 300 GeV	93
4.17	Distribution of the χ^2 variable for simulated positrons and protons (<i>normal</i> and <i>only-π^0</i> case) in the energy range 100 – 300 GeV	94
4.18	Selection efficiency as function of cut values on χ^2 for simulated positrons and protons (<i>normal</i> and <i>only-π^0</i> case) in the energy range 100 – 300 GeV	95
4.19	Distribution of $qtotimp$, v_{4siq} and q_4 as a function of rigidity for simulated positrons and protons (<i>normal</i> and <i>only-π^0</i> case) in the energy range 100 – 300 GeV	96
4.20	Selection efficiency as function of cut values on χ^3 for simulated positrons and protons (<i>normal</i> and <i>only-π^0</i> case) in the energy range 100 – 300 GeV	97
4.21	Selection efficiency as function of cut values on χ^3 for simulated positrons in the energy range 100 – 300 GeV and for flight data	98
4.22	Different values of the positron fraction after the selection $\chi^2 < 8$ and varying the cut on χ^3	101
4.23	Distribution of χ^3 for simulated positrons in the energy range 100 – 300 GeV and for flight data	104
4.24	Positron fraction	105
5.1	Sketch of the MLP neural network architecture	112
5.2	Results of the MLP neural network on simulated samples in the energy range 100 – 300 GeV	113
5.3	MLP distribution for simulations and flight data with fit in the range $(-1, 1)$	115
5.4	MLP distribution for simulations and flight data with fit in the range $(0, 1)$	116
5.5	MLP distribution for positively charged flight data	117
5.6	Results of the bootstrap analysis for negatively and positively charged events	119
5.7	Results of the bootstrap analysis for negatively and positively charged events	120
5.8	Positron fraction	122
6.1	Live time as a function of rigidity	124
6.2	Schematic view of the geometrical factor calculation	126
6.3	Sketch of the PAMELA apparatus with a representation of positive charged particle trajectories inside the magnetic cavity	127
6.4	Distribution of the efficiencies for the selections above the calorimeter	130
6.5	Positron flux evaluated in this analysis compared to other measurements	132
6.6	Positron flux evaluated in this analysis compared to theoretical predictions	133

List of Tables

2.1	PAMELA performances of cosmic ray particles and antiparticles detection	40
4.1	Number of simulated positrons and protons (<i>normal</i> and <i>only-π^0 case</i>) produced and used in this analysis	68
4.2	Number of events selected by the cuts listed in section 4.4 and $q_{track}/q_{tot} \geq 0.5$ for simulated protons in the <i>only-π^0 case</i> and for positively charged events in flight data	78
4.3	Positron fraction values	79
4.4	Proton selection efficiency and proton contamination for simulations in the energy range 20 – 100 GeV	88
4.5	Proton selection efficiency and proton contamination in the energy range 100 – 300 GeV considering simulated protons in the <i>normal case</i>	98
4.6	Proton selection efficiency and proton contamination in the energy range 100 – 300 GeV considering simulated protons in the <i>only-π^0 case</i>	99
4.7	Number of positron and electron events selected in three different rigidity intervals within 20 – 100 GV through the selections listed in section 4.7 with $\chi^2 < 5$	103
4.8	Number of positron and electron events selected in the rigidity interval 100 – 300 GV by the criteria listed in section 4.8	103
5.1	Positron fraction values	121
6.1	Calorimeter selection efficiencies	130
6.2	Positron flux values	132

Bibliography

- [1] M.S. Longair. *High energy astrophysics: particles, photons and their detection*. Cambridge University Press, vol.1, 1994.
- [2] S.P. Swordy. *The energy spectra and anisotropies of cosmic rays*. Space Science Review, **99**: 85 – 94, 2001.
- [3] J. Blümer for the Pierre Auger Collaboration. *Cosmic rays at the highest energies and the Pierre Auger Observatory*. Journal of Physics G, **29**: 867 – 879, 2003.
- [4] F. Salamida for the Pierre Auger Collaboration. *Update on the measurement of the CR energy spectrum above 10^{18} eV made using the Pierre Auger Observatory*. Proceedings of the 32nd International Cosmic Rays Conference, Beijing 2011.
- [5] M. Aglietta et al. *The cosmic ray primary composition in the "knee" region through the EAS electromagnetic and muon measurements at EAS-TOP*. Astroparticle Physics, **21**: 583 – 596, 2004.
- [6] W.D. Apel et al. *Energy spectra of elemental groups of cosmic rays: Update on the KASCADE unfolding analysis*. Astroparticle Physics, **31**: 86 – 91, 2009.
- [7] T. Antoni et al. *KASCADE measurements of energy spectra for elemental groups of cosmic rays: Results and open problems*. Astroparticle Physics, **24**: 1 – 25, 2005.
- [8] W.D. Apel et al. *Kneelike Structure in the Spectrum of the Heavy Component of Cosmic Rays Observed with KASCADE-Grande*. Physical Review Letters, **107**: 171104–1 – 5, 2011.
- [9] K. Greisen. *End to the cosmic-ray spectrum?* Physical Review Letters, **16**: 748 – 750, 1966.
- [10] G.T. Zatsepin and V.A. Kuz'min. *Upper limit of the spectrum of cosmic rays*. JETP Letters, **4**: 78 – 80, 1966.

- [11] J. Abraham et al. *Observation of the Suppression of the Flux of Cosmic Rays above 4×10^{19} eV*. Physical Review Letters, **101**: 061101–1 – 7, 2008.
- [12] <http://www.srl.caltech.edu/ACE/ACENews/ACENews83.html>.
- [13] http://www.srl.caltech.edu/ACE/ace_mission.html.
- [14] M.S. Longair. *High energy astrophysics: stars, the Galaxy and the interstellar medium*. Cambridge University Press, vol.2, 1994.
- [15] <http://jemeuso.riken.jp/en/about2.html>.
- [16] R. Abbasi et al. *An absence of neutrinos associated with cosmic-ray acceleration in γ -ray burts*. Nature, **484**: 351 – 354, 2012.
- [17] A.W. Strong, I.V. Moskalenko, and V.S. Ptuskin. *Cosmic-Ray Propagation and Interaction in the Galaxy*. Annual Review of Nuclear and Particle Science, **57**: 285 – 327, 2007.
- [18] A.W. Strong and I.V. Moskalenko. *Propagation of cosmic-ray nucleons in the galaxy*. The Astrophysical Journal, **509**: 212 – 228, 1998.
- [19] S.A. Stephens and R.E. Streitmatter. *Cosmic-Ray Propagation in the Galaxy: Techniques and the Mean Matter Traversal*. The Astrophysical Journal, **505**: 266 – 277, 1998.
- [20] J. Wu. *Measurements of cosmic ray antiprotons with PAMELA and studies of propagation models*. Ph.D. Thesis, Physics Department, Royal Institute of Technology, Stockholm, Sweden, 2012.
- [21] O. Adriani et al. *New Measurement of the Antiproton-to-Proton Flux Ratio up to 100 GeV in the Cosmic Radiation*. Physical Review Letters, **102**: 051101–1 – 5, 2009.
- [22] P.K.F. Grieder. *Cosmic Rays at Earth*. Elsevier, 2001.
- [23] <http://www.nmdb.eu/?q=node/138>.
- [24] P. Goldhagen et al. *Measurement of the energy spectrum of cosmic-ray induced neutrons aboard an ER-2 high-altitude airplane*. Nuclear Instruments and Methods in Physics Research, **A 476**: 42 – 51, 2002.
- [25] Particle Data Group. *Review of Particle Physics*. Physics Letters, **B 667**: 1, 2008.
- [26] <http://neutronm.bartol.udel.edu/>.
- [27] P. Picozza et al. *Understanding cosmic rays and searching for exotic sources with PAMELA*. Astrophysics and Space Sciences Transactions, **7**: 85 – 91, 2011.

- [28] J.W. Bieber et al. *Antiprotons at Solar Maximum*. Physical Review Letters, **83**: 674 – 677, 1999.
- [29] M.S. Potgieter and R.A. Burger. *The modulation of cosmic-ray electrons, positrons and helium nuclei as predicted by a drift model with a simulated wavy neutral sheet*. Astronomy and Astrophysics, **233**: 598 – 604, 1990.
- [30] J.R. Jokipii and B. Thomas. *Effects of drift on the transport of cosmic rays*. The Astrophysical Journal, **243**: 1115 – 1122, 1981.
- [31] O. Adriani et al. *Observation of an anomalous positron abundance in the cosmic radiation*. Nature, **458**: 607 – 609, 2009.
- [32] I.V. Moskalenko and A.W. Strong. *Production and propagation of cosmic-ray positrons and electrons*. The Astrophysical Journal, **493**: 694 – 707, 1998.
- [33] S.W. Barwick et al. *Measurements of the cosmic-ray positron fraction from 1 to 50 GeV*. The Astrophysical Journal, **482**: L191 – L194, 1997.
- [34] R.J. Protheroe. *On the nature of the cosmic ray positron spectrum*. The Astrophysical Journal, **254**: 391 – 397, 1982.
- [35] L. Zhang and K.S. Cheng. *Cosmic-ray positrons from mature gamma-ray pulsars*. Astronomy and Astrophysics, **368**: 1063 – 1070, 2001.
- [36] M. Boezio et al. *PAMELA and indirect dark matter searches*. New Journal of Physics, **11**: 105023–1 – 25, 2009.
- [37] D. Hooper, P. Blasi, and P.D. Serpico. *Pulsars as the sources of high energy cosmic ray positrons*. Journal of Cosmology and Astroparticle Physics, **0901**: 025, 2009.
- [38] O. Adriani et al. *Cosmic-Ray Electron Flux Measured by the PAMELA Experiment between 1 and 625 GeV*. Physical Review Letters, **106**: 201101–1 – 5, 2011.
- [39] Y. Asaoka et al. *Measurements of Cosmic-ray Low Energy Antiproton and Proton Spectra in a Transient Period of Solar Field Reversal*. Physical Review Letters, **88**: 051101–1 – 4, 2002.
- [40] J. Clem and P. Evenson. *Cosmic Ray Positron Fraction Observations During the A- Magnetic Solar Minimum*. Proceedings of the 30th International Cosmic Rays Conference, Merida 2007.
- [41] T. Delahaye et al. *Galactic secondary positron flux at the Earth*. Astronomy and Astrophysics, **501**: 821 – 833, 2009.
- [42] M. Boezio et al. *The cosmic-ray electron and positron spectra measured at 1 AU during solar minimum activity*. The Astrophysical Journal, **532**: 653 – 669, 2000.

- [43] M.A. Du Vernois et al. *Cosmic-ray electrons and positrons from 1 to 100 GeV: measurements with HEAT and their interpretations*. The Astrophysical Journal, **559**: 296 – 303, 2001.
- [44] J. Alcaraz et al. *Leptons in near Earth orbit*. Physics Letters, **B 484**: 10 – 22, 2000.
- [45] C. Grimani et al. *Measurements of the absolute energy spectra of cosmic-ray positrons and electrons above 7 GeV*. Astronomy and Astrophysics, **392**: 287 – 294, 2002.
- [46] T. Kobayashi et al. . Proceedings of the 26th International Cosmic Rays Conference, Salt Lake City 1999.
- [47] S. Torii et al. *The Energy Spectrum of Cosmic-Ray Electrons from 10 to 100 GeV Observed with a Highly Granulated Imaging Calorimeter*. The Astrophysical Journal, **559**: 973 – 984, 2001.
- [48] J. Chang et al. *An excess of cosmic ray electrons at energies of 300–800 GeV*. Nature, **456**: 362 – 365, 2008.
- [49] F. Aharonian et al. *Energy Spectrum of Cosmic-Ray Electrons at TeV Energies*. Physical Review Letters, **101**: 261104 1 – 5, 2008.
- [50] M. Ackermann et al. *Fermi LAT observations of cosmic-ray electrons from 7 GeV to 1 TeV*. Physical Review, **D 82**: 092004–1 – 20, 2010.
- [51] D. Grasso et al. *Possible interpretations of the high energy cosmic ray electron spectrum measured with the Fermi space telescope*. Nuclear Instruments and Methods in Physics Research, **A 630**: 48 – 51, 2011.
- [52] D. Grasso et al. *On possible interpretations of the high energy electronpositron spectrum measured by the Fermi Large Area Telescope*. Astroparticle Physics, **32**: 140 – 151, 2009.
- [53] M. Kamionkowski and M.S. Turner. *Distinctive positron feature from particle dark-matter annihilations in the galactic halo*. Physics Review, **D 43**: 1774 – 1780, 1991.
- [54] M. Cirelli et al. *Model-independent implications of the e^\pm , antiproton cosmic ray spectra on properties of Dark Matter*. Nuclear Physics, **B 813**: 1 – 21, 2009.
- [55] L. Bergström, T. Bringmann, and J. Edsjö. *New Positron Spectral Features from Supersymmetric Dark Matter - a Way to Explain the PAMELA Data?* Physical Review, **D 78**: 103520–1 – 6, 2008.
- [56] H.C. Cheng, J.L. Feng, and K.T. Matchev. *Kaluza-Klein Dark Matter*. Physical Review Letters, **89**: 211301–1 – 4, 2002.

- [57] <http://www.ams02.org/>.
- [58] P. Von Doetinchem et al. *PEBS - Positron Electron Balloon Spectrometer*. Nuclear Instruments Methods, **A 581**: 151 – 155, 2007.
- [59] P. Picozza et al. *PAMELA - A payload for antimatter matter exploration and light-nuclei astrophysics*. Astroparticle Physics, **27**: 296 – 315, 2007.
- [60] G. Osteria et al. *The time-of-flight system of the PAMELA experiment on satellite*. Nuclear Instruments and Methods, **A 535**: 152 – 157, 2004.
- [61] O. Adriani et al. *The magnetic spectrometer of the PAMELA satellite experiment*. Nuclear Instruments and Methods, **A 511**: 72 – 75, 2003.
- [62] <http://pamela.roma2.infn.it>.
- [63] O. Adriani et al. *The magnetic spectrometer of the PAMELA experiment: on-ground test of the flight-model*. 29th International Cosmic Ray Conference, Pune, **00**: 101 – 104, 2005.
- [64] M. Boezio et al. *High granularity imaging calorimeter for cosmic rays physics*. Nuclear Instruments and Methods, **A 487**: 407 – 422, 2002.
- [65] O. Adriani et al. *PAMELA results on the cosmic-ray antiproton flux from 60 MeV to 180 GeV in kinetic energy*. Physical Review Letters, **332** (6025): 121101–1 – 11, 2010.
- [66] O. Adriani et al. *A statistical procedure for the identification of positrons in the PAMELA experiment*. Astroparticle Physics, **34**: 1 – 11, 2010.
- [67] O. Adriani et al. *PAMELA Measurements of Cosmic-Ray Proton and Helium Spectra*. Science, **332** (6025): 69 – 72, 2011.
- [68] R. Wigmans. *Calorimetry, Energy Measurement in Particle Physics*. Oxford science publications, 2000.
- [69] B. Rossi. *High-Energy Particles*. Englewood Cliffs, N.J.: Prentice Hall, 1952.
- [70] T. Åkesson et al. *Inclusive η production at low transverse momentum in 63 GeV pp Collision at the Cern intersecting storage rings*. Physics Letters B, **178**: 447 – 451, 1986.
- [71] J. Lund. *Antiparticle identification studies for the PAMELA satellite experiment*. Ph.D. Thesis, Physics Department, Royal Institute of Technology, Stockholm, Sweden, 2004.
- [72] F. Cafagna. *GPAMELA – Program for PAMELA Simulation with GEANT*. http://pcba28.ba.infn.it/pamela-cgi/cvsweb_pamela.cgi/gpamela/.
- [73] R. Brun et al. *Detector Description and Simulation Tool*. CERN Program Library Long Writeup W5013, 1994.

- [74] A. Bruno. *Cosmic ray antiprotons measured in the PAMELA experiment*. Ph.D. Thesis, Physics Department of University of Bari, Italy, 2008.
- [75] C. Leroy and P.G. Rancoita. *Physics of cascading shower generation and propagation in matter: principles of high-energy, ultrahigh energy and compensating calorimetry*. Reports on Progress in Physics, **63**: 505 – 606, 2000.
- [76] B. Efron and R. Tibshirani. *An introduction to the Bootstrap*. Chapman and Hall, 1993.
- [77] M. Schubnell. *The cosmic-ray positron and electron excess: an experimentalist's point of view*. arXiv:0905.0444, 2009.
- [78] A. Hoecker et al. *TMVA 4, Toolkit for Multivariate Data Analysis with ROOT*. CERN-OPEN-2007-007, 2009.
- [79] *root.cern.ch*.
- [80] J.D. Sullivan. *Geometrical factor and directional response of single and multi-element particle telescopes*. Nuclear Instruments and Methods, **95**: 5 – 11, 1971.
- [81] E. Mocchiutti. Private communication, 2012.
- [82] E. Mocchiutti on behalf of the PAMELA Collaboration. *Electron and Positron Spectra Measured by the PAMELA Space Experiment*. Proceedings of the 32nd International Cosmic Rays Conference, Beijing 2011.
- [83] M. Ackermann et al. *Measurement of separate cosmic-ray electron and positron spectra with the Fermi Large Area Telescope*. Physical Review Letters, **108**: 011103–1 – 7, 2012.
- [84] M. Boezio et al. *Measurement of cosmic-ray electrons and positrons by the Wizard/CAPRICE Collaboration*. Advances in Space Research, **27**: 669 – 674, 2001.
- [85] S.W. Barwick et al. *Measurements of the Cosmic-Ray Positron Fraction from 1 to 50 GeV*. The Astrophysical Journal, **482**: L191 – L194, 1997.
- [86] J. Alcaraz et al. *Leptons in near earth orbit*. Physical Letters, **B 484**: 10 – 22, 2000.
- [87] T. Delahaye et al. *Galactic secondary positron flux at the Earth*. Astronomy and Astrophysics, **501**: 821 – 833, 2009.